February 2021

Investigating the Recent History of a Changing Planet with Innovative Isotopic Techniques and New Geologic Archives

Ryan A. Venturelli
University of South Florida

Investigating the Recent History of a Changing Planet with Innovative Isotopic Techniques and New Geologic Archives

by

Ryan A. Venturelli

A dissertation submitted in partial fulfillment
of the requirements for the degree of
Doctor of Philosophy
College of Marine Science
University of South Florida

Major Professor: Brad E. Rosenheim, Ph.D.
Robert H. Byrne, Ph.D.
Sierra V. Petersen, Ph.D.
Amelia E. Shevenell, Ph.D.
Lauren T. Toth, Ph.D.

Date of Approval:
February 2, 2021

Keywords: Isotope Geochemistry, Radiocarbon, Paleoglaciology, Mass Spectrometry

Epigraph

The mystic Barrier! All accounts without exception, from the days of Ross to the present time, had spoken of this remarkable natural formation with apprehensive awe. It was as though one could always read between the lines the same sentence: "Hush, be quiet! the mystic Barrier!" One, two, three, and a little jump, and the Barrier was surmounted! We looked at each other and smiled; probably the same thought was in the minds of all of us. The monster had begun to lose something of its mystery, the terror something of its force; the incomprehensible was becoming quite easy to understand.

—*Roald Amundsen*, The South Pole

Acknowledgments

Though I am the person who will earn a degree for this work, this dissertation reflects the collective influence and input of the many teachers, mentors, collaborators, co-authors, labmates, and friends who have helped me along this wild and winding academic path.

This dissertation would not exist if not for the support of my advisor, Dr. Brad Rosenheim. Thank you, Brad, for giving me full reign of your analytical playground, for always changing while to whereas, and for providing me a solid foundation on which to build my career. Most importantly, thank you for encouraging me to keep climbing the mountain on the days when it felt too high. My work has benefitted from the input of my dissertation committee: Dr. Amelia Shevenell, Dr. Sierra Petersen, Dr. Lauren Toth, and Dr. Robert Byrne who have acted as a sounding board and helped guide the work herein. I extend many extra thanks to Sierra for allowing me spend time in her lab when I was ready to throw in the towel and wash my hands of mass spectrometry altogether.

Many parallels exist between the process of completing a Ph.D. and the process of carrying out field work in Antarctica. If I am certain of anything after both experiences, it is that the people who work to make both of these things possible are superheroes who deserve much more than a line in the acknowledgements of the many theses and dissertations they have made possible. Within the College of Marine Science, I owe special thanks to Dr. David Naar and Samyntha Francis for all they do to make graduate student life as easy as possible in our program. I extend my most sincere gratitude to Ethan Goddard who handled my obnoxiously low carbon samples with ease and always managed to find time to answer my many questions. Data in chapters 3–5 were acquired with funding from the National Science Foundation (NSF grant OPP-1543347) and the National Ocean Science Accelerator Mass

Spectrometer (NOSAMS) Laboratory graduate student internship. I extend many thanks to my collaborators on the Subglacial Antarctic Lakes Scientific Access (SALSA) Project as well as those who made this project a success: Antarctic Support Contract, the New York Air National Guard, Ken Borek Air, the University of Nebraska drill team, Cat Hickman, Ellie Mango, and Julie Mueller.

The College of Marine Science has provided me with a community of people who have made the last few years among the best of my life. I owe many thanks to members of the 2015 cohort with whom this whole journey started too many years ago. Throughout my time at CMS, Rosenheim and Shevenell group members have become a tight knit family who were always as willing to tear apart one of my manuscript drafts as they were to get into good trouble. I owe special thanks to Katy Smith, Michelle Guitard, Carey Schafer, Kara Vadman, Imogen Browne, Theresa King, Catherine Prunella, Cristina Subt, and Devon Firesinger who have always listened, inspired, and helped. I have been lucky to share a home with my best friends throughout this work; thank you to Imogen, Kara, Carey, and (honorary housemate) Jon for filling our yellow nest with science, love, lots of laughs, and an abundance of chicken nuggets.

Outside of CMS, I have learned from a number of people who have each shared with me the magic that makes them incredible scientists and humans. I would like to give a special shout out to Amy Leventer, Helen Fricker, Molly Patterson, Jeanine Ash, Tristy Vick-Majors, Erin Argyilan, Jennifer Latimer, Christina Davis, Mark Kurz, Al Gagnon, Chris Maupin, Ben Keisling, Peter Neff, Wei Li, David Harwood, Brent Christner, and John Priscu who have all spent a significant amount of their time providing advice, edits, and mentorship that have benefitted me personally and professionally. Finally, I must acknowledge Chloe Gustafson, Alex Michaud, and Matt Siegfried–also known as the SALSA tots. I owe most everything I know about the Antarctic subglacial environment to our endless group message and ongoing journal club. Science is truly a better place with you three in it, and I look forward to all of the collaboration and black box dance parties in our future.

Table of Contents

List of Figures

List of Tables

Abstract

Globally averaged Earth surface temperatures indicate a 0.8°C warming since 1880. Though this warming is a result of anthropogenic influence that has exceeded natural forcings, a thorough understanding of Earth's climate system requires a knowledge of changes in global temperatures beyond the instrumental record. To achieve this, we must supplement the temporally limited observational record with proxy records of environmental conditions in the geologic past. Though the foundational questions underlying interrogations of the geologic past are seemingly simple (What happened? When?), the accuracy of their answers depend upon accessibility and availability of geologic materials as well as the capabilities of proxies applied to those materials. Because uncertainties in proxy reconstructions can propagate into projections of future conditions, it is important that we continuously work to expand the utility of geologic archives and the capabilities of proxies and preparatory techniques we apply to them. I utilize the seldomly accessed sub-ice sediment record to address questions surrounding the deglacial history of the Ross Sea Embayment, Antarctica. I optimize ramped pyrolysis preparation of acid insoluble organic material in these sediments to assess the timing of past grounding line retreat, and use isotopic data to assess the origin, age, and cycling of carbon beneath the West Antarctic Ice Sheet. I demonstrate the utility of sub-ice archives for deglacial paleoglaciological reconstructions by investigating how Holocene-aged carbon is translocated to subglacial sediments. In the interest of addressing questions about past climate, I also present improvements to the mass spectrometry of multiply substituted isotopologues of CO_2, a promising new isotopic paleothermometer.

1 Introduction

1.1 Paleoclimate Research

Earth's climate is a product of interactions between five components–the biosphere, hydrosphere, atmosphere, cryosphere, and lithosphere. Though changes in some of these components (e.g., atmosphere, biosphere) can be observed over weeks to months, others (e.g., lithosphere) experience changes over thousands to millions of years. In order to understand the cumulative effect that interactions between these components play in the evolution of Earth's climate, records longer than the time it takes each to change is necessary. The global instrumental record covers only the last ∼150 years of Earth's >4.5 billion year history (Brohan et al., 2006), and thus does not provide an adequate record for assessing Earth's climate system. Therefore, the instrumental record must be supplemented by the geologic record to gain a comprehensive understanding of modern and future climate (Steig & Neff, 2018; Tierney et al., 2020).

Paleoclimate research provides records of variability in Earth's climate system as well as its relationship to forcing mechanisms and feedbacks (e.g., Westerhold et al., 2020). To extend records of Earth's climate into the geologic past, we tap into natural archives (e.g., sediment cores, ice cores, speleothems, fossils) to extract physical, chemical, and biological information that provide indirect links to past environmental conditions. These proxy records enable us to answer the two fundamental questions that underlie paleoclimate research—"What happened?" and "When?".

Each geologic archive may differ in the extent to which it enables us to decipher what happened or when across space and time. For example, reconstructions employing ice

cores or coral skeletons may provide seasonal to annual records, but the temporal resolution of sediment-based reconstructions may vary based on sedimentation rate or accommodation space. By combining multiple, accurately dated proxy records extracted from these archives, we can achieve a record of climate variability throughout Earth's history.

1.2 Isotopes in Paleoclimate Research

The measurement of isotopes provides one means of interpreting and quantifying changes that occurred prior to the instrumental record. Whereas the abundance or depletion of stable isotopes can be used to infer changes in environmental conditions and past temperatures, the decay of radiogenic isotopes can be used to tie such changes to geologic time. The development and application of isotopic tools enables us to generate paleoclimate records from previously untapped archives, which will ultimately help to improve our understanding of Earth's climate. My dissertation is motivated by an interest in pushing the technical capabilities of innovative isotopic techniques forward for new and different applications in paleoclimate research. This work began with an interest in employing stable isotopic tools to reconstruct paleotemperature.

1.2.1 Stable Isotopic Tools

The theory underlying oxygen isotope paleothermometry is attributed to Harold Urey's work investigating isotopic fractionation of light elements between ideal gases and aqueous ions. This work included the determination of a temperature coefficient of oxygen isotope fractionation between calcium carbonate ($CaCO_3$) and water (H_2O) in a heterogeneous isotope exchange reaction (Urey, 1947):

$$H_2{}^{18}O^{+}CaC^{16}O_3 \rightleftharpoons H_2{}^{16}O^{+}CaC^{18}O^{16}O_2 \tag{1.1}$$

Equilibrium predictions of isotope partitioning between $CaCO_3$ and H_2O have enabled the reconstruction of temperature of formation for various living (e.g., corals, molluscs,

foraminifera) and non-living (e.g., speleothems) geologic archives. The extent to which each of these archives is useful for reconstructing paleotemperature varies, however, each requires knowledge of the $^{18}O/^{16}O$ ratio of the water from which the $CaCO_3$ precipitated.

On geologic timescales, the oxygen isotopic composition of seawater ($\delta^{18}O_w$) reflects both the amount of global continental ice and the evaporation-precipitation balance (Schrag et al., 1996; Adkins, 2002). Therefore, the oxygen isotopic composition of marine carbonates is dually dependent on $\delta^{18}O_w$ and the temperature at which the mineral was formed. Paleotemperature measurements derived from marine carbonate $\delta^{18}O$ thus may only be as accurate as our knowledge of $\delta^{18}O_w$ when the mineral formed. With the exception of pore-water profile constraints on $\delta^{18}O_w$ from the Last Glacial Maximum (Adkins, 2002), very few direct measurements of variations in $\delta^{18}O_w$ through time exist. Therefore, an independent proxy for temperature or ice volume is needed to decouple the combined effect of temperature and $\delta^{18}O_w$ on the $\delta^{18}O$ record.

Several organic [e.g., alkenones (Müller et al., 1998) and biomarkers (Schouten et al., 2002)] and inorganic [e.g., measurement of Mg/Ca (Delaney et al., 1985; Anand et al., 2003; Elderfield et al., 2006) and Sr/Ca ratios (Beck et al., 1992)] paleotemperature proxies have been developed and applied in attempts to overcome uncertainties associated with $\delta^{18}O_w$ assumptions in the application of oxygen isotope paleothermometry. The range and diversity of proxies applied to decouple temperature and $\delta^{18}O_w$ provides insight to the magnitude of the problem. The development and application of new proxies has enabled a different approach to solve for past variations in $\delta^{18}O_w$, however, each new proxy application brings uncertainties of its own. Trace metal paleothermometry (e.g., Mg/Ca, Sr/Ca) introduces uncertainty when past seawater compositions are unknown, whereas organic proxies may introduce uncertainty relating to biological source (Wang et al., 2021) and calibration (Kim et al., 2010). Without an accurately constrained $\delta^{18}O_w$, the $\delta^{18}O$ paleothermometer remains limited in its ability to accurately answer, "What happened?".

Carbonate clumped isotope paleothermometry has been developed within the last decade as a promising new approach for solving the unknown $\delta^{18}O_w$ problem (Eiler, 2007, 2011). In contrast to Urey's oxygen isotope paleothermometer, the clumped isotope paleothermometer is based upon a homogenous isotope exchange reaction:

$$M^{12}C^{18}O^{16}O_2{}^{+} M^{13}C^{16}O_3{}^{2-} \rightleftharpoons M^{13}C^{18}O^{16}O_2 + M^{12}C^{16}O_3{}^{2-} \tag{1.2}$$

where M is Ca in calcite minerals typically employed for paleotemperature measurement. Equation 1.2 has a temperature dependent equilibrium constant that theoretically approaches 1 at high temperatures (1000°C) when molecules containing ^{13}C–^{18}O are stochastically distributed (Schauble et al., 2006). In systems below 1000°C, an inverse linear relationship exists between the concentration of ^{13}C–^{18}O bonds and temperature, due to the lower vibrational energy (and higher stability) of molecules containing bonds between two heavy isotopes. Because all components of equation 1.2 are in a single phase, the equilibrium constant is an internal property unobstructed by $\delta^{18}O_w$ (Eiler & Schauble, 2004; Ghosh et al., 2006; Schauble et al., 2006).

Early clumped isotope measurements of natural and synthetic carbonates (Δ_{47}) demonstrated promising agreement with theory (Ghosh et al., 2006), which enabled an increase in Δ_{47} derived paleotemperature reconstructions. As the number of laboratories making Δ_{47} measurements increased, interlaboratory comparability issues became apparent. Advances in standardization (e.g., Dennis et al., 2011; Bernasconi et al., 2018), sample preparation (temperature of acid digestion reaction; e.g., Defliese et al., 2015; Murray et al., 2016), analytical corrections (He et al., 2012; Bernasconi et al., 2013; Venturelli & Rosenheim, 2018), and mathematical corrections (Daëron et al., 2016; Schauer et al., 2016) have allowed the field to overcome interlaboratory differences (Petersen et al., 2019). As such, Δ_{47} measurements have provided reliable reconstructions of paleotemperature and seawater chemistry

(both $\delta^{18}O_w$ and Mg/Ca; Petersen & Schrag, 2015; Petersen et al., 2016; Winkelstern et al., 2017; Rodríguez-Sanz et al., 2017; Evans et al., 2018; Leutert et al., 2020).

1.2.2 Radiocarbon

In investigations of Earth's recent past (e.g., late Pleistocene to Holocene), radiocarbon (^{14}C) dating is a widely applied method used to tie paleoclimate records to the geologic timescale. The theory underlying modern ^{14}C dating is attributed to Willard Libby's work investigating the production of ^{14}C in the upper atmosphere (Libby, 1946).

$$^{14}N + n \longrightarrow {}^{14}C + H \tag{1.3}$$

Newly produced ^{14}C is oxidized to ^{14}CO and $^{14}CO_2$ (e.g., Pandow et al., 1960), which enters the biosphere by oceanic exchange (inorganic carbon) and photosynthesis (organic carbon). Living organisms maintain a ^{14}C content in equilibrium with the atmosphere through photosynthesis or respiration. When an organism dies, ^{14}C is no longer assimilated into its tissues, resulting in a decline in ^{14}C as it decays to ^{14}N.

$$^{14}C \longrightarrow {}^{14}N + \beta + \text{neutrino} \tag{1.4}$$

The activity of ^{14}C in a collected carbon sample can then be used to determine the timing of death and deposition (Libby et al., 1949; Libby, 1955). The relatively short ^{14}C half-life [5568 yr (Libby, 1955); 5730 yr (Godwin, 1962)] enables ^{14}C to be used as a chronometer that reliably covers the last ∼55,000 years (Reimer et al., 2020). However, a strength and a weakness of using carbon to acquire absolute dates is its ubiquity on the Earth's surface and its absolute necessity for life. As such, the form of carbon from which ^{14}C is measured determines the reliability of the acquired date (Libby, 1955). In paleoclimate research, biogenic marine carbonate (e.g. foraminiferal tests, coral skeletons) is the preferred material for ^{14}C dating because of the unambiguous origin and general

abundance in the marine environment. However, where carbonate mineral preservation and production is poor due to corrosive bottom waters (e.g., the Southern Ocean; Kennett, 1968), organic carbon (OC) may be employed for ^{14}C dating. In sediment cores retrieved from the open ocean, OC is dominated by autochthonous carbon, sourced from primary productivity (phytoplankton) in the surface ocean. In sediment cores collected from the continental shelf, however, allochthonous carbon (such as plant debris, continental sedimentary rocks, and ancient kerogen transported from a terrestrial setting to a marine setting) is present in addition to autochthonous material. If OC is primarily composed of allochthonous material, ^{14}C concentrations may reflect processes unrelated to the age of sediment deposition. The separation of allochthonous material from autochthonous material has thus been a driving goal of researchers that employ OC for ^{14}C dating.

Sample size requirements for analysis of ^{14}C concentrations limited early separation of OC. Initially, ^{14}C concentrations were evaluated with counting techniques (i.e. Geiger counting, gas proportional counting, liquid scintillation counting) that required >1 g of carbon. The development of accelerator mass spectrometry (AMS) reduced sample size requirements to <1 mg of carbon (Muller et al., 1977; Beukens et al., 1977; Nelson et al., 1977; Muller et al., 1978). The continued effort to reduce sample sizes for AMS analyses (Pearson et al., 1997; Synal et al., 2007) has enabled the development of compound specific radiocarbon analysis (CSRA; Eglinton et al., 1997; Pearson et al., 2000; Ohkouchi et al., 2003). The expansion and application of CSRA throughout the last 20 years has allowed for the investigation of sources of carbon to TOC in the marine environment, despite the persistence of difficulties in dating increasingly small sample sizes.

Whereas CSRA requires the chemical extraction of specific biomarkers to separate OC mixtures, Ramped Pyrolysis (Ramped PyrOx; RPO) ^{14}C exploits the range of thermochemical stabilities in OC mixtures to separate allochthonous from autochthonous carbon (Rosenheim et al., 2008). By separating OC mixtures with heat, RPO yields a spectrum of isotopic data that demonstrates that the youngest, most labile material is pyrolyzed at a

lower temperatures than older, more diagenetically stable material. Specifically, RPO was developed for ^{14}C dating of carbonate poor, Antarctic marine sediments. To date, RPO has been applied using Antarctic marine sediments from Palmer Deep (Rosenheim et al., 2008), Hugo Bay Trough (Rosenheim, Santoro, et al., 2013), and Lapeyrère Bay (Subt et al., 2016) as well as sub-ice shelf sediments near Larsen C (Subt et al., 2017). This work demonstrated that RPO ^{14}C is a reliable method for developing chronologies when carbonate material is unavailable. Furthermore, when used in combination with carbonate ^{14}C, RPO can be used to understand the sources of OC to the sediment (Subt et al., 2016). The ability to use low-temperature RPO aliquots for chronologic constraints depends on how well autochthonous carbon has been isolated from allochthonous carbon and, similar to CSRA is limited by sample size. Two adaptations of RPO (Isotope dilution and composite techniques), developed by Subt et al. (2017) circumvent sample size limitations, yielding ages comparable to those from foraminiferal calcite. The recent methodological adjustments to RPO lend promise to the potential of this method to isolate autochthonous carbon in OC deposits extracted from presently ice covered environments of Antarctica.

1.3 Antarctica and Sea Level Rise

Of the many consequences of modern and future climate change, sea level rise poses the most impactful disruption to society (e.g., Hauer et al., 2016). As global temperatures increase, both the thermal expansion of seawater and mass loss from continental-scale ice sheets result in a rise in global mean sea level (Church et al., 2013; Dutton et al., 2015). Antarctica hosts one of two remaining continental-scale ice sheets on modern Earth. The Antarctic Ice Sheet, typically discussed in two parts—the West Antarctic Ice Sheet (WAIS) and the East Antarctic Ice Sheet (EAIS), contains 57.2 meters of sea level equivalent ice (Rignot et al., 2019). Satellite observations using NASA's Ice, Cloud, and land Elevation Satellites (ICESat & ICESat-2) indicate that Antarctica has been experiencing a mass loss of 118 billion tonnes per year since 2003 (Smith et al., 2020).

Though future projections indicate that ice mass loss from Antarctica will account for the greatest contribution to rising sea level in the coming decade (Joughin et al., 2014; DeConto & Pollard, 2016), how much, how fast, and from where Antarctica will lose mass accounts for the largest source of uncertainty in future projections (e.g., Bamber et al., 2019). This uncertainty is, in part, a result of the temporally limited record of ice dynamics. However, our understanding of long-term ice sheet change can be improved by interfacing the short, observational record with the longer-term record of ice sheet change preserved in the geologic record. The most recent analogue of large-scale ice sheet change can be observed in the geologic record as deglaciation following the Last Glacial Maximum within the Ross Embayment.

1.4 Region of Study

The Ross Embayment is made up of the modern Ross Ice Shelf and Ross Sea. Here, 25% of Antarctic Ice flows into the Ross Ice Shelf, making it the single largest drainage basin in Antarctica (Halberstadt et al., 2016). This region has been shaped by the West Antarctic Rift System; the extension of which formed both the Ross Sea and deep basins therein, some of which extend beneath the contemporary WAIS (e.g., Jankowski & Drewry, 1981; Cooper et al., 1991; Bell et al., n.d.). Along the East Antarctic boundary of the West Antarctic Rift System lie the Transantarctic Mountains, long thought to separate the thick East Antarctic lithosphere from the thin, subsided lithosphere of West Antarctica (e.g., Behrendt et al., 1991; Behrendt, 1999; Goodge, 2020). More recently, magnetic and gravity data from airborne surveys over Ross Ice Shelf have been used to reposition this tectonic boundary between East and West Antarctica to below the Ross Ice Shelf (Tinto et al., 2019).

The work herein focuses on sediments collected from two sites along the Siple Coast of West Antarctica, Mercer Subglacial Lake (SLM) and Whillans Grounding Zone (WGZ), which are influenced by both the stability of the overlying Mercer and Whillans ice streams, and the geology over which these ice streams flow (Figure 1.1). Mercer Ice Stream is fed

by Reedy Glacier, an outlet of EAIS that flows through the Transantarctic Mountains. Upstream sources of sediments and solutes may come from Precambrian to Ordovician igneous and metamorphic rocks overlain by late Paleozoic sedimentary deposits that exist beneath Reedy Glacier (Mercer, 1968). As ice from Reedy Glacier flows into Mercer Ice Stream, its fast flow is enabled by a layer of water saturated till (Alley et al., 1986; Blankenship et al., 1986) of glaciomarine origin (Scherer, 1991; Tulaczyk et al., 1998). Transport of components of these sediments by ice (Alley et al., 1998) and water (Carter & Fricker, 2012) provides an additional West Antarctic source of sediment and solutes to SLM and WGZ. During periods in the geologic past when ice did not exist over SLM and WGZ, the low lying lithosphere in this region enabled the formation of a seaway and thus, open marine productivity over the region (e.g., Scherer, 1991).

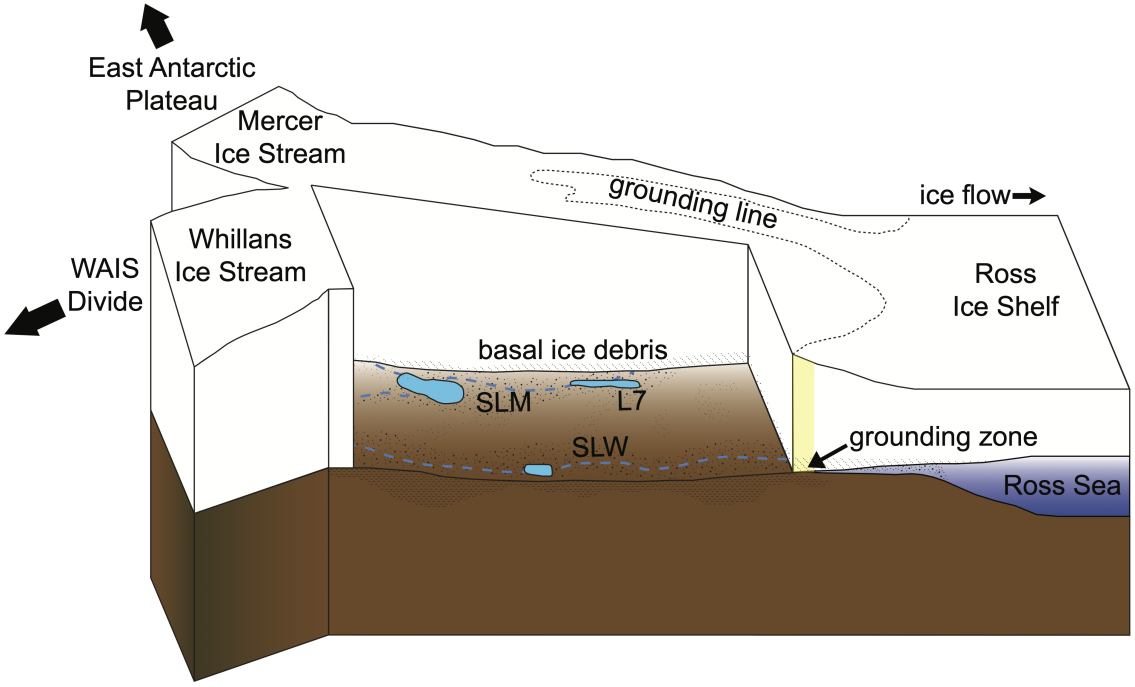

Figure 1.1: Cutaway diagram of Whillans and Mercer ice streams. Sediment samples in this dissertation were retrieved from Whillans Grounding Zone and Mercer Subglacial Lake.

It is well-established that during the Last Glacial Maximum, grounded ice filled the Ross Embayment to the continental shelf edge (e.g., Anderson et al., 2002, 2014; Halberstadt et al., 2016). However, several decades of paleoglaciological investigation about how the region has changed following the Last Glacial Maximum have resulted in active debate surrounding both the timing and nature of deglaciation. The most widely cited explanation for deglacial grounding line retreat in this region is the "swinging gate" model, wherein the grounding line was hinged at Roosevelt Island in the eastern Ross Sea, while the western Ross Sea deglaciated rapidly along the Transantarctic Mountains (Conway et al., 1999). As further marine evidence was collected on the continental shelf, the asynchronicity of deglaciation across the Ross Sea Embayment (Ackert, 2008) and the importance of seafloor morphology and physiological characteristics (Halberstadt et al., 2016) resulted in two further deglacial models ("saloon door" and "marine based"). Though these models differ in the timing and mechanism of retreat, each is bound to geologic evidence from presently ice-free archives (e.g., continental shelf geomorphology, exposure ages, raised beach deposits). This perspective has resulted in the paradigm that deglacial grounding line retreat in the Ross Embayment occured in a unidirectional fashion from the continental shelf edge to the modern position. Conversely, in a recent study by Kingslake et al. (2018), an ice sheet model and bulk ^{14}C dating of subglacial sediments demonstrated that the grounding line could have retreated far inland from its modern position during the deglaciation and subsequently re-advanced during the Holocene. Therefore, further investigation of sediments collected from beneath presently ice-covered regions of West Antarctica (SLM and WGZ) may be able to fill a gap in our knowledge of deglacial ice dynamics in this region.

1.5 Focus of the Dissertation

My dissertation is motivated by an interest in pushing the technical capabilities of clumped isotope mass spectrometry and Ramped PyrOx ^{14}C forward for new and different applications

in paleoclimate research. The questions to be answered in my work can be divided into two main foci:

1. **Optimization of sub-ice geologic archives for interrogating Holocene ice sheet history**

    - Can Ramped PyrOx ^{14}C be used to decipher chronologically relevant information from sub-ice geologic archives?
    - What are the sources of organic carbon to the Antarctic sub-ice environment and how do they differ in temporal scale?
    - How can natural level ^{14}C in the subglacial environment be used to define the carbon cycle in an Antarctic subglacial lake?

2. **Clumped isotope method development**

    - How do measurements at different beam intensities impact pressure baseline (PBL) effects in clumped isotope mass spectrometry?
    - Can we empirically account for PBL to reduce measurement time during a clumped isotope measurement?

Though these foci cover seemingly different topics, the underlying theme of this research lies in the use of innovative isotopic techniques to untangle the often mixed signals preserved in the geologic record. Whereas clumped isotopes can be used to deconvolve the combined effects of temperature and $\delta^{18}O_w$, Ramped PyrOx ^{14}C can be used to decipher chronologically relevant information from the mixed subglacial sedimentary record.

1.6 Dissertation Overview

This dissertation is divided into six chapters. The next four chapters are written as stand-alone manuscripts that have been published (Ch. 2, Ch. 4), are currently in review (Ch. 3) or are being prepared for peer-review (Ch. 5). As such, some overlap in material (most

notably project descriptions and methods) exists. This dissertation is articulated around the following chapters:

Chapter 2: Compositional and beam-size-dependent effects on pressure baseline in clumped isotope mass spectrometry (2019), published in *Rapid Communications of Mass Spectrometry*, outlines a newly developed empirical correction for background effects during the measurement of clumped isotopes in CO_2 gas derived from $CaCO_3$ minerals. The correction described in this chapter can be used to reduce analytical time for clumped isotope measurements.

Chapter 3: A framework for transdisciplinary ^{14}C science: Use of natural-level and ^{14}C-labeling in Antarctic field research has been submitted to *Radiocarbon*. In this chapter, we describe the successes and failures of a collaboration involving researchers who employ natural-level ^{14}C variations and researchers who apply ^{14}C-labelled materials at levels elevated above natural abundances. As transdisciplinary science progresses, especially in remote field science in Antarctica and elsewhere, it becomes increasingly important to overcome logistical obstacles impeding the maximally successful outcomes for each proposed project. This work will have long-ranging importance for researchers working on ships, at shared research stations, and in remote field locations.

Chapter 4: Mid-Holocene grounding line retreat and re-advance at Whillans Ice Stream, West Antarctica (2020) published in *Geophysical Research Letters* details the first application of Ramped PyrOx ^{14}C to grounding-line-proximal sediment samples. Sediments in this setting reflect a mixture of ages spanning millions of years, but we identify evidence for a Holocene input of organic carbon to the subglacial environment. This work, in particular, highlights the utility of Ramped PyrOx ^{14}C for dating the small amount of autochthonous carbon included in subglacial sedimentary archives.

Chapter 5: The origin, age, and cycling of carbon beneath the West Antarctic Ice Sheet includes work that is currently in preparation for peer-review. In this chapter, I apply Ramped PyrOx ^{14}C and Monte Carlo simulations of isotopic spectra

(^{14}C, δ^{13}C) to assess the timing and extent of Holocene grounding line retreat along the Siple Coast of West Antarctica. Sediment OC ^{14}C is compared to other carbon reservoirs in the subglacial system [dissolved inorganic carbon (DIC), dissolved organic carbon (DOC), particulate organic carbon (POC), sedimentary carbonate minerals] to establish a conceptual model of the subglacial carbon cycle and address the role of marine input to the subglacial microbial ecosystem.

Finally, **Chapter 6** summarizes the findings of this dissertation and provides speculation about future directions of paleoclimate research that can build upon my work.

2 Compositional and beam-size-dependent effects on pressure baseline in clumped isotope mass spectrometry

2.1 Note to reader

This chapter was published in *Rapid Communications in Mass Spectrometry* with permission from John Wiley & Sons, Ltd. (See Appendix A). Section headers are consistent with the published version, but figures and tables have been reformatted for this document.

Citation: Venturelli, R. A., & Rosenheim, B. E. (2019). Compositional and beam-size-dependent effects on pressure baseline in clumped isotope mass spectrometry. *Rapid Communications in Mass Spectrometry*, 33(1), 140-148.

Author Contribution Statement: Both authors worked together in experimental design and conceptualization of the study. R. A. Venturelli prepared samples, analyzed data, and prepared the manuscript. B. E. Rosenheim provided edits and discussion that improved the manuscript.

2.2 Abstract

Rationale: The analysis of carbonate samples for the application of clumped isotopes to paleoclimate reconstruction necessitates smaller beam intensities. However, there is a relationship between beam intensity and pressure-dependent baseline (PBL), and therefore between beam intensity and the correction for PBL. Here we explain the relationship between PBL and beam intensity to develop a better correction protocol and an improved understanding of clumped isotope mass spectrometry.

Methods: We describe a beam size experiment using our Isoprime isotope ratio mass spectrometer in which samples of the carbonate standard IAEA-C1 were analyzed at 30, 50, and 70 nA to establish an optimal protocol and a new method to correct for PBL using the theoretical constraint of invariable Δ_{47} over a range of δ^{47} (bulk isotope composition) values. We also explore the effects of both over- and under-correction of PBL on equilibrated and heated gas samples to understand the effect of mis-correction of PBL.

Results: The results of our beam size experiments showed that a direct measurement of the baseline consistently introduced variability to measurements of the Δ_{47} of heated gases, equilibrated gases, and carbonate standards. These results necessitated a new protocol to account for PBL in our system. Our new approach flattens the reference frame line slope to 0 and, importantly, reduces the variability of data points about the heated gas line. We also describe, for the first time, an empirically derived description of the compositional effect of PBL.

Conclusions: A seemingly small change in our isotope ratio mass spectrometer resulted in a better understanding of PBL, for which we have developed an empirically based correction protocol to apply. Our new protocol has the potential to reduce analytical time for laboratories measuring PBL, and supports the need for carbonate mineral-based clumped isotope standards.

2.3 Introduction

For nearly seven decades, stable oxygen isotope ratios (δ^{18}O) have been utilized as a paleoclimate proxy (McCrea, 1950; Urey et al., 1951; Emiliani, 1955). Though oxygen isotopic compositions are dually dependent upon temperature and the composition of seawater ($\delta^{18}O_w$), the use of δ^{18}O in marine carbonates has been demonstrated as valuable for paleotemperature measurements when assumptions of seawater chemistry are robust and variability through time is well constrained or minimal (Cole et al., 1993; Linsley et al., 1994; Quinn et al., 1998; Felis et al., 2000). For cases in which $\delta^{18}O_w$ is less constrained, independent temperature

proxies [e.g., alkenones (Müller et al., 1998; Sachs et al., 2000; Volkman, 2000); coral Sr/Ca (Gagan et al., 1998); foraminifer Mg/Ca (Delaney et al., 1985; Anand et al., 2003; Elderfield et al., 2006)] have been applied to separate the effects of $\delta^{18}O$ from temperature. Each independent temperature proxy has been applied in concert with $\delta^{18}O$ to varying degrees of success due to discrepancies associated with vital effects and inter-laboratory comparability (Lea, 2003).

The measurement of multiply substituted isotopologues (clumped isotopes), specifically the mass 47 variant (Δ_{47}) of CO_2 liberated by orthophosphoric acid from the lattice of carbonate minerals, has recently offered another opportunity to deconvolve paleotemperature and past seawater chemistry within a single measurement. As opposed to Urey's heterogeneous isotope exchange reaction (Urey, 1947) carbonate clumped isotope thermometry is based on a homogeneous isotope exchange reaction in which the ordering of $\delta^{13}C$ and $\delta^{18}O$ in bonds of $CaCO_3$ is inversely correlated with temperature (Schauble et al., 2006). The mass 47 isotopologue ($^{13}C^{18}O^{16}O$ = 44.4 ppm, $^{13}C^{17}O^{17}O$ = 1.6 ppm, $^{12}C^{17}O^{18}O$ = 1.5 ppm; Eiler, 2007) of CO_2 derived from carbonate-bearing minerals is fundamentally difficult to measure due to the paucity of this particular multiply substituted isotopologue relative to isotopologues of masses 44–46. In order to make sufficiently precise measurements to differentiate variations in Earth surface temperatures, quite large samples (typically 3–15 mg) are often analyzed over a 2–4 h period (Ghosh et al., 2006; Passey et al., 2010; Zaarur et al., 2013). The protocol to monitor the stability of an instrument for clumped isotope analyses involves the measurement of CO_2 with differing δ^{47} (ratio of masses 47/44 in a sample relative to that in a reference gas) compositions that have been driven to a stochastic distribution of isotopologues by heating to 1000°C for a minimum of 2 h. These data are used to construct a heated gas line of δ^{47} versus Δ_{47} values, used to correct for any "non-linearities" (e.g. a linear slope not equal to zero) present when δ^{47} compositions vary on the scale of 20–30‰ for any of the contributing isotope ratios (Eiler & Schauble, 2004). It has been demonstrated that observed slopes greater than zero in both heated and equilibrated

gas lines (Huntington et al., 2009; Dennis et al., 2011) can be a result of both analytical and mathematical discrepancies (He et al., 2012; Bernasconi et al., 2013; Rosenheim, Tang, & Fernandez, 2013; Schauer et al., 2016). The accuracy of clumped isotope analyses is complicated by the presence of a negative background effect ('pressure baseline', PBL) observed on Faraday cups when gas is admitted to the source of a mass spectrometer (He et al., 2012; Bernasconi et al., 2013; Rosenheim, Tang, & Fernandez, 2013). Since the first account of PBL (He et al., 2012), a number of correction attempts have been discussed. Whereas some utilize a linear regression from the correlation between the major beams and minor beams to remove the nonlinearity effects of the mass spectrometer (He et al., 2012; Bernasconi et al., 2013) others have demonstrated the ability to perform a direct off-peak measurement of PBL, while gas is being ionized in the source but directed spaces between Faraday cups, to remove this effect (Rosenheim, Tang, & Fernandez, 2013; Müller, Fernandez, et al., 2017; Müller, Violay, et al., 2017; Meckler et al., 2014). Our work sheds further light on PBL, allowing us to build upon the original definition as we demonstrate that PBL appears to be a function of beam size, source geometry, chemistry and stability, frequency of measurement, and characteristics of individual mass spectrometers. Isotope ratio mass spectrometers ionizing at 10 kV potentials are typically used to measure clumped isotopes, but smaller systems have demonstrated both the ability to achieve the same precision and the need for better monitoring of instrument stability (Rosenheim, Tang, & Fernandez, 2013; Fernandez, Tang, & Rosenheim, 2014; Tang et al., 2014). For instance, smaller instruments [the Elementar Isoprime (Rosenheim, Tang, & Fernandez, 2013) and the Thermo Fisher Delta series (Yoshida et al., 2012)] have been shown to require accurate measurement of PBL for purposes of reproducibility of standards and samples because of the high, yet systematic, amount of variability in Δ_{47} over varying δ^{47} values (high "non-linearity"; (Rosenheim, Tang, & Fernandez, 2013). Successful clumped isotope measurements on the Isoprime 5 kV isotope ratio mass spectrometer have quantified PBL through direct off-peak measurements at a static point, 41V less than the accelerating voltage at peak center (Rosenheim, Tang, & Fernan-

dez, 2013). This practice has demonstrated an accurate assessment of PBL at a single, but large, beam intensity (100 nA), resulting in the use of this system for measurements and calibration of siderite (Fernandez, Tang, & Rosenheim, 2014) and calcite (Tang et al., 2014). These studies demonstrated that clumped isotope measurements could be reliably made and comparable reference frames could be produced from a system with an entirely different ion source, ion optics, and analytical technique from traditionally made measurements with a 10 kV MAT 253.

As the clumped isotope community continues to improve analytical precision while moving to smaller sample sizes (Schmid & Bernasconi, 2010; Hu et al., 2014; Müller, Fernandez, et al., 2017), we have further modified the Isoprime mass spectrometer by the installation of higher (10^{12} Ω) resistors on the Faraday cups configured to measure masses 47–49. These higher resistors facilitated increased sensitivity and decreased beam intensity, but also caused profound changes in the generation and, hence, the resultant measurement of PBL in our system. In this paper we present a new empirical, rather than measurement-based, PBL correction which we have preliminarily tested on an internal laboratory standard and gas reference frames spanning three separate analytical sessions. Furthermore, we apply what we have observed in our system to explore the effects of mis-correction of PBL on reference frames and transfer functions to the absolute reference frame. We share an improved understanding of compositional and pressure effects on PBL, which could become important as more laboratories using different mass spectrometer setups implement methods in which beam size is not held constant throughout a measurement.

2.4 Experimental

2.4.1 System

All isotopologue measurements were made on the compact 5 kV Isoprime isotope ratio mass spectrometer at the University of South Florida (USF, St Petersburg, FL, USA. The system was moved from the Stable Isotope Laboratory of Tulane University (SILTU, New Orleans,

LA, USA) and is described in detail in Figure 2 of Rosenheim, Tang, and Fernandez (2013). Measurements previously published from this system (Rosenheim, Tang, & Fernandez, 2013; Fernandez, Tang, & Rosenheim, 2014; Tang et al., 2014) required large sample sizes to produce ion beams of 100 nA. In order to facilitate the measurement of smaller beams (30–50 nA), and ultimately reduce sample sizes for clumped isotope applications, a new head amplifier was installed with increased resistance on all cups (Table 2.1).

Table 2.1: Resistor values for CO_2 isotopologue cups on the Isoprime system. Previously published values for the SILTU system and values after installation of a new head amplifier at USF

m/z	**Resistance at SILTU(Ω)**	**Resistance at USF(Ω)**
44	5.0 x 10^7	1.0 x 10^9
45	5.0 x 10^9	1.0 x 10^{11}
46	1.5 x 10^{10}	1.0 x 10^{11}
47	2.0 x 10^{11}	1.0 x 10^{12}
48	2.0 x 10^{11}	1.0 x 10^{12}
49	2.0 x 10^{11}	1.0 x 10^{12}

All gases (equilibrated, heated, and carbonate-derived) were passed twice through the glass vacuum separation line described in detail in Rosenheim, Tang, and Fernandez (2013). Briefly, this consists of two independent water traps, four loops each, cooled to -70°C with isopropanol (cooled to liquid–solid phase transition by liquid nitrogen) followed by a U-shaped glass Porapak and a silver wool trap cooled to -15°C using ethylene glycol (cooled to liquid–solid phase transition with liquid nitrogen). Heated (1000°C) and equilibrated (25 and 50°C) gases were prepared within four analytical sessions between August 2015 and May 2017 to construct independent reference frames. Each equilibrated and heated gas line consisted of three points covering a range of different bulk isotopic composition (Table 2.2).

Table 2.2: Description of ingredients for reference frame gases. "Tank CO_2" refers to gas sourced from a bottle purchased from an AirGas vendor in New Orleans, LA, USA ($\delta^{13}C$=-3.22‰VPDB; $\delta^{18}O$ = 25.46‰VSMOW) and "APICR" refers to Antarctic Peninsula Ice Core residual water

	Light	Middle	Heavy
Equilibrated	Tank CO_2 + APICR water; δ^{47} ≈-8 to -4‰	Tank CO_2 + DI water; δ^{47} ≈ 8 to 12‰	Tank CO_2 + DI water evaporated to 20% of original volume; δ^{47} ≈30‰
Heated	Fisher Scientific $CaCO_3$ (C-64, Lot 874601); δ^{47} ≈ -48 to -44‰	Tank CO_2 δ^{47} ≈ -3 to -2‰	CO_2 from headspace of the heavy equilibrated ampoule; δ^{47} ≈ 29 to 35‰

Each combination of CO_2 + H_2O was sealed in a borosilicate ampoule and placed in a water bath (set to 25 or 50°C) to equilibrate for at least 72 h before cryogenically separating CO_2 from H_2O. Each of the gases for heating was frozen into quartz ampoules and placed in a muffle furnace at 1000°C for at least 2 h to reach a stochastic distribution of isotopologues. The $\delta^{13}C$ values ranged between -41.02‰ and 2.05‰ VPDB and the $\delta^{18}O$ values ranged between 18.37‰ and 60.76‰ VSMOW. An internal carbonate standard (IAEA-C1) was reacted under vacuum with 2–5 mL of concentrated H_3PO_4 (104.1%) and analyzed to verify our reference frame and test our method of PBL correction. All reactions were carried out at 100°C by simple immersion of a two-legged McCrea-type reaction vessel in boiling water and continuously trapped in the first four-loop trap with liquid nitrogen throughout the reaction in order to minimize re-equilibration with water.

2.4.2 Mass Spectrometry

Purified samples were introduced into the bellows of the Isoprime mass spectrometer by being frozen into an adjacent microvolume and then expanded at ambient temperature. Pressures were adjusted on both sample and reference side to produce ion beams of 50 nA for the majority of samples, with the exception of a beam size experiment in which additional ion beams of 30 and 70 nA were produced from the same aliquots of gas (described further in the next section). Before each analysis, an accelerating voltage scan with a width of 120 V was performed with a step size of 0.27 V (0.1 s each) in the accelerating voltage. The entire process, which we refer to herein as pre-acquisition peak scanning, lasts 45 s, and is only performed once at the start of each analysis (Figure 2.1). For measurements, the ion beams of masses 44–49 were monitored for 20 s on both the reference and the sample side, with 12 s of data omitted after changeover valve switches. The sample gas isotope ratios were bracketed by measurements of reference gas (δ^{13}C = -3.22‰ VPDB; δ^{18}O = 25.46‰ VSMOW). In order to comparatively monitor PBL correction techniques, we employed the protocol outlined in Rosenheim et al. (2013) in which currents for all Faraday cups are measured when the m/z 44 beam is shifted 41 V lower in accelerating voltage for an off-peak measurement of PBL. This measurement occurs at the beginning of each sample and reference acquisition block, adding approximately 20 minutes to each measurement.

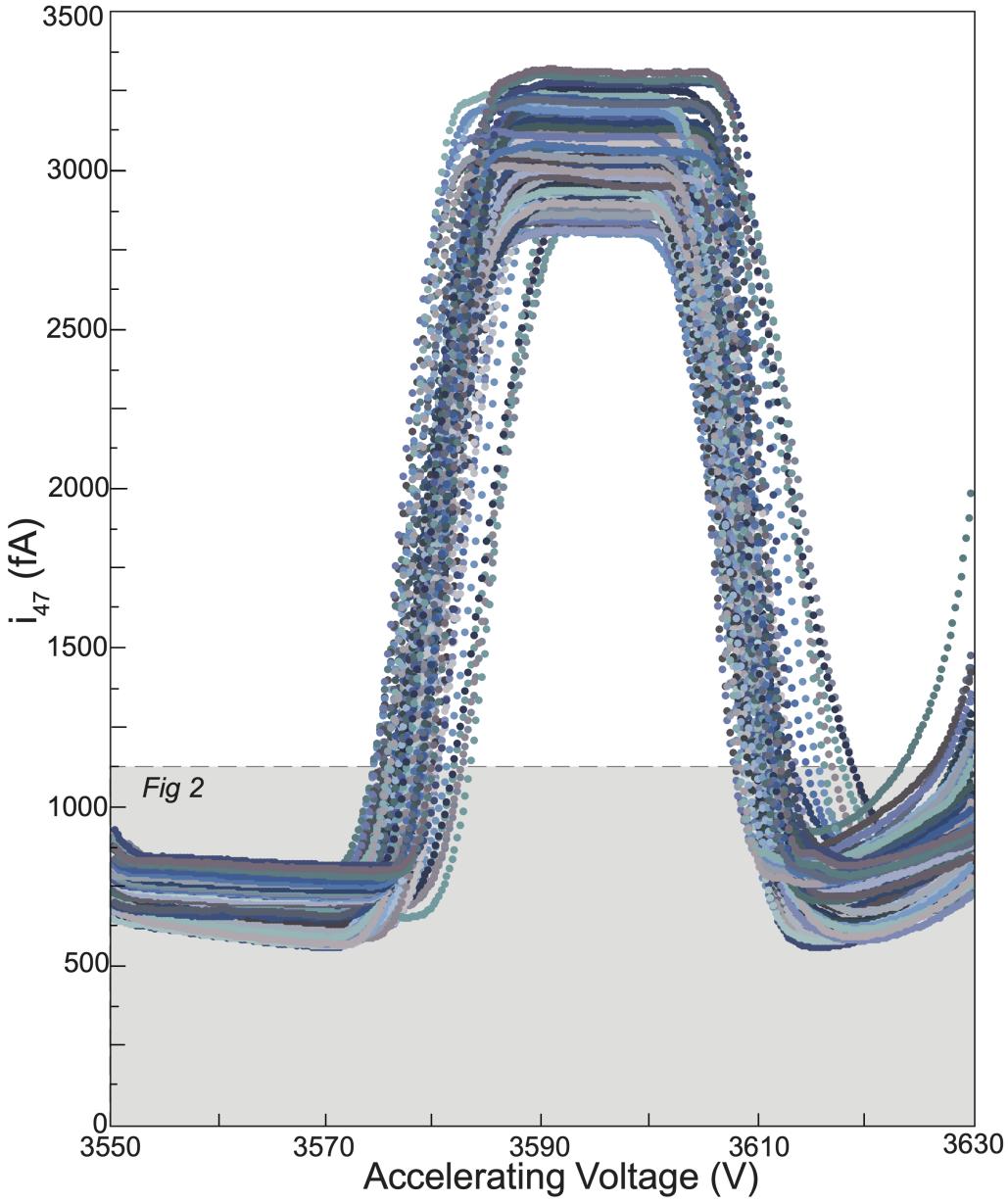

Figure 2.1: A compilation of pre-acquisition peak scans (n = 130), demonstrating the stability of our m/z 47 peak. The average peak center deviates by 3.1 V; however, the lowest point on the scan (peak scan minimum) varied by as much as 14.68 V

2.4.3 Beam Size Experiment

Two large samples (25 mg each) of IAEA-C1 were measured repeatedly during two analytical sessions (in September 2015 and January 2016) to determine the precision and accuracy for clumped isotope analyses in our updated system at different beam intensities. Repeated measurements of large samples from a single reaction and vacuum-line preparation were performed to isolate beam size as the sole variable inciting change on δ^{47} and subsequently Δ_{47} results. By analyzing each of the prepared IAEA-C1 samples at a m/z 44 beam of 70 nA (n = 3), 50 nA (n = 6), and 30 nA (n = 6) we were able to investigate whether or not PBL could be measured at a set, off peak, point, as well as the stability of this set point through time. During the September 2015 analytical session, the previously established protocol (Rosenheim, Tang, & Fernandez, 2013) was employed, in which on-peak signal measurements were alternated with 41 V off-peak PBL measurements. During the January 2016 analytical session, however, the off-peak PBL measurement location was adjusted to the lowest point on a pre-acquisition peak scan, similar to previously published methods from a different laboratory (Meckler et al., 2014; Müller, Violay, et al., 2017). This point will be referred to as the peak scan minimum (PSM) herein. The PSM remained stable at each beam size for the entirety of this experiment. Heated and equilibrated gases were regularly analyzed during the duration of these experiments. When previously accepted values of IAEA-C1 were not achieved with any of the PBL values from either the PSM or the 41 V monitoring points, an arbitrary set value for PBL was used to correct raw voltages to the accepted value. This practice was only performed on the IAEA-C1 samples in the beam size experiment to assess the degree of mismeasurement and failure to consistently achieve accuracy and precision for a known standard value. Eventually this value for the 50 nA samples (see Table 2.3) was able to be tied to an empirically derived multi-compositional intersection (MCI) point.

Table 2.3: PBL values (in fA) used to correct for each analysis of IAEA-C1 in our beam size experiment. The set value correction is the PBL value necessary to correct the standard to an accepted value. This point, at 50 nA, matches the intersection point of three heated gases of different bulk isotopic composition, with a forced varied background applied.

	41V correction (fA)	**PSM correction (fA)**	**Set value correction(fA)**
30 nA	752	770	822
50 nA	633	651	772
70 nA	493	539	739

2.4.4 Compositional PBL Sensitivity Test

Gas reference frame data were used to test the sensitivity of equilibrated and heated gas lines, as well as the subsequent transfer function, to an improper PBL correction. Observed differences (as much as 120 fA) between PBL correction methods in our beam size experiment were used to simulate extreme cases of over-correction and under-correction. Using the maximum observed differences of 120 fA, we applied the same offset to the entire range of reference frame samples in order to empirically derive the compositional effect (Meckler et al., 2014; Müller, Violay, et al., 2017) of PBL (Figure 2.5).

2.5 Results

Observation of pre-acquisition peak scans from over 100 analyses revealed that the PSM varies at beam intensities lower than 100 nA. At a large beam size (100 nA), the assumed PSM was probably stable ($n > 400$) at 41 V less than the accelerating voltage at peak center based on the achieved reference frame lines with slopes = 0 over broad compositional differences (Rosenheim, Tang, & Fernandez, 2013). This is only assumed because, with the success of the simple PBL measurements at that ion beam intensity, there was no impetus to measure pre-integration peak scans with every sample. We subsequently observed that this point changes as a function of m/z 44 beam size (Figure 2.2). Consistent with previous

observations (Meckler et al., 2014; Müller, Violay, et al., 2017), an inverse relationship exists between the PSM and beam size; i.e. PSM was driven lower by increasing the beam intensity. Consequently, the PSM can be found 7–11 V nearer the peak center than when a m/z 44 beam of 100 nA is used (Figure 2.2). From our beam size experiment and previous analyses performed at 100 nA (n > 400), we have established a relationship between PSM and beam size best described by a second-degree polynomial (Figure 2.3), although we have no theoretical basis for such a functional form and the number of points tested is not significant enough to constrain such a relationship. Nonetheless, the parabolic fit changes insignificantly between ∼50 nA and 0 nA, with a minimum offset of 28.7 V at 25.1 nA (where dV/dnA = 0). This modeled variability (approximately 3 V) over a large range of beam intensities is smaller than the variability recorded at 50 nA using the direct measurements of PSM.

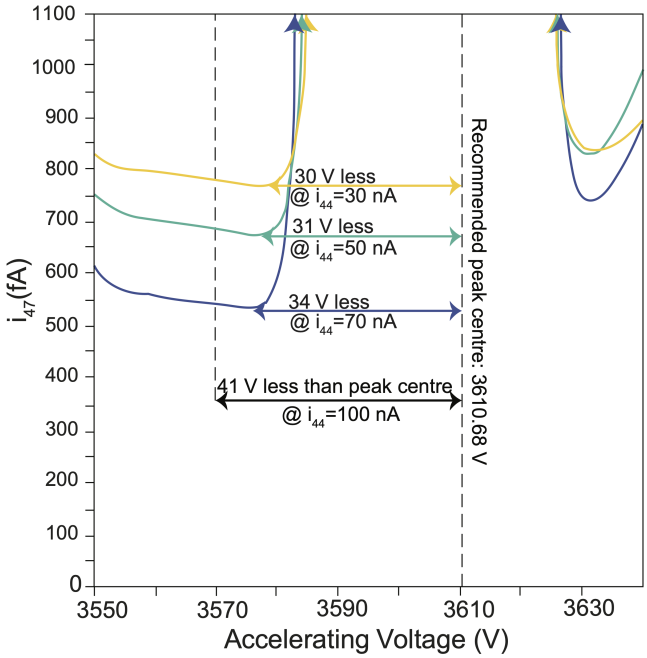

Figure 2.2: Close-up view of mass 47 peaks in the Isoprime system with major CO_2 beams (m/z 44) of 30, 50, and 70 nA. Traditional measurements in this system were performed at 100 nA and PBL was monitored at an AV adjusted to 41 V left of the peak center. Here we show that with a changing beam intensity, PSM shifts closer to the peak center

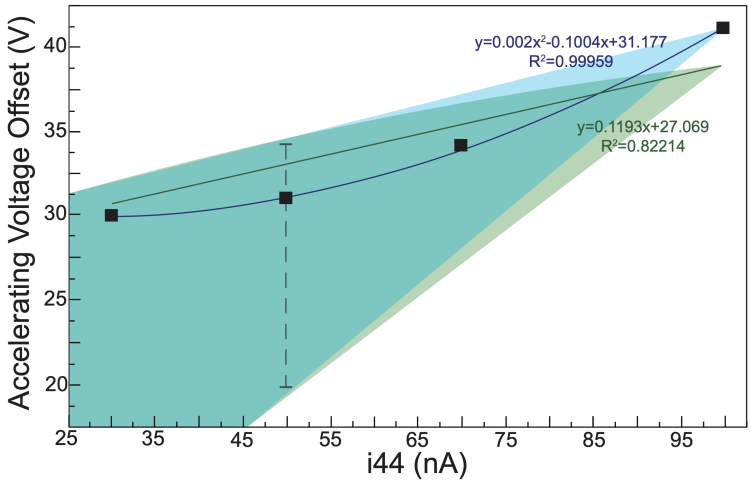

Figure 2.3: The relationship between major beam intensity and the offset in PSM from peak center. Lower beam intensities require lower offsets from the m/z 45 peak center (the mass to which the instrument is tuned). We have empirically fitted a polynomial (blue line) to these data, as it provided the best fit, from our beam size experiment (30 nA, n = 6; 50 nA, n = 6; 70 nA, n = 3) and the established methods of Rosenheim et al. (2013; 100 nA, n > 400). Because we have no theoretical basis for such a functional form, we also provide a linear fit (green line) through these data. With the addition of 120 analyses at 50 nA, error bars have been added to encompass the full range of accelerating voltage offsets between peak center and PSM. The shading indicates the full range of uncertainty based on a linear fit through the endpoint of each line (100 nA) and the high and low accelerating voltage offsets at 50 nA. The green shading encompasses the cloud of error associated with the linear fit, while the blue encompasses that associated with the polynomial fit

Despite an improvement in accuracy and precision when switching from a 41 V to a PSM correction for PBL, the overall accuracy did not reach acceptable levels (Figure 2.4). Our findings were consistent with those of Rosenheim, Tang, and Fernandez (2013) in which precision between measurements, regardless of beam size, was improved upon by applying a PBL correction. When PBL was monitored at the PSM, the signal on the empty Faraday cups was consistently and systematically greater than when PBL was monitored at 41 V off of the center. These two measurements differed by 18 fA for 30 and 50 nA measurements, and 46 fA for the 70 nA measurements. The improvement in precision of these measurements between PBL correction techniques was not linear for each beam size (Figure 2.4), further implying that both the 41 V and the PSM set PBL correction points do not sufficiently

eliminate PBL effects. The objective of this experiment was to constrain the position at which PBL is monitored and determine which beam size would reduce both sample size and instrumental variability. The outcome of this experiment did not allow us to assess this objective; however, it did raise a question of whether or not the correction for PBL must come from a direct measurement.

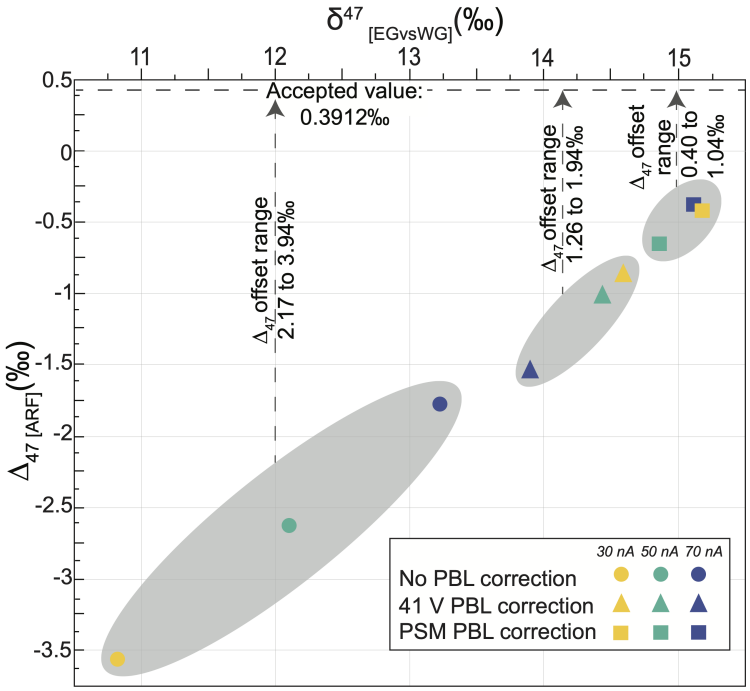

Figure 2.4: Mean Δ_{47} values obtained with different PBL corrections in the beam size experiment. An amount of 25 mg each of IAEA-C1 was measured in September 2015 and January 2016 at 30, 50, and 70 nA. Samples denoted by the 41 V symbol were corrected with the protocol described in Rosenheim, Tang, and Fernandez (2013) while the PSM correction refers to those points corrected with a value for PBL measured at the lowest point on a pre-analysis peak scan. It should be noted that, despite a lack of accuracy, a PBL correction improves measurement precision. Previously published values from Rosenheim, Tang, and Fernandez (2013) for IAEA-C1: $\Delta_{47} = 0.3912‰$

2.6 Discussion

Improving inter-laboratory comparability of measurements remains one of the most important tasks for the growing clumped isotope community to accomplish. Conventional practice prescribes measurement of CO_2 with different bulk isotope compositions (δ^{47} values) that

have been equilibrated at a set temperature (∼25°, and ∼50°C in our laboratory) or driven to a stochastic distribution of isotopologues by heating the samples to 1000°C (Wang et al., 2004). Measurements of Δ_{47} at different δ^{47} values are used to construct a reference frame of Δ_{47} versus δ^{47}, from which intercepts are plotted against theoretical values to construct an empirical transfer function to the absolute reference frame, on which all clumped isotope measurements can be compared (Dennis et al., 2011). It has been suggested that slopes >0 for heated and equilibrated gas lines (Δ_{47} versus δ^{47}) can be attributed to differences in correction for the influence of ^{17}O (Schauer et al., 2016; Daëron et al., 2016) and improper/absent correction for PBL (He et al., 2012; Bernasconi et al., 2013; Rosenheim, Tang, & Fernandez, 2013). To resolve these issues, the clumped isotope community has moved from a set of correction parameters used in the calculation of Δ_{47} (R^{13}_{VPDB}, R^{17}_{VSMOW}, R^{18}_{VSMOW}, λ) from Gonfiantini/Santrock parameters [0.112372, 0.0003799, 0.0020052, 0.5164; (Nier, 1950; Santrock et al., 1985; Gonfiantini et al., 1995)] to Brand/IUPAC parameters [0.0118, 0.038475, 0.0020052, 0.528; Schauer et al., 2016; (Daëron et al., 2016; Brand et al., 2010)] in an effort to improve inter-laboratory comparability mathematically. Where non-linearities cannot be resolved mathematically, they can be attributed to poor understanding of, and thus correction for, PBL (He et al., 2012; Bernasconi et al., 2013; Rosenheim, Tang, & Fernandez, 2013). Although not all laboratories apply a PBL correction, it has been demonstrated that both direct (He et al., 2012; Bernasconi et al., 2013; Rosenheim, Tang, & Fernandez, 2013; Müller, Fernandez, et al., 2017; Müller, Violay, et al., 2017; Meckler et al., 2014) corrections can be made and indirect [heated gas lines; (Huntington et al., 2009)]offsets can be observed.

Pre-acquisition peak scans, as well as a beam size experiment, described herein have revealed that despite an apparent relationship between major beam size and PSM (Figure 2.3), we are unable to tie the point in which PBL should be directly measured to a single physical location (Rosenheim, Tang, & Fernandez, 2013; Fernandez, Tang, & Rosenheim, 2014; Tang et al., 2014). Our inability to directly measure PBL at smaller beam intensities,

however, allows us to shed light on the effect of incorrectly accounting for PBL in clumped isotope measurements of a carbonate standard, reference frames, and transfer functions. When a 41 V PBL correction was applied in our beam size experiment, the Δ_{47-ARF} values of IAEA-C1 varied by as much as 0.52‰ from our laboratory accepted value, translating to an offset of 20.5°C between 30 nA and 50 nA analyses and 43.6°C between 50 nA and 70 nA analyses (Dennis et al., 2011). Using a correction tied to PSM (Meckler et al., 2014; Müller, Violay, et al., 2017) in our beam size experiment, the Δ_{47-ARF} variability of IAEA-C1 reduced to 0.22‰, although the 70 and 30 nA analyses yielded Δ_{47} values within error of one another. Despite an improvement in the precision of these measurements with a change in correction for PBL from 41 V to PSM, the measurements remain inaccurate, yielding Δ_{47-ARF} values as much as 1.04‰ lower than the published Δ_{47-ARF} value of 0.3912‰ for IAEA-C1 from our laboratory [(Rosenheim, Tang, & Fernandez, 2013); Figure 2.4].

Given that heated gas lines should be invariant in Δ_{47} regardless of bulk isotopic composition, it is possible to determine PBL in a system without direct measurement. If measured at a single beam intensity, on-peak signals for three different points (different bulk isotopic composition) on a heated gas line are corrected for a linear range of possible PBL values, the point at which the three samples intersect should theoretically correspond both with the Δ_{47} value for the temperature to which they were heated or equilibrated (Wang et al., 2004) and with the true PBL of the system during the period in which those gases were analyzed. We refer to this intersection point as the MCI point. In the case of our laboratory, we have applied this test by forcing a PBL correction ranging from 100 to 1200 fA, in a linear, stepwise fashion, on our raw m/z 47 signals. These values were well in excess of previously observed ranges of PBL values with different direct PBL measurement techniques. We illustrate this practice in Figure 2.6 with three heated gases each having a different bulk isotope composition (described in Table 3). We demonstrate that the calculated Δ_{47} values using this range of PBL values will intersect at a single MCI point, of which the abscissa

value is indicative of the actual PBL while the ordinate value at the MCI point corresponds to the Δ_{47} for the temperature at which samples were heated.

We suggest that the practice of varying background approach can be tested in systems outside of our laboratory by analyzing internal carbonate standards (such as IAEA-C1 in our laboratory) or potentially external carbonate standards [such as ETH 1–4; (Meckler et al., 2014; Müller, Fernandez, et al., 2017; Müller, Violay, et al., 2017; Bernasconi et al., 2018)] bolstered by heated and/or equilibrated gas analyses to find an instrument's or analytical session's individual MCI point. By performing a simple check with the varied background approach on heated gases analyzed at 50 nA surrounding the beam size experiment, we were able to confirm that the MCI point-derived PBL value (Figure 2.6) in fact matched the PBL necessary to correct the carbonate standard to our laboratory accepted value (50 nA set value in Table 3). By confirming that these values are in fact the same, for analyses performed at 50 nA, we can safely assume that the same would also be true at other beam sizes. PBL was always the lowest for the 70 nA analyses and highest for the 30 nA analyses, further supporting the idea that PBL is a function of beam size (Figure 2.4), regardless of which PBL measurement or correction technique was used. Differences between the PBL as measured at the PSM and MCI point used to correct each sample to an accepted value exist, but are not systematic. The greatest difference between PBL values for both approaches and set values exists for analyses performed at 70 nA, whereas the smallest difference exists for analyses performed at 30 nA. Furthermore, the values in our beam size experiment (Figure 2.4) yielded a consistent (but not systematic) negative offset from the previously published (Rosenheim, Tang, & Fernandez, 2013) value for IAEA-C1, indicating that the negative signal of PBL was not being fully eliminated and that we were effectively under-correcting for PBL. Furthermore, the order in which each PBL correction changed δ^{47}/Δ_{47} values was apparently random, suggesting that monitoring for PBL at a static point, whether it be 41 V or PSM, does not adequately eliminate PBL at lower beam intensities than 100 nA in our modified Isoprime system. The set correction for PBL applied to find the

accepted value of our carbonate standard was always greater than both the 41 V and the PSM corrections. However, it matched the MCI point correction at 50 nA. This confirms that the PBL correction that sufficiently removes the negative effects of pressure-dependent baseline comes from the varied background approach that we have presented herein, whereas all other approaches tested were consistently under-correcting for this effect.

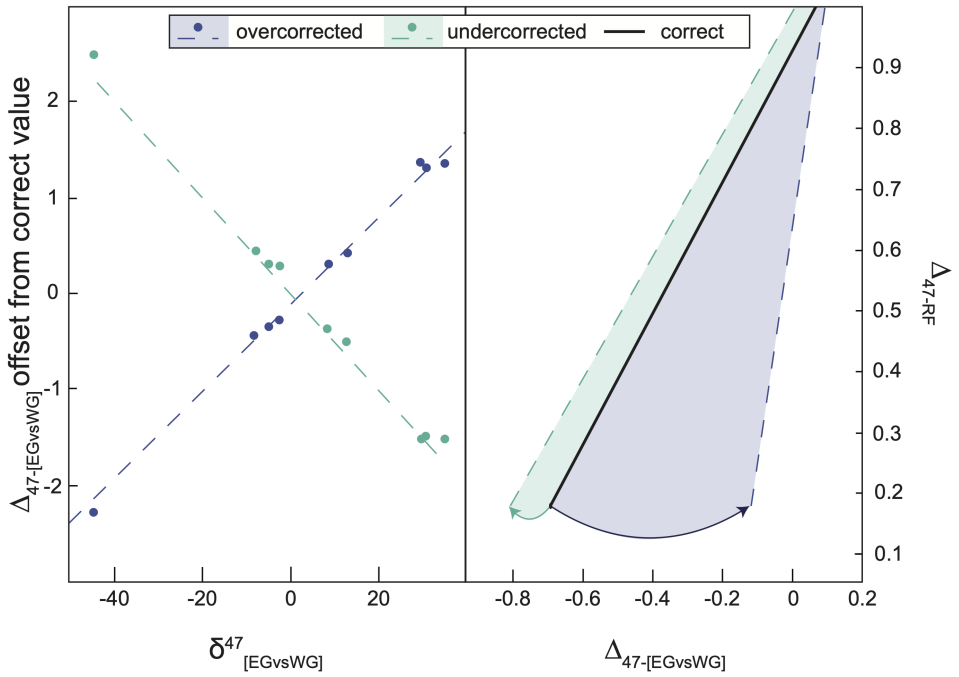

Figure 2.5: The effect of PBL mis-correction on reference frame samples. In the left panel the bulk isotopic (δ^{47}) value is plotted against the offset of the mis-corrected value from the known value of each equilibrated gas and heated gas from our reference frame. Because samples nearest the origin (δ^{47} value near 0) are less sensitive to changes in PBL than those further away, there is a compositional effect. In the right panel, the mis-corrected samples are plotted with a published reference frame to demonstrate that under-correcting for PBL results in a shallower slope, while overcorrecting yields a steeper transfer function slope

The femtoamp-magnitude offset in PBL between the correction methods was applied to existing data in order to gain an understanding of how mis-correction would affect reference frames, and ultimately the translation of clumped isotope measurements to temperature (Figure 2.5). When the same PBL offset was applied to every reference frame sample (three different points each on 25, 50, and 1000°C lines), we observed that samples nearest the

composition of our working gas (i.e., a δ^{47} near 0) were affected less than those further away from the origin (δ^{47} near +40 or -40), consistent with previous findings about the compositional PBL effect [(Müller, Violay, et al., 2017);Figure 2.5]. We calculate, for the first time, a compositional effect for PBL expressed as:

$$\Delta_{47} = 0.0456 \times \delta^{47} \tag{2.1}$$

when an over-correction is applied and

$$\Delta_{47} = -0.0503 \times \delta^{47} \tag{2.2}$$

when an under-correction is applied.

The compositional effect also affects the sensitivity of an empirical transfer function (ETF) to mis-correction for PBL. Where many laboratories have published ETF equations with a slope of around one (Dennis et al., 2011), an under-correction for PBL will yield a shallower slope and over-correction will yield a steeper slope. This observed change in slope has an effect on the sensitivity of Δ_{47} measurements, meaning that laboratories with an ETF of shallower slope are making less sensitive measurements, and are able to measure a potentially larger range of temperatures than those with a steeper slope. This is of particular importance when Δ_{47} measurements are being translated to temperature, and could possibly have an effect on clumped isotope-temperature calibrations.

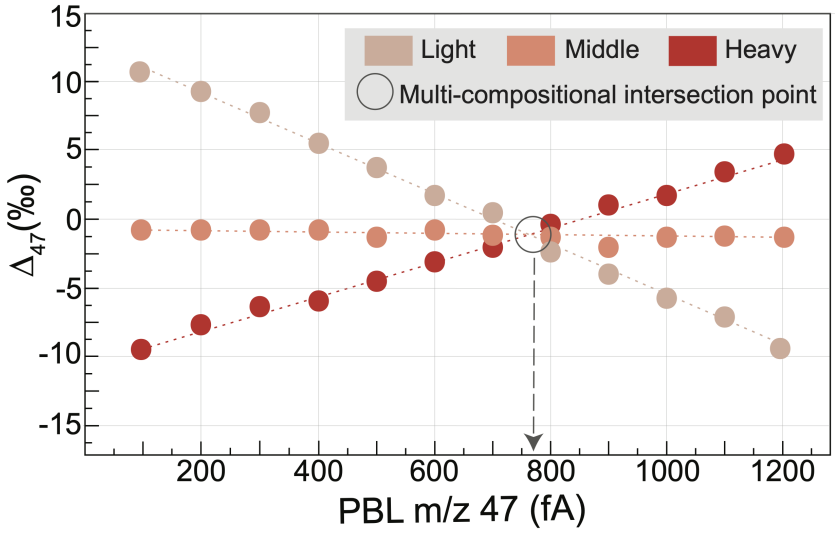

Figure 2.6: Using a set of samples with different bulk isotopic composition from a heated gas line, we correct for varied PBL values from 100 to 1200 fA. By plotting these heated gases together with varied background, we are able to determine the PBL in our system at the point of intersection

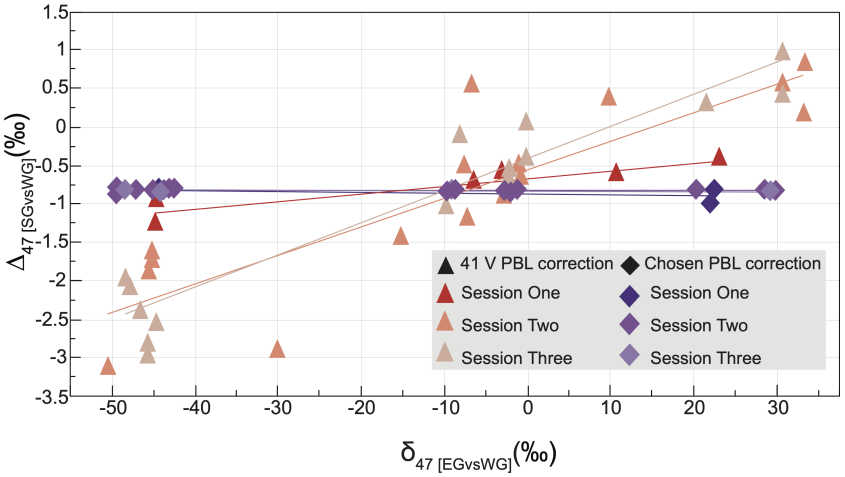

Figure 2.7: Heated gas lines corrected with the traditional 41 V PBL measurements and our newly established correction method. Using our new method, we are able to reduce the slope from 0.0295 ±0.017 to -0.0004 ±0.0007 and reduce the variability of the δ^{47} and Δ_{47} values of each of the categories of heated gases (light, mid, heavy)

In order to demonstrate that applying a PBL correction derived from the MCI point abscissa value would not only correct for the proper PBL in our system on a single com-

position carbonate standard, but also prove effective over a range of samples with a large range of bulk isotopic values, we have corrected samples from three heated gas lines during three separate analytical sessions (Figure 2.7). Using the abscissa MCI point for every three reference frame samples (Figure 2.6) as the value of PBL in our system during that time, we are able to reduce the slope from 0.0295 ±0.017 to -0.0004±0.0007. More notable, however, is a reduction in variability about the heated gas lines (Figure 2.7), demonstrating that this method of empirically deriving PBL improves both accuracy and precision better than directly measuring PBL at any set point tied to our peak scans. The standard deviation of the intercept throughout the three sessions is also reduced from 0.6700 to 0.0262, which will ultimately produce a more stable reference frame through time. To implement this approach, all unknowns in our laboratory are preceded and followed by an equilibrated or heated gas. Once three gases equilibrated to the same temperature have been analyzed at one beam size, the MCI point can be applied to correct for a set PBL value for all unknowns analyzed between the gases. The same may also be true for carbonate standards, in which a set PBL value can be used to correct a standard to its accepted value, and thus the unknowns analyzed adjacent to each standard. Although this is different from the use of carbonate standards proposed by Bernasconi et al. (2018), this method adds additional support to the necessity of there being well-established carbonate standards for clumped isotope analyses. The pre- and post-run standards, whether carbonate-derived or equilibrated/heated gas, if run within the same session, have never demonstrated differences greater than 7 fA in PBL voltages to achieve the previously published value of the given standard, regardless of composition. Differences of the order of 100s of femtoamps are, however, observed when analytical sessions are punctuated by major mass spectrometric changes (discontinuous filament or source cleaning and rebuild), lending insight to our claim that PBL may also be sensitive to changes in source geometry. The apparent success of this newly developed protocol in place of directly measuring off-peak has the potential to reduce instrument time by eliminating the off-peak measurement step and thus the sample size without making additional modifi-

cations to the instrument. It would require, though, that a laboratory analyze a potentially high frequency of equilibrated/heated gases and carbonate standards if they are not already doing so.

2.7 Conclusion

1. The desire to operate our instrument at smaller beam sizes to facilitate smaller sample sizes prompted a new understanding of PBL in the Isoprime system.

2. Our observations of the changes in PBL with respect to changes in major beam intensity support the ideas previously suggested by Meckler et al. (2014) and Müller, Violay, et al. (2017) that both a compositional and a pressure dependence are present.

3. Whereas fixing a point of PBL monitor to pre-acquisition peak scans has proven useful in the past, we have found that an empirical approach to account for PBL better serves our system at major beam intensities lower than 100 nA. This approach has the potential to reduce analytical time and ultimately further reduce sample size; however, it may increase the frequency at which a laboratory analyzes standards.

4. Our new approach to PBL correction helps us to reduce reference frame slopes and achieve similar transfer functions to previous studies from the Isoprime (Rosenheim, Tang, & Fernandez, 2013; Fernandez, Tang, & Rosenheim, 2014; Tang et al., 2014). We have demonstrated that this approach works both with gases and with our laboratory's internal carbonate standard, but it could easily be modified with standards used more widely in the clumped isotope community [ETH 1-4; (Meckler et al., 2014; Müller, Fernandez, et al., 2017; Müller, Violay, et al., 2017; Bernasconi et al., 2018)], supporting work to establish carbonate clumped isotope standards with community-wide accepted Δ_{47} values.

5. Although many laboratories still operate a 'stable' instrument and do not monitor for PBL or apply any PBL correction to their measurements, at the very least, our method may serve as a useful check on a longer time scale.

3 A framework for transdisciplinary radiocarbon research: Use of natural-level and elevated-level ^{14}C in Antarctic field research

3.1 Note to Reader

This chapter includes a manuscript under review at *Radiocarbon* by R.A. Venturelli, T. Vick-Majors, B. Collings, A. Gagnon, K. Kasic, M. Kurz, W. Li, J. Priscu, M. Roberts, B.E. Rosenheim, and the SALSA Science Team.

Author contribution statement: R. A. Venturelli (first author) worked with B. E. Rosenheim (senior author) on the protocol development that led to this manuscript. R. A. Venturelli carried out swipe testing in the field and prepared samples for AMS analysis at NOSAMS laboratory. T. Vick-Majors, W. Li, and J. Priscu provided context for ^{14}C-labelled tracer work. A. Gagnon assisted with swipe testing in the field. M. Kurz and M. Roberts enabled the analysis of swipe samples. B. Collins and K. Kasic provided photographs used in the figures herein. All authors provided edits on the manuscript prior to submission.

3.2 Abstract

Radiocarbon (^{14}C) is a useful isotopic tracer that can address a range of scientific research questions. However, contamination by unnatural levels of ^{14}C can be deleterious to natural-level laboratory workspaces and accelerator mass spectrometer facilities designed to precisely measure small natural variations in ^{14}C abundance. The risk of contaminating materials and facilities intended for natural-level ^{14}C with ^{14}C-labeled materials has dictated near complete separation of research groups practicing profoundly different radiocarbon measurements. Such separation can hinder transdisciplinary research projects, especially in remote

and isolated field locations (at sea, remote research stations), where both natural-level and elevated-level radiocarbon applications are being conducted. This paper outlines the successful collaboration between researchers making natural-level ^{14}C measurements and researchers using ^{14}C-labeled materials during a U.S. Antarctic Program subglacial lake access project in West Antarctica (SALSA, 2018–2019). We successfully carried out ^{14}C radiolabeling experiments within close quarters at the remote field camp without contaminating samples of sediment and water intended for natural-level radiocarbon measurements when adhering to our strict operating protocol. All sampled materials for both elevated-level and natural-level radiocarbon work were collected through a single, 0.4 m borehole drilled through 1087 m of ice. We present the collaborative protocol for maintaining natural-level radiocarbon cleanliness in a remote field camp as a framework for future transdisciplinary radiocarbon collaborations.

3.3 Introduction

Radiocarbon (^{14}C) is a powerful isotopic tool with applications that transcend disciplinary boundaries. Formation of ^{14}C occurs naturally and continuously in Earth's atmosphere when cosmic ray neutrons react with abundant atmospheric ^{14}N. Living organisms fix and consume carbon, incorporating small amounts of ^{14}C into their tissues. Death of the organism ends incorporation of ^{14}C and radioactive decay back to ^{14}N decreases the $^{14}C/C$ ratio relative to the modern atmosphere. In addition to dating applications, which interpret these changes in the $^{14}C/C$ ratio as age (e.g., Arnold & Libby, 1949); measuring variations of ^{14}C at natural levels has proven useful for tracing oceanic water masses (e.g., Broecker, 1982); chronicling geomorphological change such as burial-exposure histories (e.g., Goehring et al., 2011): and assessing the flux of oil spill-related petrocarbon to the seafloor (Chanton et al., 2014). Conversely, the use of ^{14}C-labeled materials (at concentrations elevated above natural abundances) is a valuable tool for studying carbon transformations in ecosystems. Samples collected from the environment are incubated with high specific activity ^{14}C-labeled

substrates, and the ^{14}C serves a tracer of biologically mediated transformations of carbon (e.g., Strickland & Parsons, 1972; Kirchman et al., 1985).

The dynamic range from natural to ^{14}C-labeled materials spans more than 10 orders of magnitude (Figure 3.1). To extend measurement capabilities to samples with exceedingly small amounts of ^{14}C (e.g., smaller sample sizes), the original counting techniques (i.e., Geiger counting, gas proportional counting, liquid scintillation counting) were replaced by accelerator mass spectrometry (AMS) techniques (e.g., Muller et al., 1977; Beukens et al., 1977; Nelson et al., 1977; Muller et al., 1978). The real advantage of AMS over counting techniques is sample size; whereas counting requires 1 g of carbon, AMS requires 1 mg or less. Measurement of $^{14}C/C$ ratios by AMS has grown more precise in recent years (Steier et al., 2004), extending low-end detection limits down to 10^{-16} atoms $^{14}C/C$ (Zhao et al., 2019). In contrast, the application of ^{14}C-labeled materials can be measured on the high end of the dynamic range making use of counting techniques. Labeling molecules with ^{14}C is useful for determining the rates of key carbon transformation processes through microbial biomass, including rates of photosynthetic primary production, chemoautotrophic carbon fixation, and rates of and respiration (Strickland & Parsons, 1972; Kirchman et al., 1985; Hill et al., 2013; Baltar & Herndl, 2019). The use of ^{14}C in these studies is advantageous specifically because of its high sensitivity, which makes it appropriate for use across a range of environments, including those with low productivity (Peterson, 1980). In addition, ^{14}C has a lower radiotoxicity to humans than other isotopic tracers. Whereas naturally occurring ^{14}C concentrations fall below $^{14}C/C$ atomic ratios of 10^{-12} atoms (modern atmospheric values $= 1.176 \times 10^{-12}$ atoms $^{14}C/C$), commercially available ^{14}C-labeled tracers may be as many as 12 orders of magnitude above natural levels.

Collaboration between researchers using natural-level radiocarbon and researchers using ^{14}C-labeled materials as a tracer carries high risk despite the growing transdisciplinary nature of science. Such collaboration could compromise the integrity of natural-level ^{14}C research (e.g., make old samples look anomalously young) and restrict the appropriate use of

^{14}C-labeling experiments through efforts to prevent cross-contamination. Even communication between scientists measuring natural-level ^{14}C and applying ^{14}C-labeled materials can be difficult, due to decades of work sequestered from one another. For instance, whereas natural-level workers measure ^{14}C/C ratios that are then converted to radiocarbon abundances expressed in terms of fraction modern (f_M) or radiocarbon years (^{14}C y), groups using ^{14}C-labeled materials above natural levels discuss abundances in units of total activity [e.g., disintegrations per minute (dpm), curies(Ci), becquerels(Bq)], concentration (e.g., Ci ml^{-1}) or specific activity (e.g., dpm mol of labeled compound). Conversions between the two sets of units are not straightforward without knowledge of sample size or measurement technique. Though complete separation of individuals using ^{14}C for dating and those using it for rate experiments may be feasible in conventional laboratories, it is often unavoidable in community shared spaces (e.g., research vessels, shared field stations, shared office spaces at remote research stations) where visiting groups carry out consecutive projects at either end of the radiocarbon measurement dynamic range. In such spaces, strict measures typically limit the use of ^{14}C-labeled materials to avoid the constant worry that a very small amount ($<$ 1 nL) of labeled solution or exposure to $^{14}CO_2$ will ultimately nullify the results of natural-level ^{14}C work. The need to separate natural-level workers from radiolabeling workers may preclude simultaneous transdisciplinary collaborations where transformative scientific discoveries may otherwise be possible. In many cases, opportunities to work together are not regarded as opportunities for potentially transformative science due to logistical difficulty and are passed up at the earliest stages of proposal building.

For collaborative projects in which research efforts rely dually on the measurement of natural-level ^{14}C abundances and the application of ^{14}C-labeled tracers, it is imperative to determine operating protocols that will reduce cross contamination without interfering with the integrity of either type of research. Here we summarize efforts in an Antarctic field expedition, wherein the research foci of different research groups revolved around subglacial carbon cycling over a number of timescales. Scientific questions regarding geologic history

relied on the measurement of ^{14}C at natural levels (e.g., Venturelli et al., 2020), whereas questions relating to cellular biosynthesis and respiration relied on the use of ^{14}C-labeled leucine and sodium bicarbonate (e.g., Christner et al., 2014; Vick-Majors et al., 2016). With only one access point into the subglacial environment and a limited time window for sample collection (Priscu et al., in revision), infrastructure, protocol, and mutual understanding needed to be developed in the planning stages of this project so that both groups could maximize successful research outcomes. We contend that these developments will be useful to a broad subset of communities using ^{14}C at natural and elevated levels, as well as communities using other analytes/contaminants over wide dynamic ranges (e.g., pulse-chase/nutrient research). We outline testing procedures for community laboratory spaces where ^{14}C-labeled materials have been applied in the past, provide remediation strategies for low-level contamination in community shared laboratory space, and outline operating procedures that resulted in a successful, collaborative research effort. These protocols provide a framework for continued success in future research initiatives.

3.4 ^{14}C Contamination Vernacular

"Contamination" can have a range of definitions that depend largely upon discipline, especially with the broad-ranging applications of ^{14}C measurements. Radiation control groups might consider something to be free of contamination when it falls below levels that are a concern to human health ($<10^4$ dpm/m^2), but such levels are still much higher than modern atmospheric ^{14}C concentrations (Figure 3.1). Throughout this paper we refer to contamination from the perspective of natural-level ^{14}C research, such that any substance containing a ^{14}C concentration greater than a Fraction Modern equal to one (>1 f_M, where f_M is the deviation of $^{14}C/^{12}C$ ratio in a sample from 95% of the ^{14}C concentration in 1950) is considered to be contamination. Although this definition includes ^{14}C elevations that occurred in the atmosphere during and after thermonuclear bomb testing in the 1950s which are also exploited by natural-level radiocarbon researchers, the natural-level work described here in-

volved only older-than-modern samples (Holocene through Oligocene). It is well-documented that samples containing high concentrations of radiocarbon, colloquially deemed "hot" samples, can be catastrophic for natural-level AMS facilities (Buchholz et al., 2000; Zermeño et al., 2004; Zhou et al., 2012). However, low-level contamination of older samples, for example Last Glacial Maximum (LGM-33.0 to 26.5 ka; Clark et al., 2009) sediment that may date to the Holocene (11.7 ka-to-present) after being contaminated, has the potential to result in a substantial misunderstanding of Earth's history because the contamination is not enough to render the result impossible (i.e., f_M>1). Such subtle risk, in addition to previously described high-level contamination that is harmful to AMS technology, is why we frame our perspective of contamination from a natural-level standpoint.

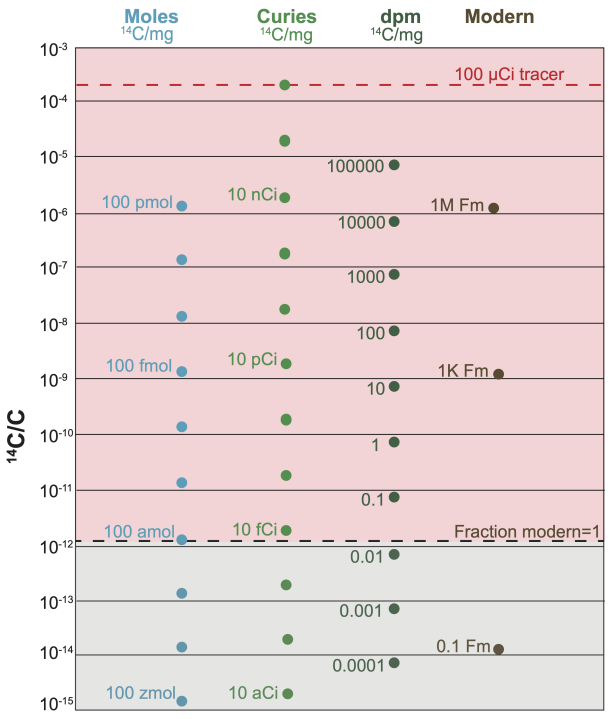

Figure 3.1: Clarification of differing radiocarbon units used by natural level and ^{14}C-labeling groups. The red dotted line highlights how a 100 μCi ^{14}C-labeled tracer (used during SALSA field work) translates to different ^{14}C units. The brown dotted line indicates the upper limit of natural level work. The grey shaded box demonstrates natural level radiocarbon concentrations, whereas the red shaded box indicates levels that we consider contamination throughout this chapter.

3.5 Evaluation of ^{14}C Contamination

Shared research facilities necessitate evaluation for ^{14}C contamination on surfaces, keypads, handles, floors, faucets, and other commonly touched areas before samples intended for natural-level ^{14}C research enter a space. In an effort to ensure the success of natural-level research after isotopic tracers have been used, the radiocarbon community employs two types of sampling for contamination, "SWAB" testing and "swipe" sampling. Measurement technique of these samples is largely a result of the contamination levels each method monitors for. Therefore, the threshold of background ^{14}C levels required for natural-level work in a shared space should be carefully assessed when choosing a contamination testing method. Because exposure to radioactive materials poses risk to human health, conventional testing can be performed by radiation control groups. However, this testing would not be sufficient to detect contamination that may be deleterious to natural-level ^{14}C research. For this reason, the Miami SWAB program was established in 1981 to assess ^{14}C remaining in laboratory spaces and research vessels after U.S. National Science Foundation (NSF)-funded use of radiolabeled tracers. Testing through the Miami SWAB program prescribes covering potentially contaminated surfaces with diluted detergent (Count-Off™) in 1 m^2 spaces, absorbing the solution with a sponge, and squeezing collected liquid into a bottle that may be submitted to the analytical facility (Tritium laboratory at University of Miami). In the Tritium laboratory, particulate material is removed by centrifuging, and the supernatant is analyzed with a liquid scintillation counter (LSC). Results are reported as the amount of radioactivity per unit area, and the SWAB program recommends remediation based on the level detected (Table 3.1).

Table 3.1: SWAB result levels and required remediation as prescribed by the Miami SWAB program (http://www.rsmas.miami.edu/groups/tritium/swab/ monitoring-of-shipboardcontamination/)

^{14}C detected(dpm/m^2)	**Remediation prescribed**
<50	No action required
50-10,000	Cleaning required before natural-level work
>50,000	Possible health hazard, radiation safety notified

Even when SWAB testing shows values as high as 10,000 dpm/m^2, human health issues are of no concern (Table 3.1). However, researchers using natural level ^{14}C abundances in their research usually opt for AMS-based swipe testing to be used to check for low-level contamination. Swipe testing employing AMS measurement of ^{14}C/C is an additional, but important, test for natural-level work because, even if a surface requires no remediation action (Table 3.1), it may still result in subtle contamination of natural-level samples that can lead to false conclusions. Contamination levels as low as 500 dpm/m^2 may be as much as 30 times greater than modern (f_M=1) depending on the total amount of carbon in the test. To test for ^{14}C contamination using AMS-based swipes, a pre-combusted (525°C, 4 hr) quartz fiber filter (Pall TissuQuartz 2.5 cm PALL 7200) is moistened with isopropanol and wiped over a surface. Unlike testing with the SWAB program, swipe testing is not confined solely to horizontal/flat surfaces, which allows for the testing of areas with high hand traffic (handles, faucets, buttons, keypads). Materials collected on quartz fiber filters are then converted to CO_2 by closed-tube in vacuo combustion in the presence of CuO and Ag, graphitized, and analyzed with an AMS system capable of detecting ^{14}C at natural levels, and slightly above natural radiocarbon levels in samples with low carbon content (i.e., tidy labs with little ambient dust). It should be noted that swipes from pristine surfaces, those with little-to-no carbon, must often be diluted with ^{14}C-free CO_2 in order to produce 1 mg of graphite for measurement (Table 3.2).

Table 3.2: AMS-based swipe result levels and first-order interpretation of results. It should be notes that "clean" laboratories (<1 f_M) are often characterized by swipe results of ∼0.6-0.75 $f_M$which comes from a combination of ambient dirt and dust. A lab that is hygienically very clean, lacking dirt and dust, may result in swipe results nearer 1 f_M due to a lack of ^{14}C free dust to dilute modern atmospheric values.

^{14}C detected (f_M)	**Interpretation**	**Action prescribed**
>2	Evidence of artificial ^{14}C exists	Test more surfaces and clean
>1 to 2	Suspect evidence of contamination	Clean surfaces and re-swipe
<1	No evidence of contamination	None

As part of the U.S. Antarctic Program, a combination of these methods has been used to assess ^{14}C contamination. Such protocols entail application of collection methods similar to swipe-testing, wherein a quartz fiber filter is moistened with isopropanol or Count-Off™ and wiped over a surface. However, the measurement of ^{14}C is performed with LSC due to the likelihood of a swipe sample from this environment containing levels of ^{14}C that could harm AMS equipment. We refer to this combination of testing as "LSC-based swipe testing" below.

3.6 Project Description

The Subglacial Antarctic Lakes Scientific Access (SALSA) Project was a transdisciplinary research effort centered on understanding the subglacial carbon cycle (Priscu et al., in revision). Researchers working on this project deployed to Mercer Subglacial Lake (SLM), 600 km from the nearest research station (McMurdo Station) during the 2018-19 Antarctic field season. During field operations, workers seeking to evaluate natural-level ^{14}C as well as researchers seeking to apply ^{14}C-labeled leucine and sodium bicarbonate as isotopic tracers in their experiments obtained subglacial water and sediment samples through a single hot water-drilled borehole (Priscu et al., in revision; Tulaczyk et al., 2014; Rack, 2016). In-field sample processing was carried out in 40 ft shipping containers converted into mobile

laboratories. Before SALSA fieldwork, the mobile laboratories used at our remote field site were used in a project that applied ^{14}C-labeled bicarbonate and leucine at concentrations 1.6×10^{10} times greater than modern (Christner et al., 2014; Vick-Majors et al., 2016, 2020). The challenges posed by collaborating in close quarters, and knowledge of the previous use of our laboratory facilities, rendered it imperative to assess contamination levels in laboratory spaces intended for natural-level ^{14}C work and establish protocol for groups with different research goals to work in close quarters at our field site. Planning for the evaluation of ^{14}C at different levels began as soon as the project was funded (August, 2016) and continued until field deployment (December, 2018; Figure 3.2). Herein we outline the iterative process of checking for contamination, developing protocol, remediating contamination, and monitoring ^{14}C levels during field operations.

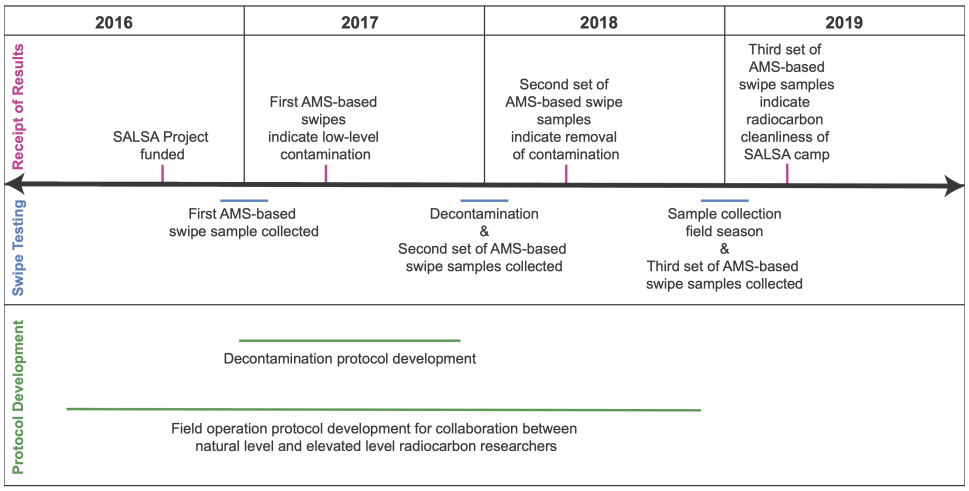

Figure 3.2: Timeline of preparation and operations for the SALSA Project. Here we highlight the multi-year period over which we prepared laboratory spaces and protocols for field operations. The extended timeline is a result of the logistical constraints involved in Antarctic field research and the inaccessibility of our field laboratories.

3.7 Protocol Development and Enactment

3.7.1 Initial AMS-based Swipe Testing and Results

Mobile laboratory containers transported to the SALSA field site had been used during a previous subglacial drilling effort (WISSARD) that employed radiolabeling techniques to assess microbial carbon transformations (described in detail in Christner et al., 2014; Vick-Majors et al., 2016). At the conclusion of WISSARD, LSC-based swipe testing resulted in <20 dpm/m^2 indicating that AMS-based swipe testing could be carried out. We performed AMS-based swipe testing on areas of high hand traffic (i.e., door handles, faucets, cabinets) and surfaces intended for sample and tool placement (i.e., bench tops, sinks, floor) in the laboratory intended for natural-level ^{14}C work during the 2016-2017 Antarctic field season, two years prior to SALSA field operations (Figure 3.2). On benches and floors, swipe testing was confined to 1 m^2 spaces to avoid tracking local-scale contamination throughout the entire laboratory space if it was present. We placed the individual quartz fiber filters used to perform each swipe test into pre-combusted glass scintillation vials (525°C, 4 hrs) immediately after performing each test. All swipe tests were sent to the National Ocean Sciences Accelerator Mass Spectrometry (NOSAMS) facility for analysis. Results of these initial AMS-based swipe tests indicated higher-than-modern (1.7 f_M) and near-modern (0.97 f_M) ^{14}C concentrations on faucet handles in the laboratory space intended for natural-level radiocarbon work. Other regions (benches, drains, door handles, and cabinets) in this laboratory were characterized by ^{14}C concentrations typical of ambient indoor laboratory air (0.5-0.7 f_M).

3.7.2 Contamination Remediation and Second Swipe Testing

We applied a chemically intensive cleaning protocol to the contaminated laboratory space, in part, due to the lack of radiolabel-usage record-keeping within the contaminated space. Radiolabeled substrates in the form of ^{14}C-leucine or $H_2{}^{14}CO_3$ had been used during WIS-

SARD, however, we had no records as to the mechanism of contamination (i.e. direct spill or secondary tracking from personnel and equipment moving between laboratory spaces). We divided the laboratory into sub-sections to avoid spreading any localized contamination, such as what we detected on the faucets. Sub-sections were limited to 1 m^2 on benches and floors, individual handles, and individual faucets. Each individual space was assigned cleaning materials (sponges, spray bottles, towels, garbage bags, gloves) that did not leave the designated space. Each section was wiped with a dilute acid (10% HCl) and isopropanol (100%) to remove potential contamination from inorganic and organic molecules, respectively. Surfaces were rinsed with soap and water and finished with laboratory cleaning solvents RBS 35™ and Count Off™ applied as a spray and wiped off with single-use paper towels. All materials were disposed of immediately in a waste container located outside the laboratory. We suggest a chemically intense cleaning protocol provides thorough remediation for contamination resulting from radiolabeled tracer in both organic and inorganic forms. Following full cleaning of the laboratory space, we performed another round of AMS-based swipe testing to determine the efficacy of the cleaning protocol. We performed one swipe test for each of the following locations: all door handles, all benches, all floors, and each individual faucet. Results from post-cleaning swipe testing demonstrated successful elimination of contamination in this laboratory space, specifically located on faucets, and reduced concentrations to 0.6-0.7 f_M. We were able to apply the lessons learned from our two years of AMS-based swipe testing and contamination remediation to develop a plan for field operations during the 2018 Antarctic field season (Figure 3.2).

3.7.3 Field Operations

During the two years of AMS-based swipe testing and contamination remediation (2016-2018, Figure 3.2), we developed a comprehensive plan for field operations during the 2018 SALSA Antarctic field season. Immediately following the cleaning and second round of swipe testing in 2017 (Figure 3.2), two laboratory facilities were set up at the field site and staged for

winter until they were opened in December 2018 for SALSA field operations. One laboratory was designated as a sediment laboratory space, in which natural-level ^{14}C work would be performed. A second laboratory was designated as the chemical laboratory, in which ^{14}C-labeled materials would be used for biological rate experiments (Figure 3.3). Primary wind patterns were observed and documented before configuration of the camp to ensure that the chemical laboratory was positioned downwind of the sediment laboratory. Personnel were assigned a workspace, and crossover of personnel between workspaces was prohibited. All materials, even laboratory waste, were confined to their designated space until the conclusion of field operations. Crossover was unavoidable, however, in common-use areas such as the mess tent where meals were served, the mechanical tent where tools and common field miscellany were housed, and lavatories.

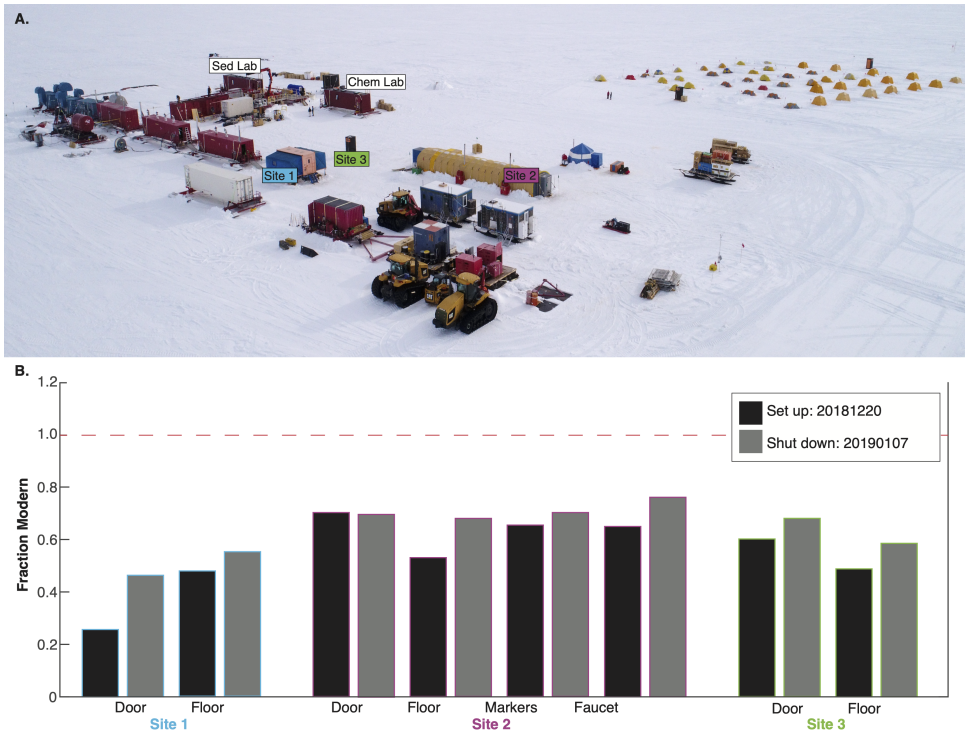

Figure 3.3: (A) A drone photograph of SALSA field camp (credit Billy Collins) with swipe locations designated by colored boxes. (B) Swipe results from common locations in the camp performed at the beginning of SALSA field operations and upon shut down of camp. The red dotted line indicates that all swipe results fell below concentrations considered contamination

In order to transport materials to and from the SALSA deep field site in Antarctica, boxes are packed by the science party and entered into the science cargo system, handled by cargo staff, unloaded by the staff on board the flight to the field site (Air National Guard or Ken Borek Air depending on aircraft used), and transported to field laboratories by camp staff. This chain of custody is well-documented and designed to minimize the flight resources required to service remote Antarctic camps, but it contains several steps in which a box could come into contact with a person or persons who have unknowingly encountered ^{14}C contamination. Therefore, any sample or supply material entering the lab with an unknown chain of custody from shipment to the field site was treated as contaminated. Materials were unboxed outside of the sediment laboratory, often in cold/windy conditions (<0°C), to avoid introduction of potential radiocarbon contamination that may have resulted from contact with chemical laboratory scientists. Where removal of an outer package was not possible, materials were wiped down with 10% HCl, 100% isopropanol, and Count Off™ before entering the sediment laboratory. All packaging and cleaning materials were placed onto Bench Coat™ to allow containment and cleanup. This minimized potential contamination from multiple people handling materials at the unpacking stage.

Any persons working in the chemical laboratory were strictly prohibited from entering the sediment laboratory. This included our education and outreach collaborators who were filming a documentary about the SALSA project; we asked that they dedicate certain clip-on microphones to chemical laboratory researchers and others to sediment laboratory workers, and that they film sequentially in the sediment laboratory first. Though it is possible to minimize cross-contamination of personnel by the removal of shoes, gloves, and outer clothing, we deduced that in high-stress field situations with a finite time of access for samples, as well as rapidly changing weather and the need to enter and exit the laboratories sequentially, the stakes were too high to risk such potential for crossover. As a result, interdisciplinary sample handling was complex. All sediment cores intended for natural-level ^{14}C work were packaged in the sediment laboratory and not opened until they arrived at the Oregon State

University Antarctic and Geologic core facility for sampling. All sediments to be shared between groups were sub-sampled as whole rounds from sediment cores or individual multi-core tubes in the sediment laboratory and transferred to members of the chemical laboratory in a neutral location. Water sampled for natural-level ^{14}C work was drawn from a new (not previously used in the field) 10 L Niskin bottle into pre-cleaned and combusted (525°C, 4 hrs) glass bottles. Water samples were transferred in secondary containment provided by the sediment lab in a neutral location. Until placement in their final location, containers were handled with gloved hands. All gloves were treated as contamination and disposed of following sample handling.

In order to assess the expected spread of contamination from the chemical laboratory, we developed an AMS-based swipe program to be employed during field operations. During this program, we performed swipe testing in set locations at the set up and shut down of camp, as well as every other day during field operations. We performed swipe testing in both communal (mess tent, mechanical facility, lavatories) and science-focused spaces (sediment laboratory, borehole control center); sampling both areas of high hand (faucets, doorknobs, bench surfaces) and foot (steps, doorways) traffic (Figure 3.3). Experiments applying ^{14}C-labeled materials were confined to the chemical laboratory, and personnel working with radiolabeled chemicals logged all applications. This swipe program was designed to test our working hypothesis that ^{14}C contamination would inevitably spread through our small camp. We expected that periodic swipe testing would allow us to chronicle a time-series of contamination events. Importantly, all SALSA scientists were involved in communication and protocol development during the planning stages of SALSA so that the sensitivity of natural-level work to ^{14}C contamination was at the forefront of our collaborative research efforts. Radiation safety protocols in the chemical laboratory intended to prevent the spread of contamination included the use of laboratory bench paper and secondary containment for all items used in the preparation of radioisotope assays, use of and frequent changing of gloves by radioisotope users, cleaning of benches with 10% HCl and Count-Off™ in

between experiments, and containment of pieces of potentially radioactive equipment such as pipettors and consumables such as tap in bags. In addition to these measures, radioisotope users always removed the Tyvek suits that were worn to protect subglacial samples from contamination before leaving the radioisotope area and did not re-use the suits. Swipe testing was performed every other day, and the only one instance of an elevated ^{14}C level was detected in the sediment laboratory doorway at a ^{14}C concentrations of 1.3 f_M. Time points for two subsequent testing periods after the elevated swipe (1.3 f_M) indicate a return to natural levels (0.5 f_M), likely due to snow-covered boots naturally diluting the already low-level contamination (Figure 3.4). The indication of elevated ^{14}C concentrations in a doorway but not on door handles or benches indicates that minor, ephemeral contamination was associated with foot traffic, but not with hand traffic, thus highlighting the importance of including floor contamination in protocol development.

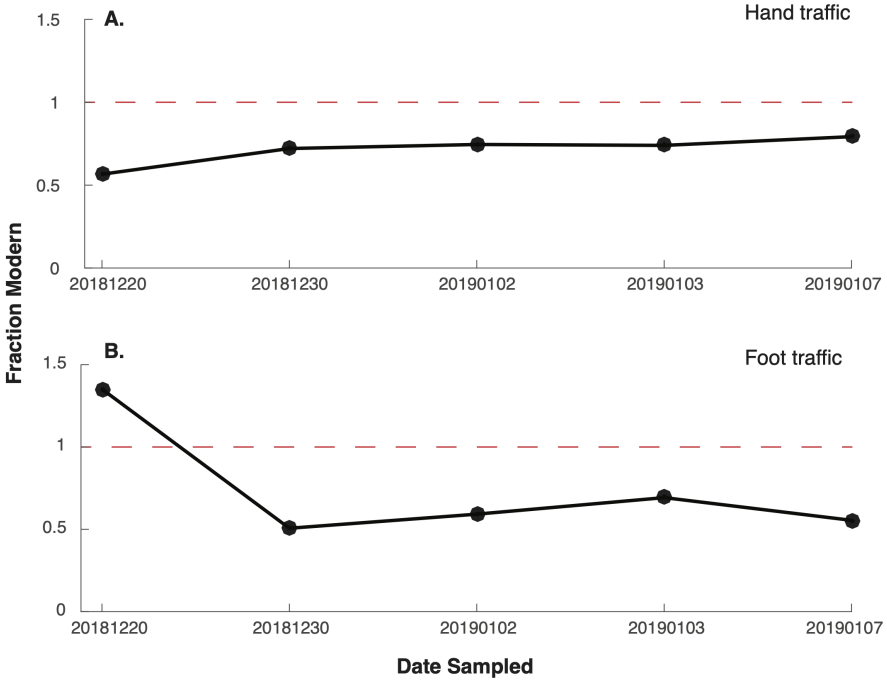

Figure 3.4: Swipe results from the sediment laboratory at SALSA field camp. The red dotted lines indicate that all swipe results fell below concentrations considered contamination after initial swipes of the sediment laboratory floor (20181220).

Avoiding contamination at a remote field site is important, albeit meaningless, if samples are subsequently exposed to above-natural ^{14}C levels during shipment or storage. We took extra precautions in the packaging of samples intended for natural-level work by packing in the sediment laboratory for northbound shipment. Sediment core materials were wrapped in multiple layers of plastic so that if handled by a contaminated individual, the outer layer could simply be removed without coming into contact with sampled material. This allowed samples to be stored in shared facilities that might not be cleaned to our (natural-level ^{14}C) standards without compromising the integrity of natural-level materials and without interruption of experiments using ^{14}C-labeled materials.

3.7.4 Contamination Assessment at McMurdo's Crary Laboratory

The Crary Laboratory facility, the largest shared laboratory facility in Antarctica, serves as the science and logistics center for the United States Antarctic Program (Peacock, 1992). Each season, many scientists conduct research, share and store equipment, and pack samples for shipment back to their home institutions in this facility. A portion of the research conducted in the Crary laboratory includes the application of highly concentrated ^{14}C-labeled materials. Because scientists, cargo, and materials were moving through this building, we performed AMS-based swipe testing to assess the risk of contamination. We restricted our testing to areas frequented by the SALSA field team (offices, shared spaces, lavatories) and avoided areas near the room where ^{14}C-labeling experiments are performed. Before our efforts, the Crary Laboratory had been LSC-based swipe tested, however, AMS-based swipe testing had not been performed to assess the fitness of this facility for natural-level work. We found ^{14}C concentrations of 0.72 to 1.8 f_M throughout Crary Laboratory. Elevated, but not unnatural, ^{14}C levels were found on scientific and administrative office door handles, main door handles, and library door handles. Above natural ^{14}C levels were found on the door handles of the main office (1.2 f_M) and the shared laboratory equipment door handle (1.8 f_M). Because swipe testing was not performed directly in or near the radiolabeling

and scintillation counting laboratory, the presence of contamination in areas of high hand traffic indicates that there is, indeed, some ^{14}C contamination being moved around Crary Laboratory.

3.8 Discussion and Conclusions

3.8.1 Was this level of protocol development necessary?

Early avoidance of contamination and success in carrying out simultaneous experiments with high levels (mCi) of ^{14}C-labeled material and natural-level ^{14}C work during this project begs the question of whether extensive protocol development was necessary. To illustrate how necessary our efforts were, we collected one extra water sample, against the guidelines of our protocol–from a 10 L Niskin bottle that previously entered the chemical laboratory (see section 4.4). The off-protocol sample (SLM1801-Cast 3-20181230) was immediately frozen for shipment and remained frozen (-20°C) until just before analysis. For analysis of DO^{14}C, the first step is normally the removal of DIC. In this case, we sampled CO_2 stripped from DIC with the addition of acid (4 mL of 85% phosphoric acid; McNichol et al., 2010). Following the removal of DIC, we sparged the sample with ultrahigh purity (UHP) helium gas and oxidized it with ultraviolet (UV) light (1200 Watt medium pressure mercury arc lamp) for four hours in a quartz reactor (following the methods of Beaupré et al., 2007; Griffin et al., 2010) to assess DO^{14}C. CO_2 evolved from DOC during UV oxidation was sparged with UHP helium and cryogenically purified. By sequentially analyzing both inorganic and organic pools of carbon from this same sample for ^{14}C content, we found DO^{14}C concentrations 0.496 f_M higher than our sample taken according to the guidelines of our sampling protocol (i.e. before the new Niskin bottle entered the chemical laboratory). Conversely, the DI^{14}C measurement yielded a result of 4 times modern (f_M= 4.2673). During field operations, ^{14}C-labeled sodium bicarbonate was used in uptake experiments within the chemical laboratory, and this sample demonstrates the ease with which the DIC of a lake water sample was contaminated by exposure to ^{14}C-labeled material. The DO^{14}C from the

same sample (0.1027 f_M), higher than our uncontaminated, within-protocol sample (0.0531 f_M), suggests that some carry over of contaminated DIC into the DOC pool is possible, despite the sample being stored frozen (Table 3.3). To assess whether significant carry over can be explained by microbial carbon fixation in storage (-20°C), we calculated what $DO^{14}C$ would be after 8 months of storage with rates of autotrophic carbon fixation similar to those measured in nearby SLW during the WISSARD Project (2.7 nmol C/d/L; Christner et al., 2014). The results of this calculation (Supplemental Text) indicate that persistence of rates of inorganic carbon fixation measured in SLW during sample storage would be enough to result in the elevated $DO^{14}C$ concentrations measured in our water sample collected off protocol.

Table 3.3: Table of results for dissolved inorganic carbon (DIC) and dissolved organic carbon (DOC) under three scenarios [on protocol (section 5.3), off protocol (after the Niskin entered the chemical laboratory), and theoretical (calculated)]

Sample identifier	**Sample notes**	**$DI^{14}C$ (f_M)**	**$DO^{14}C$ (f_M)**
SLM1801-Cast 2-20181229	Sample of lake water, collected in a new/clean Niskin bottle following protocol	0.0208	0.0531
SLM1801-Cast 3-20181230	Sample frozen for DIC and DOC preservation experiment, collected and preserved not following protocol	4.2673	0.1027
Calculated	Assuming a $DI^{14}C$ of 4.2673 f_M, we calculate a $DO^{14}C$ after 8 months of storage based on subglacial autotrophic C fixation rates and initial f_M of our within protocol sample	4.2673	0.1066

Both DI^{14}C and DO^{14}C results from the water sample collected off protocol compared to DI^{14}C and DO^{14}C results from the water samples collected following protocol confirm that contamination of ^{14}C was a risk to our experimental design and that our protocol was warranted. Whereas the DI^{14}C analysis of our sample collected off protocol yielded results obviously identified as contamination (f_M>1), the contamination in the DO^{14}C for this same water sample was not (f_M<1). However, when compared to the results of the DO^{14}C sample collected following protocol, and calculations simulating the persistence of microbial life in storage, (Table 3.3) the higher DO^{14}C can be explained by some carryover from contamination of DI^{14}C . This example highlights not only the risk of obvious contamination (f_M>1 observed in DIC), but also the risk of insidious contamination (observed in DOC) described section 2.

3.8.2 Summary of Recommendations

Our paper addresses the risk of transdisciplinary collaboration in field situations between natural-level ^{14}C researchers and researchers using ^{14}C-labeled materials with elevated concentrations and shows that establishment of rigorous contamination protocols can yield high integrity results for both measurements. The protocol for this type of work can be improved; our results are intended to encourage others to adapt philosophies, to further improve our practices, and to participate in, rather than avoid, such research opportunities. We make the following direct recommendations for researchers interested in pursuing natural-level ^{14}C research in collaboration with researchers using ^{14}C-labeled materials:

1. Assuming that personnel applying ^{14}C-labeled materials in their experiments are uninformed chemists is good for worst-case-scenario planning, but bad for establishing interpersonal relationships. The same can be said about scientists who use ^{14}C enriched substrates assuming that natural level ^{14}C scientists are being too protective. It cannot be overstated that establishment of rapport, respect, and understanding are extremely important to productive protocol development.

2. Begin developing operating procedures during the project planning stage and assign specific protocol leads to communicate the necessity of ^{14}C cleanliness to all researchers involved in the project. We attribute the success of our collaboration to the understanding developed in the planning stages of SALSA. It is important to tie operating protocol directly to the research objectives of disparate groups so that both natural-level and elevated-level ^{14}C workers can achieve proposed research objectives without detriment to their individual results. Development of operating procedures prior to 24 hour field operations during SALSA ensured minimal crossover between ^{14}C workers, thus reducing the risk of contamination.

3. Allow enough time to prepare laboratory spaces for natural-level ^{14}C work. Due to the remote nature of Antarctic research laboratories and field camps, iterations between testing, cleaning, and sampling take a full field season. This likely won't be the case on most UNOLS vessels or more accessible field stations.

4. Perform the appropriate testing in shared spaces. If prior use of ^{14}C-labeled materials is unknown, it may be necessary to perform SWAB testing prior to AMS-based swipe testing. We recommend performing AMS-based swipe testing of all laboratory surfaces where natural-level research will be carried out after SWAB testing results in ^{14}C levels <50 dpm/m^2. Ships in the UNOLS fleet typically undergo routine SWAB testing in coordination with use of radiation laboratories aboard; vessels operated by other national research programs or private vessels may not. The same can be said about other remote research stations.

5. Prepare with a full stock of cleaning reagents. We recommend a chemically intensive, multi-step cleaning process based on our success in reducing contamination in the SALSA laboratory space. The chemicals and cleaners chosen should remedy the types of label used and should not jeopardize other facets of the work.

Contamination is not always avoidable, but the success of our research program and cleaning protocol demonstrate that the spread of such contamination can be controlled in a way that allows maximum successful outcomes from transdisciplinary collaborations.

3.9 Supplemental Material

3.9.1 Contamination Calculations

Below we describe the calculation from section 6 and Table 3.3. Here we simulate a $DO^{14}C$ concentration that may result from a sample with contaminated $DI^{14}C$ if C-fixation rates measured in the subglacial environment persisted in frozen storage (Table 3.4)

Table 3.4: Variables used in calculations below to assess contamination in storage

Constant	**Measured value**
C-fixation rate	2.7 nmol C/day/liter
Within-protocol $DO^{14}C$ concentration	0.0531 f_M
Measured DOC concentration within protocol sample	51000 nmol C/liter
Measured $DI^{14}C$ in off-protocol sample	4.2673 f_M

First, we calculate the amount of DIC converted to DOC in a 1 L water sample assuming that observed subglacial C-fixation rates (Christner et al., 2014) persist in storage:

$$2.7\,\mathrm{nmol\,C\,d^{-1}L^{-1}} \times 240\,\mathrm{d} = 648\,\mathrm{nmol\,CL^{-1}} \tag{3.1}$$

Next, we determine the proportion of total DOC that is likely to have been assimilated from DIC, p_i, based on our assumption of rate.

$$p_i = \frac{648\,\mathrm{nmol\,C\,L^{-1}}}{51000\,\mathrm{nmol\,C\,L^{-1}}} = 0.0127 \tag{3.2}$$

Using a binary mixing model, we calculate what the $DO^{14}C$ would be if assimilation of contaminated DIC allowed for carry over of contamination into the DOC of our off-protocol

sample.

$$F_{m-calc} = p_i F_{m-i} + (1 - p_i) F_{m-o} \quad (3.3)$$

$$= (0.0127)(4.2673 f_M) + (0.9873)(0.0531 f_M) \quad (3.4)$$

$$= 0.1066 f_M \quad (3.5)$$

where the subscripts i and o are for inorganic (DOC derived from DIC in the bottle) and organic (the originally present DOC), respectively. If we assume that the contaminated assimilated C is being mixed into a sample of radiocarbon free water, the resulting $DO^{14}C$ could be calculated as follows:

$$F_{m-calc} = p_i F_{m-i} + (1 - p_{Ai}) F_{m-o} \quad (3.6)$$

$$= (0.0127)(4.2673) + (0.9873)(0) \quad (3.7)$$

$$= 0.0542 f_M \quad (3.8)$$

Using rates of dark ^{14}C-bicarbonate incorporation from SLW, the calculated off-protocol DOC in this sample, which could have resulted from the slow assimilation of obviously contaminated DIC (f_M= 4.2673), is alarmingly similar to the measured value of $DO^{14}C$ in the same sample (Table 3.4, Equation 3.6-3.8). At those rates of assimilation, which are likely higher than what actually occurred in the frozen sample bottle, 1.3% of the DOC we measured could have come from contaminated DIC. The sample we took following our standard protocol was collected during a cast of the Niskin bottle prior to any contact with the chemical laboratory, and DOC was measured at f_M= 0.0531 (Table 3.4). Both samples were frozen solid for storage and shipment in amber bottles, and the only possibility of microbial assimilation of DIC into DOC would have been in any small veins in which liquid water and concentrated salts were present. Furthermore, the sample was from SLM, which likely had lower cell counts and metabolic rates than SLW. Thus, our calculation represents

a high end of potential contribution from the contaminated DIC; if the rates of autotrophic assimilation were similarly an order of magnitude lower in SLM, then other factors may have contributed to the elevated amounts of radiocarbon in the off-protocol DOC sample.

In either case, two outcomes are important. First, the conundrum of whether to trust our outside protocol DOC values illustrates the insidious nature of ^{14}C contamination in settings such as these. In this case, we took ample precautions to break from protocol and sample from the Niskin bottle after it had been in the chemistry laboratory. Our off-protocol results suggest that freezing of samples may allow some limited exchange between the DIC and DOC pools. In this case, the amber bottle is not limiting to organisms adapted to assimilate inorganic carbon without (i.e., in an environment underneath 1 km of ice). However, salt concentrations were extremely low in this environment compared to open ocean samples. Given these competing factors, it is noted that we likely were able to see evidence of DIC-DOC exchange in a frozen sample because of the amplified signal produced by the contamination of the DIC in the outside protocol sample. This exercise shows that:

1. We have a DOC sample, sampled within our protocol, that likely avoids all sources of contamination and that

2. Our ^{14}C contamination prevention protocol was likely necessary despite the fact that our other success hides the reasons for such precaution.

3.9.2 Swipe Testing Data

We include all results from our swipe testing in tabular form (Table 3.5). Because the site locations within the sediment laboratory point to specific locations, we include a schematic of this 40 foot shipping container used for natural-level ^{14}C work (Figure 3.5)

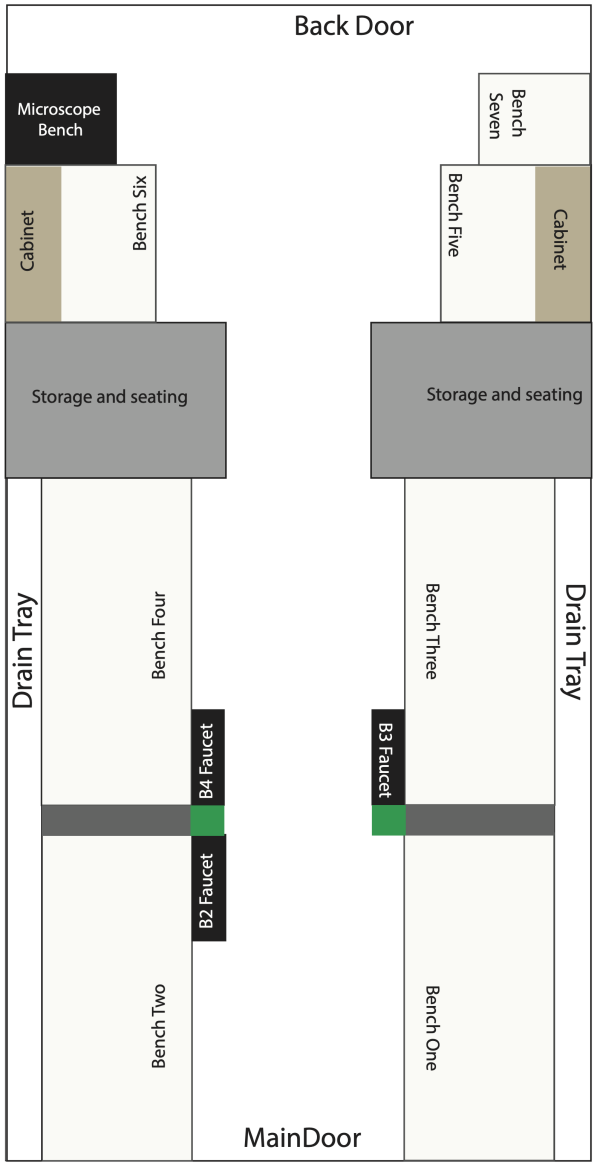

Figure 3.5: Schematic map of sediment laboratory used in SALSA Project field work. Specific site locations are labeled and correspond to locations of swipe testing for which results are listed in Table 3.5.

Table 3.5: All AMS-swipe testing performed in preparation for and during the SALSA field season (See Figure 3.2 for timeline of swipe testing). Herein we include the timeframe over which swipe testing was performed and analyzed as well as all results. We include the submitted sample names as well as site descriptors that correspond with our camp map (Figure 3.3) and our sediment lab schematic (Figure 3.5).

2016-2017 field season: Sediment Laboratory					
Date Collected	**Date Reported**	**Submitted sample name**	**Sample location**	f_M	$\pm\mathbf{1}\sigma$
November, 2016	1/4/17	1A, Counter, drain, counter front	Sediment lab bench one	0.6829	0.0017
November, 2016	1/4/17	1B, replicate 1A	Sediment lab bench one	0.6642	0.0018
November, 2016	1/4/17	2A, Counter, drain, counterfront 2	Sediment lab bench two	0.6905	0.0017
November, 2016	1/4/17	2B, Counter, faucet, door knob	Sediment lab bench two, B2 faucet, main door knob	0.5199	0.0016
November, 2016	1/4/17	3A, Faucet and sprayer handles	Sediment lab B4 faucet	0.5527	0.0017
November, 2016	2/21/17	3B, replicate 3A	Sediment lab B4 faucet	0.9662	0.0162
November, 2016	1/4/17	4A, Counter, drain, counterfront 3	Sediment lab bench three	0.5727	0.0016
November, 2016	2/21/17	4B, replicate 4A	Sediment lab bench three	0.5497	0.0015
November, 2016	1/4/17	5A, Counter, drain, counterfront 4	Sediment lab bench four	0.6315	0.0018
November, 2016	2/21/17	5B, replicate 5A	Sediment lab bench four	0.6832	0.0021
November, 2016	1/4/17	6A, Counter, counterfront 5	Sediment lab bench five	0.5176	0.0016
November, 2016	2/21/17	6B, replicate 6A	Sediment lab bench five	0.4952	0.0018
November, 2016	1/4/17	7A, Counter, counterfront 6	Sediment lab bench six	0.6494	0.0018
November, 2016	1/4/17	7B, Faucet and sprayer handles 2	Sediment lab B4 faucet and sprayers	1.6894	0.0045
November, 2016	2/21/17	8A, Counter, counterfront	Sediment lab bench seven	0.6611	0.0020
November, 2016	2/21/17	8B, Counter, counterfront	Sediment lab bench seven	0.7144	0.0019
November, 2016	1/4/17	9A, Counter-fronts	Sediment lab all fronts	0.5975	0.0016
November, 2016	2/21/17	9B, replicate 9A	Sediment lab all fronts	0.6031	0.0018
November, 2016	1/4/17	10A, Microscope table	Sediment lab Microscope bench top	0.4793	0.0015
November, 2016	1/4/17	10B, Wall cabinet handles	Sediment lab cabinet handles	0.4711	0.0016
2017-2018 field season: Sediment Laboratory					
Date Collected	**Date Reported**	**Submitted sample name**	**Sample location**	f_M	$\pm\mathbf{1}\sigma$
November, 2017	1/8/18	20171311-AllHandles	Sediment lab door and cabinet handles	0.6228	0.0174
November, 2017	1/8/18	20171311-AllBenches	Sediment lab all bench tops	0.2975	0.0017
November, 2017	1/8/18	20171311-B2Faucet	Sediment lab individual faucet B2	0.6033	0.0216
November, 2017	1/8/18	20171311-B3Faucet	Sediment lab individual faucet B3	0.6001	0.0254
November, 2017	1/8/18	20171311-B4Faucet	Sediment lab individual faucet B4	0.6928	0.0194
November, 2017	1/8/18	20171511-AllFloors	Sediment lab all floors	0.5089	0.0020
2018-2019 field season: SALSA camp					
Date Collected	**Date Reported**	**Submitted sample name**	**Sample location**	f_M	$\pm\mathbf{1}\sigma$
December, 2018	2/4/19	20181220-RCS-1, Sed lab doorhandle	Sediment lab entry door handle	0.5660	0.0167
December, 2018	2/4/19	20181220-RCS-5, RAC tent step	Mess tent foot step	0.5330	0.0018
December, 2018	2/4/19	20181220-RCS-6, Sed lab entry floor	Sediment lab entryway floor	1.3519	0.0218
December, 2018	2/4/19	20181220-RCS-7, RAC tent doorknob	Mess tent door handle	0.7013	0.0021
December, 2018	2/4/19	20181220-RCS-8, Restroom door handle	Restroom door handle	0.6007	0.0345
December, 2018	2/4/19	20181220-RCS-9, Restroom door step	Restroom foot step	0.4914	0.0498
December, 2018	2/4/19	20181220-RCS-10, MEC tent door handle	Mechanical tent door handle	0.2567	0.0020
December, 2018	2/4/19	20181220-RCS-11, RAC tent faucet	Mess tent faucet handle	0.6494	0.0132
December, 2018	2/4/19	20181220-RCS-12, Markers for borehole timelin	Mess tent dry erase markers	0.6579	0.0027
December, 2018	2/4/19	20181220-RCS-13, MEC tent door step	Mechanical tent dfoot step	0.4809	0.0155
January, 2019	2/4/19	20190107-RCS-1, Sed lab doorknob	Sediment lab entry door handle	0.7926	0.0027
January, 2019	2/4/19	20190107-RCS-5, RAC tent doorknob	Mess tent foot step	0.6837	0.0180
January, 2019	2/4/19	20190107-RCS-6, Sed lab entry floor	Sediment lab entryway floor	0.5547	0.0093
January, 2019	2/4/19	20190107-RCS-7, RAC tent doorknob	Mess tent door handle	0.6967	0.0023
January, 2019	2/4/19	20190107-RCS-8, Restroom door handle	Restroom door handle	0.6793	0.0191
January, 2019	2/4/19	20190107-RCS-9, Restroom door step	Restroom foot step	0.5894	0.0203
January, 2019	2/4/19	20190107-RCS-10, MEC tent door handle	Mechanical tent door handle	0.4635	0.0019
January, 2019	2/4/19	20190107-RCS-11, RAC tent faucet	Mess tent faucet handle	0.7607	0.0027
January, 2019	2/4/19	20190107-RCS-12, Markers borehole	Mess tent dry erase markers	0.7061	0.0023
January, 2019	2/4/19	20190107-RCS-13, MEC tent door step	Mechanical tent dfoot step	0.5547	0.0224
2018-2019 field season: Crary laboratory					
Date Collected	**Date Reported**	**Submitted sample name**	**Sample location**	f_M	$\pm\mathbf{1}\sigma$
January, 2019	11/19/19	#1 Room 219 door handle	Crary Lab office 219 door handle	0.9687	0.0029
January, 2019	11/19/19	#2 Room 208 office door handle	Crary Lab office 208 door handle	0.8859	0.0032
January, 2019	11/19/19	#4 Room 201 door handle	Crary Lab office 201 door handle	1.1824	0.0031
January, 2019	11/19/19	#3 Women's room door handle	Crary lab women's restroom door handle near SALSA offices	0.7222	0.0030
January, 2019	11/19/19	#5 Main enterance door handle	Crary lab main entrance door handle	0.8849	0.0028
January, 2019	11/19/19	#8 Library door handle	Crary lab library entrance door handle	0.9102	0.0028
January, 2019	11/19/19	#7 Admin office door handle	Crary lab administrative office door handle	0.9276	0.0030
January, 2019	11/19/19	#6 Lab consumable door handle	Crary lab shared science supply room door handle	1.7837	0.0048

4 Mid-Holocene grounding line retreat and readvance at Whillans Ice Stream, West Antarctica

4.1 Note to Reader

This chapter includes materials published in *Geophysical Research Letters* reprinted with permission from AGU Publications (See Appendix A).

Citation: Venturelli, R. A., Siegfried, M. R., Roush, K. A., Li, W., Burnett, J., Zook, R., et al. (2020). Mid-Holocene grounding line retreat and readvance at Whillans Ice Stream, West Antarctica. *Geophysical Research Letters*, 47, https://doi.org/10.1029/2020GL088476.

Author Contribution Statement: R. Venturelli (first author) prepared samples, analyzed data, and prepared the manuscript. K.A. Roush, W. Li, and J.C. Priscu provided samples. J. Burnett and R. Zook provided video data used in the interpretation of the depositional environment. A. Leventer provided diatom data. M.R. Siegfried and H.A. Fricker helped put paleoglaciological interpretations into glaciologic context. Useful input, discussions, and editing were provided by B. E. Rosenheim.

4.2 Abstract

Understanding ice sheet evolution through the geologic past can help constrain ice sheet models that predict future ice dynamics. Existing geological records of grounding line retreat in the Ross Sea, Antarctica, have been confined to ice-free and terrestrial archives, which reflect dynamics from periods of more extensive ice cover. Therefore, our perspective of grounding line retreat since the Last Glacial Maximum remains incomplete. Sediments beneath Ross Ice Shelf and grounded ice offer complementary insight into the southernmost

extent of grounding line retreat, yielding a more complete view of ice dynamics during deglaciation. Here we thermochemically separate the youngest organic carbon to estimate ages from sediments extracted near the Whillans Ice Stream grounding line to provide direct evidence of mid-Holocene (7.2 kyr B.P.) grounding line retreat in that region. Our study demonstrates the utility of accurately dated, grounding-line-proximal sediment deposits for reconstructing past interactions between marine and subglacial environments.

4.3 Introduction

The West Antarctic Ice Sheet (WAIS) is a marine-based ice sheet susceptible to rapid retreat and possible collapse in the face of projected warming (e.g., Mercer, 1978; Golledge et al., 2015; DeConto & Pollard, 2016). The marine ice sheet instability (MISI) hypothesis suggests that ice sheet grounding lines, where ice transitions from grounded to floating, are critical for large-scale ice sheet evolution (e.g., Hughes, 1973; Weertman, 1974; Schoof, 2007). Through both observations and modeling, it has been demonstrated that multiple processes can individually or cumulatively impact the stability of a grounding line on different timescales: sea level (e.g., Schoof, 2007); intrusion of warm water (Rignot & Jacobs, 2002), isostatic adjustment (e.g., Gomez et al., 2010; Whitehouse et al., 2019); underlying topography and bathymetry (e.g., Matsuoka et al., 2015; Halberstadt et al., 2016); and sedimentary accumulation (e.g., Alley et al., 2007; Simkins et al., 2018). Therefore, quantifying long-term stability of WAIS grounding lines can constrain estimates of future contributions of Antarctic Ice Sheet mass loss (DeConto & Pollard, 2016). Despite the long timescales over which grounding line dynamics can change, direct observations of grounding line dynamics have only been made over the past decade (e.g., Rignot et al., 2014; Joughin et al., 2016). Present-day sub-ice sediments provide an under-explored archive of grounding line retreat and advance, which can be leveraged to extend the record of grounding line stability into the geologic past.

Deglaciation of the Ross Sea since the Last Glacial Maximum (LGM) provides one of the best examples of significant Antarctic ice retreat in the geologic record and thus serves as an analog for the future of marine-based ice sheet sectors. Marine geological evidence on the Ross Sea continental shelf (e.g., Anderson et al., 2002; Mosola & Anderson, 2006; Anderson et al., 2014; Bentley et al., 2014; Simkins et al., 2018) and terrestrial evidence surrounding the Ross Sea (e.g., Stuiver et al., 1981; Hall & Denton, 2000; Hall et al., 2013; Spector et al., 2017) have been used to chronicle the pattern of retreat during the last deglaciation. Although this region has been heavily investigated, there remains an active debate surrounding the style and timing of deglaciation here. The paradigm of a "swinging gate" deglacial pattern persisted for several decades, wherein Roosevelt Island serves as a pinning point in the eastern Ross Sea, and the grounding line migrates southward along the Transantarctic Mountains in the western Ross Sea (Conway et al., 1999). More recently, periods of rapid Holocene retreat (Spector et al., 2017) and re-advance (Greenwood et al., 2018; Kingslake et al., 2018) have been suggested, and varied styles of retreat resulting from differences in physiography and bathymetry across the Ross Sea have been proposed (Halberstadt et al., 2016; Prothro et al., 2020).

Evaluating the full extent of deglaciation in the Ross Embayment requires dateable deposits from beneath the contemporary Ross Ice Shelf (RIS); however, thick ice cover, with 95% of RIS area between 211 and 764 m thick (Morlighem, 2019; Morlighem et al., 2020), limits direct access to these sediments. Before the Whillans Ice Stream Subglacial Access Research Drilling (WISSARD) Project, the only sediment samples retrieved from beneath RIS were collected at site J9 (Figure 4.1) as part of the RIS Project (Clough & Hansen, 1979). Sediments from J9, along with sediments from beneath the Siple Coast ice streams flowing into RIS (Figure 4.1), contain Miocene, Pliocene, and Pleistocene aged microfossils (Harwood et al., 1989; Scherer, 1991; Scherer et al., 1998; Coenen et al., 2019), as well as measurable radiocarbon (Kingslake et al., 2018). Knowledge that diachronous marine influence on subglacial sediments introduces a chronologic range on the order of millions

of years should thus raise caution on how time-diagnostic data from subglacial sediments are interpreted. We analyzed a grounding-line-proximal sediment core from Whillans Ice Stream to provide accurate chronological constraints on grounding line stabilization. We employed Ramped PyrOx (RPO) radiocarbon (^{14}C) dating, specifically designed to thermochemically deconvolve mixtures of acid-insoluble organic material (AIOM) and remove biases from glacially reworked carbon, to directly test a recent model-based hypothesis of Holocene grounding line retreat and re-advance (Kingslake et al., 2018).

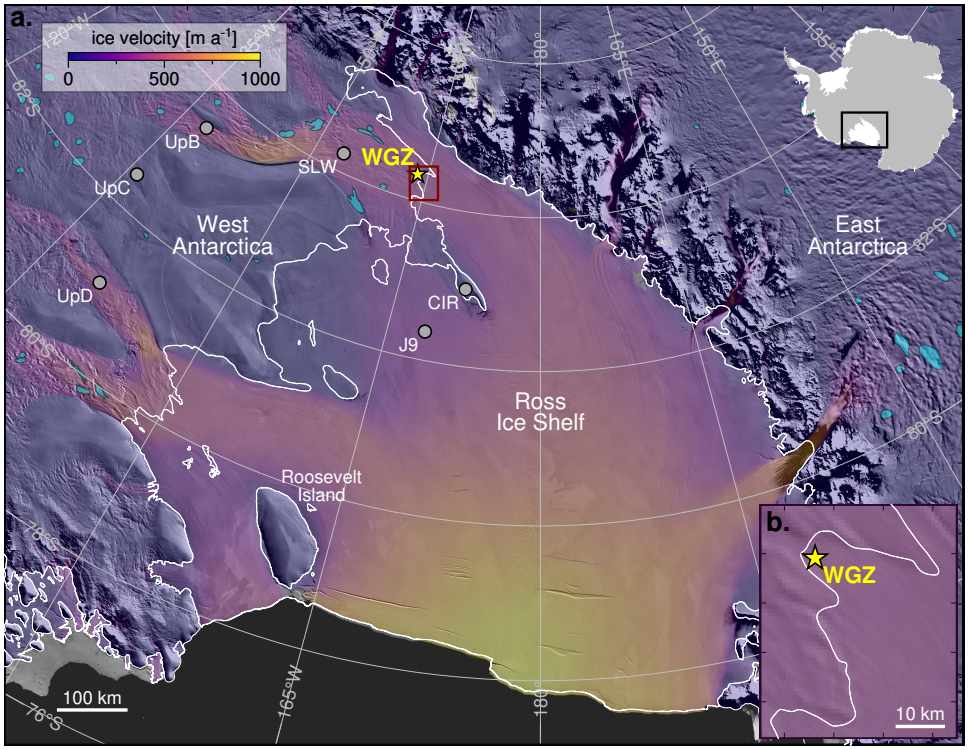

Figure 4.1: Map of study location. (a) Ross Sea sector (inset showing extent on Antarctica) with historical subglacial core site locations (gray circles) and Whillans Grounding Zone (WGZ) site (this study; yellow star). Ice velocity (Mouginot et al., 2019) overlain on an imagery mosaic (Scambos et al., 2007), with active subglacial lake areas (blue polygons; Siegfried & Fricker, 2018) and grounding line (white; Depoorter et al., 2013) indicated. (b) WGZ embayment showing core site relative to grounding line.

4.4 Study Location and Methods

4.4.1 Study Location and Borehole Operations

The Whillans Ice Stream grounding zone (WGZ) is one of the most studied areas of WAIS (e.g., MacGregor et al., 2011; Christianson et al., 2013; Horgan, Alley, et al., 2013; Horgan, Christianson, et al., 2013; Jacobel et al., 2014). WGZ is influenced by glacial and glaciofluvial processes, including sediment transport downstream by till deformation (e.g., Alley et al., 1986; Blankenship et al., 1986; Kamb, 2001), englacial sediment transport and deposition by basal melt (e.g., Christoffersen et al., 2010; Christianson et al., 2016), and transport of suspended sediment by the subglacial hydrologic system (e.g., Alley, 1989; Horgan, Christianson, et al., 2013). Though an actively accreting grounding zone wedge has been identified elsewhere in the Whillans Ice Stream system (Alley et al., 2007; Anandakrishnan et al., 2007), a comprehensive geophysical survey across the grounding line at our study site (84.33543°S, 163.61187°W; Figure 4.1) identified no evidence for grounding zone wedge deposition (Horgan, Christianson, et al., 2013). Instead, the sedimentary system accessed as part of the WISSARD Project (2014–2015) consists of recent sedimentation from basal melt underlain by subglacial till (Horgan, Christianson, et al., 2013). We collected a 70 cm long gravity core through a hot-water-drilled borehole (Tulaczyk et al., 2014; Rack, 2016) located ∼3 km downstream from the modern grounding line of Whillans Ice Stream (Begeman et al., 2018, 2020).

4.4.2 Geochemical and Microfossil Preparation

We determined total organic carbon (%TOC) of WGZ sediments with a Carlo-Erba NAN2500 Series-II Elemental Analyzer using a small aliquot of each sample. We prepared individual samples (5, 13, 40, and 62 cm) for radiocarbon dating with RPO, which employs a temperature ramp of 5°C per minute to leverage the thermochemical reactivity of AIOM within a sediment sample (Rosenheim et al., 2008). Aliquots of CO_2 from RPO preparation were

sent to the National Ocean Sciences Accelerator Mass Spectrometry (NOSAMS) facility for determination of $^{14}C/^{12}C$ ratios and $\delta^{13}C$. We prepared slides for individual samples (3, 32, and 64 cm) after the methods of Scherer (1994) and Warnock and Scherer (2014), which allows for a random distribution of diatoms to be settled over a known surface area for quantification of absolute diatom abundance (Section 4.9.1).

4.4.3 RPO Data Treatment

We normalized the thermograph (evolution of CO_2 as a function of temperature from the RPO process) of each sample to total pCO_2 produced in each run to compare the thermochemical stability of carbon separation at each core depth. We iteratively decomposed each thermograph into reaction components, assuming a Gaussian distribution of activation energies in the temperature domain within each component and using a nonlinear least squares technique to minimize residuals. To quantitatively relate information from thermographs to carbon bond strength and chemical stability, we modeled thermal activation energy distributions for each sample following Hemingway (2017) and Hemingway, Rothman, et al. (2017). We blank corrected all ^{14}C ages to account for uncertainty due to the RPO preparation process (Fernandez, Santos, et al., 2014, Section 4.9.2). We calibrated radiocarbon ages (^{14}C year) of low temperature RPO intervals to calendar years (year B.P.) using the Marine20 curve in Calib 8.2 (Heaton et al., 2020) and a local reservoir correction of 1,101 $\pm$ 120 years reflecting measured living amphipods from the site and prescribed uncertainties on reservoir ages due to different water masses intruding onto the Antarctic margin (Hall et al., 2010; King et al., 2018; Kingslake et al., 2018, Section 4.9.3).

4.5 Results

4.5.1 Thermographs and Activation Energy Distributions

Separation of AIOM with RPO results in qualitative information about thermochemical stability and quantitative information about the stability of organic carbon in these sedi-

ments (Figure 4.2). Samples analyzed at 5, 13, and 62 cm fit a four-component Gaussian model, whereas the 40 cm sample did not contain the low temperature Gaussian component present at other depths, fitting best with a three-component Gaussian model (Figure 4.2). The 5, 13, and 40 cm samples reacted at lower temperatures, represented by a large low temperature (350°C) peak, whereas the 62 cm eluted more CO_2 at a higher temperature (505°C). Thermal decomposition activation energy distributions Figure 4.2) reveal that RPO intervals range in activation energies across low (<150 kJ mol^{-1}), medium (150 $\leq$ E $<$ 185 kJ mol^{-1}), and high ($\geq$185 kJ mol^{-1}) energy ranges, demonstrating that subglacial organic carbon contains diverse bond structures rather than a homogeneous pool of refractory carbon (Hemingway et al., 2018). We separated the low-energy component in the lowest temperature interval of each of our samples, which yielded distinctly different activation energies from higher temperature intervals Figure 4.2). Though not useful for chronological purposes, higher temperature RPO intervals (RPO 2–5) were characterized by higher activation energies. Generally, these fractions contain less radiocarbon (i.e., are older) than other fractions (Rosenheim & Galy, 2012; Rosenheim, Roe, et al., 2013; Rosenheim, Santoro, et al., 2013; Williams et al., 2015), unless the low-energy radiocarbon from was from a frozen labile source like permafrost (Schreiner et al., 2014; Zhang et al., 2017) or volatile petroleum carbon (Pendergraft & Rosenheim, 2014). Combined with stable isotopic data, mid- and high-E data can be useful in Antarctic sediments for identifying sources and amounts of relict organic carbon in a grounding-line-proximal environment.

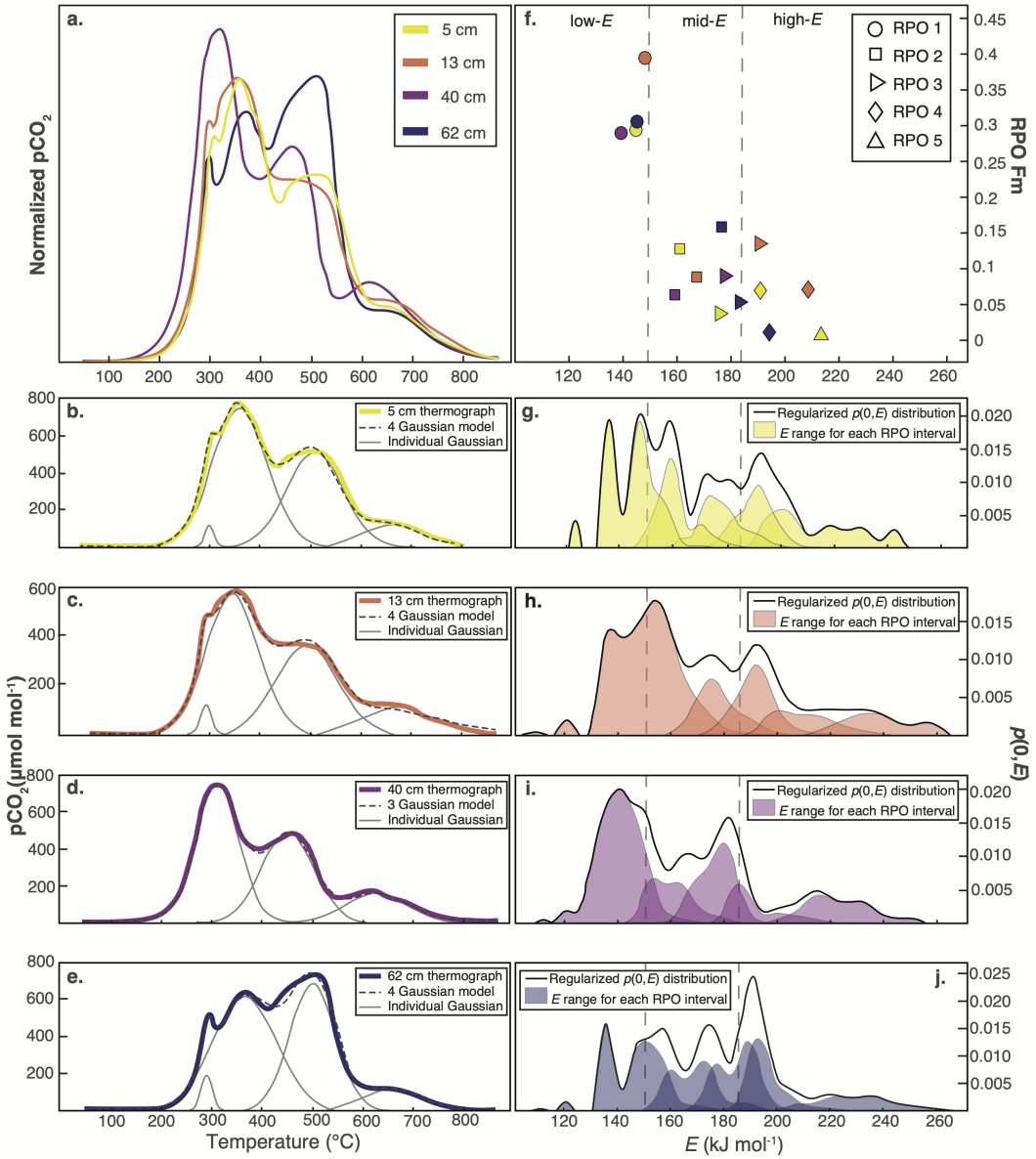

Figure 4.2: (a) Thermographs for all samples. Gaussian decompositions of thermographs for (b) 5, (c) 13, (d) 40, and (e) 62 cm core depths, showing modeled temperature ranges for individual carbon components. (f) Activation energy (E) versus fraction modern (f_M) for all RPO intervals with measurable ^{14}C activity. Dotted lines separate organic carbon into low-E (<150 kJ mol^{-1}), mid-E (150–185 kJ mol^{-1}), and high-E (>185 kJ mol^{-1}). Modeled energy distributions (p(0, E)) at (g) 5, (h) 13, (i) 40, and (j) 62 cm core depths show the range of energy distributions in each RPO interval.

Table 4.1: Reported fraction modern (f_M) is data directly from NOSAMS. Blank Corrected f_M values have been corrected to account for uncertainty resulting from RPO preparation. Italicized items are used to show that these ages are near the limits of measurable radiocarbon.

Sample	**Sample size (μmol)**	**Reported f_M**	**$\pm 1\sigma$**	**Blank corrected f_M**	**$\pm 1\sigma$**	**Age(^{14}C years)**	**$\pm 1\ \sigma$**	**δ^{13}C**
WGZ 5 cm: RPO 1	12.4	0.3046	0.0012	0.2952	0.0080	9,800	220	-27.6
WGZ 5 cm: RPO 2	19.1	0.1375	0.0012	0.1287	0.0064	16,450	300	-25.7
WGZ 5 cm: RPO 3	14.8	0.1031	0.0011	0.0910	0.0084	19,250	740	-25.7
WGZ 5 cm: RPO 4	12.5	0.0852	0.0012	0.0705	0.0101	21,300	1200	-25.1
WGZ 5 cm: RPO 5	24.2	0.0158	0.0011	0.0073	0.0057	39,500	6,300	-22.2
WGZ 13 cm: RPO 1	12.1	0.4032	0.0013	0.3961	0.0073	7,440	150	-30.3
WGZ 13 cm: RPO 2	13.5	0.1703	0.0010	0.1586	0.0085	14,800	430	-27.3
WGZ 13 cm: RPO 3	12.7	0.1492	0.0010	0.1363	0.0093	16,000	550	-27.1
WGZ 13 cm: RPO 4	12.4	0.0869	0.0009	0.0721	0.0102	21,100	1,100	-27.6
WGZ 13 cm: RPO 5	10.3	0.0170	0.0009	-0.0030	0.0132	>30,200	—	-22.9
WGZ 40 cm: RPO 1	13.4	0. 2992	0.0137	0.2904	0.0158	9,930	440	-29.0
WGZ 40 cm: RPO 2	15.2	0.0771	0.0008	0.0648	0.0084	22,000	1,000	-26.8
WGZ 40 cm: RPO 3	15.4	0.0510	0.0008	0.0383	0.0085	26,200	1,800	-26.1
WGZ 40 cm: RPO 4	13.6	0.0128	0.0008	-0.0024	0.0100	>32,400	—	-26.4
WGZ 40 cm: RPO 5	11.8	0.0122	0.0008	-0.0053	0.0116	>32,400	—	-21.2
WGZ 62 cm: RPO 1	13.6	0.3154	0.0012	0.3070	0.0073	9,490	190	-28.3
WGZ 62 cm: RPO 2	16.6	0.1005	0.0011	0.0897	0.0075	19,350	680	-27.2
WGZ 62 cm: RPO 3	17.5	0.0649	0.0011	0.0540	0.0074	23,400	1,100	-26.5
WGZ 62 cm: RPO 4	24.1	0.0199	0.0011	0.0114	0.0057	35,900	4,000	-25.6
WGZ 62 cm: RPO 5	16.6	0.0087	0.0012	-0.0038	0.0083	>35,000	—	-21.0

4.5.2 Geochemical and Diatom Data

Sediments from WGZ had low %TOC (0.03–0.21%; Section 4.9, Table 4.2) and low diatom abundances (500 to 1,000 valves per gram dry sediment; Section 4.9.1). The most commonly observed diatom species were *Denticulopsis simonsenii*, *Pyxilla reticulata*, *Stephanopyxis sp.*, and *Paralia sulcata*. None of the diatom specimens observed in our study were species that are common living taxa in the modern Ross Sea. Five aliquots of CO_2 at 5, 13, 40, and 62 cm resulted in a spectrum of isotopic data and ^{14}C ages for all samples (Table 4.1; Figure 4.3). The most thermochemically reactive aliquot of carbon was separated into the lowest-temperature RPO interval, containing 15% of the total sample at 5, 40, and 62 cm and 19% of the total sample at 13 cm determined by mass. Low-temperature aliquots for each sample contained the highest ^{14}C concentrations for each of the four spectra, resulting in ages from 9,900 to 7,400 ^{14}C years and lacking stratigraphic order (Figure 4.3). Values of $\delta^{13}C$ ranged from -30.3‰ to -27.6‰ VPDB in low temperature intervals. Radiocarbon concentrations decreased throughout the spectra, resulting in increasing ages and increasing $\delta^{13}C$ values with temperature (Table 4.1). High temperature intervals from 13, 40, and 62 cm samples resulted in ^{14}C sample activity less than the uncertainty of radiocarbon content and are reported as minimum ages after Stuiver and Polach (1977). Weighted arithmetic means of age spectra result in ages of 26,800–14,900 ^{14}C years, not in stratigraphic order.

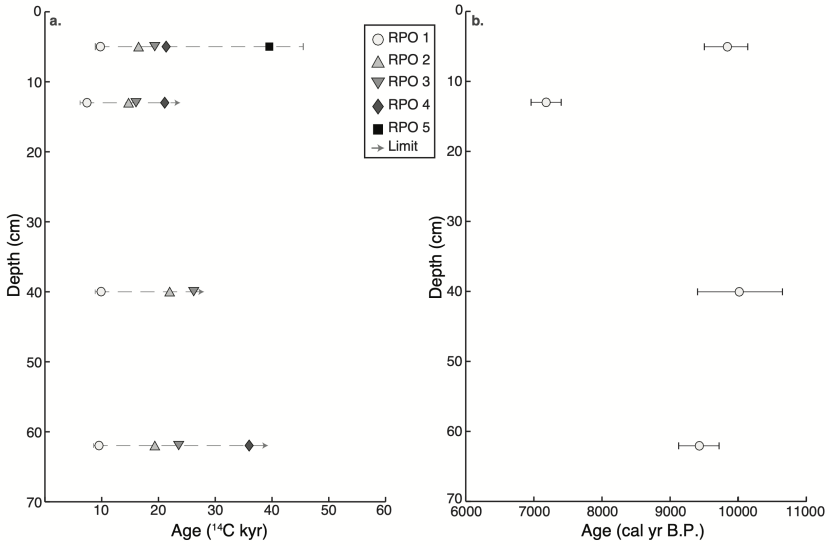

Figure 4.3: (a) RPO ^{14}C age spectra and (b) calibrated radiocarbon ages for low temperature RPO intervals. Where intervals are not indicated with a point in (a), radiocarbon content was less than the uncertainty of radiocarbon content or negative. We display these intervals with an arrow toward higher age to indicate limitations of reporting radiocarbon concentrations close to background.

4.6 Discussion

4.6.1 RPO Under Ice

The WGZ sedimentary system is composed of material influenced by glacial and sub-glaciofluvial processes (e.g., Christianson et al., 2013; Horgan, Alley, et al., 2013; Horgan, Christianson, et al., 2013; Vick-Majors et al., 2020). In a sub ice shelf setting, the proportion of pre-aged carbon transported from the continent (allochthonous material) is present in much higher proportion than carbon input from the marine environment (autochthonous material), with ages of these components reflecting the dynamic processes occurring before deposition (Subt et al., 2017). The application of RPO at WGZ builds upon previous work with Antarctic marine sediments to improve deglacial chronology by exploiting differences in thermochemical stability between autochthonous organic material and allochthonous organic material (Rosenheim et al., 2008; Rosenheim, Santoro, et al., 2013; Subt et al., 2016, 2017). In order

to interpret ^{14}C concentrations measured in low-carbon, subglacial sediments as a chronological constraint on grounding line retreat, separation of autochthonous organic material from high proportions of allochthonous material is imperative.

4.6.2 Comparison with previous ^{14}C Dating

We identify the presence of 9,900 to 7,400 ^{14}C year old (Figure 4.3) organic carbon in low temperature RPO intervals throughout our core. Recent work interpreted the presence of radiocarbon from bulk-dated subglacial sediment samples at WGZ, as well as upstream Whillans, Kamb, and Bindschadler ice streams, as evidence for exposure of the subglacial environment to marine water during the Holocene (Kingslake et al., 2018). This interpretation is consistent with stable carbon isotopic data in our study, falling within a typical range of marine organic material in the Ross Sea (Villinski et al., 2000). The lack of common modern Ross Sea diatoms observed here implies that marine incursion occurred under sub-ice-shelf conditions rather than with the onset of open marine conditions (Smith et al., 2019). Dissolved inorganic carbon beneath RIS can be fixed by chemolithoautotrophic ammonium oxidizing bacteria to produce new particulate organic carbon (Horrigan, 1981; Priscu et al., 1990). Therefore, the presence of radiocarbon in our sediments likely reflects the timing of this microbial process when the subglacial environment was exposed to marine water.

Weighted arithmetic means of RPO age spectra are comparable to bulk-dated ages from the same AIOM samples taken from riverine settings (Rosenheim & Galy, 2012) and the Bellingshausen Sea (Rosenheim, Santoro, et al., 2013); in highly detrital sediments, however, weighted arithmetic mean ages have been shown to result in slightly younger ages than conventional bulk dates (Subt et al., 2017). Bulk-dated samples from other WGZ cores resulted in ages from 28,600 to 20,200 ^{14}C year (Kingslake et al., 2018). Mean ages calculated from RPO age spectra in our study resulted in ages ranging from 26,800 to 14,900 ^{14}C years old. Younger calculated bulk ages for the same sediments may be explained by slight differences in pretreatment of material having a different effect on young labile organic

carbon, as preparation techniques can influence dating efforts (Bao et al., 2018). Combined with heterogeneous sedimentation in a low-carbon, ice-proximal depositional environment, small differences in extremely low ratios of $^{14}C/^{12}C$ can be expected when interpreted as ages, consistent with Subt et al. (2017). Nonetheless, low temperature RPO intervals here are 7,500 to 17,800 ^{14}C years younger than previously bulk-dated samples from WGZ (Kingslake et al., 2018).

4.6.3 Whillans Ice Stream Grounding Line Retreat

Isolation of low-energy bonded carbon in low-temperature RPO intervals demonstrates that we have minimized the amount of relict carbon incorporated in our dated samples, reducing geological uncertainty in dating grounding-line-proximal sediment. We calibrated our low temperature RPO intervals to calendar years (Figure 4.3) and interpret the mid-Holocene ages (7.2 kyr B.P.) as chronological constraints of grounding line retreat. The incorporation of marine carbon in these sediments supports the hypothesis that the upstream Whillans Ice Stream subglacial system was previously exposed to the marine environment. These results imply that the grounding line retreated beyond its current position in the mid-Holocene and subsequently re-advanced to the current position, rather than a progressive retreat of the grounding line in the Ross Sea since the LGM (Figure 4.4). Thus, the paradigm of a unidirectional retreat, pinned at Roosevelt Island at 3.2 kyr B.P. (e.g., Conway et al., 1999; Lowry et al., 2019), is not consistent with our results. WGZ RPO ^{14}C data support the model of grounding line and re-advance following the LGM (Greenwood et al., 2018; Kingslake et al., 2018). However, our dates from WGZ indicate that grounding line retreat occurred at least 2 kyr later, during the mid-Holocene, rather than the early Holocene (9.7 kyr B.P.) as simulated by Kingslake et al. (2018).

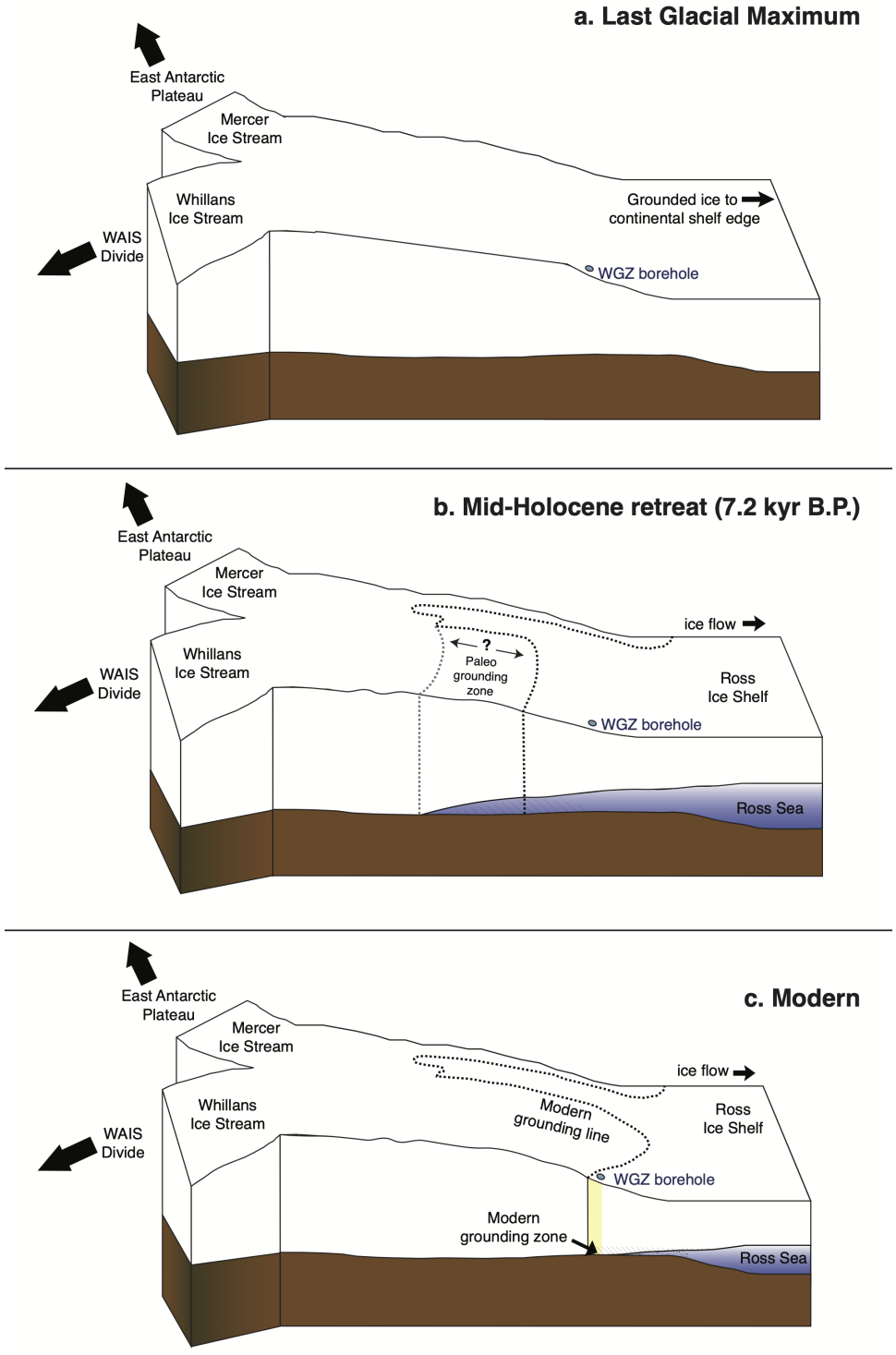

Figure 4.4: Conceptual model illustrating Whillans Ice Stream grounding zone through (a) LGM, (b) mid-Holocene retreat, and (c) re-advance to present position based on RPO ^{14}C ages in this study.

4.6.4 Implications for Deglacial History of Ross Sea

Our record from WGZ provides new insight into the large-scale deglacial history of the Ross Sea. During the LGM, grounded ice filled the Ross Sea (Figure 4.4) to the continental shelf edge (e.g., Mosola & Anderson, 2006; Bentley et al., 2014). Exposure ages indicate that Beardmore and Scott Glaciers, which deliver ice to the central Ross Sea, maintained LGM ice thickness until between 16.7 and 14.4 kyr B.P. (Spector et al., 2017). These terrestrial records are consistent with the marine AIO (Prothro et al., 2020) and foraminiferal (Licht, 2004) constrained ^{14}C ages for timing of initiation of grounding line retreat from the continental shelf edge. As deglaciation persisted in the western Ross Sea, foraminiferal ^{14}C ages indicate open marine conditions east of Ross Island 8.6 kyr B.P. (McKay et al., 2016), consistent with ^{10}Be exposure ages indicating grounding line retreat to the mouths of Beardmore and Shackleton glaciers (Spector et al., 2017). Collectively, these records indicate that full deglaciation of the western Ross Sea precedes grounding line retreat of Whillans Ice Stream by $\sim$1 kyr. Dates from WGZ falls closer to the deglacial history in the western Ross Sea than in the eastern Ross Sea (e.g. Bart, Anderson, & Nitsche, 2017; Bart, Krogmeier, et al., 2017). This interpretation is consistent with the tectonic boundary identified between East and West Antarctica beneath RIS, which has been suggested to control bathymetry and oceanic circulation (Tinto et al., 2019). We thus contend that grounding line retreat at Whillans Ice Stream likely responded to western Ross Sea oceanic conditions, whereas grounding line retreat at other ice streams along the Siple Coast (i.e., Bindschadler ice stream) may have been more strongly influenced by eastern Ross Sea oceanic conditions. The occurrence of retreat at WGZ supports physiographic control of grounding line retreat through embayments (Halberstadt et al., 2016), but widespread transects of sub ice sediment cores dated with RPO ^{14}C or similarly accurate methods are needed to fully constrain the southernmost extent of this process.

4.7 Conclusions

We present the most accurately dated record of sediments collected from the southernmost portion of the marine cavity beneath RIS. Our record reveals the exposure of subglacial sediments underlying Whillans Ice Stream to marine water as recent as 7.2 B.P. Combined with the broader record of Ross Sea deglaciation, our work supports a retreat and re-advance of the grounding line but amends previously modeled timing from the early-Holocene to the mid-Holocene. Our retreat chronology reveals a variable Siple Coast grounding line during a time of much lower amplitude climate variability than during the last glacial period. This work lends insight into the response of dynamically connected ice streams to physiography, bathymetric controls, and distinct far-field forcing. Furthermore, our data demonstrate that RPO ^{14}C dating improves upon the inherent ambiguity of bulk radiocarbon dating in subglacial sediments and can be used to constrain retreat chronology using sub-ice AIOM.

4.8 Acknowledgements

This work was supported by the U.S. National Science Foundation, Section for Antarctic Sciences, Antarctic Integrated System Science program as part of two subglacial access projects: Whillans Ice Stream Subglacial Access Research Drilling (WISSARD; NSF Grants OPP-0839059, OPP-0839142, OPP-0838933, and OPP-0838885) and Subglacial Antarctic Lakes Scientific Access (SALSA; NSF Grants OPP- 1543347, OPP-1543537, and OPP- 1543441). We thank the University of Nebraska, Lincoln, drill team for borehole access that enabled sample collection, the WISSARD Science Team (see wissard.org for a list of members) for their work in the field, Raytheon Polar Services and Antarctic Support Contract (ASC) for logistical support, and the New York Air National Guard and Ken Borek Air for air support in the field. We thank the GMT team for their continued support of the software package; Figure 1 was produced using GMT6/pyGMT (Wessel et al., 2019). This paper benefitted from discussions with C. Schafer, A. Michaud, C. Gustafson, and M. Patterson as well as insightful criticisms and feedback from L. Simkins and one anonymous reviewer.

4.9 Supplemental Material

Extended information about diatom abundances, the University of South Florida-College of Marine Science Ramped PyrOx (RPO) system blank correction (Section 4.9.2, Figure 4.5), details about the reservoir correction applied in this study, and data tables (Tables 4.2, 4.3) containing all data generated in this study that is not found in the main text.

4.9.1 Diatom Abundance

The total number of diatoms observed per slide was few, ranging between 0–7 diatoms per slide. Average diatom abundance numbers are averages for the four slides at each depth. We counted three samples depths (3 cm, 32 cm, 64 cm) and found 600, 800, and 1200 valves/gram, respectively. Commonly observed diatom species (*Denticulopsis simonsenii, Pyxilla reticulata, Stephanopyxis sp.* and *Paralia sulcata*) despite very low abundances, were observed as whole valves and fragments.

4.9.2 Blank Correction

We apply a blank correction of 1.15 ± 0.91 μg and a modern blank of 2.52 ±1.65 μg (Figure 4.5) following the methods outlined in Fernandez, Santos, et al. (2014). We determine the mass of (a) modern and (b) dead contributions of carbon from the Ramped PyrOx ^{14}C system by repeatedly analyzing graphite (n=37) and oxalic acid (n=32), respectively. The blank determinations included here represent operations of the USF RPO system from 2015 to 2019. Past work has noted that a reduction in blank contamination in the RPO system was made when Teflon tubing was replaced with stainless steel and copper tubing (Subt et al., 2017), and we build upon previously reported blank values with the addition of more analyses of our internal standards. Neither modern nor dead blank contamination appear to have any relationship with time, allowing compilation of blank determinations over a longer period of time.

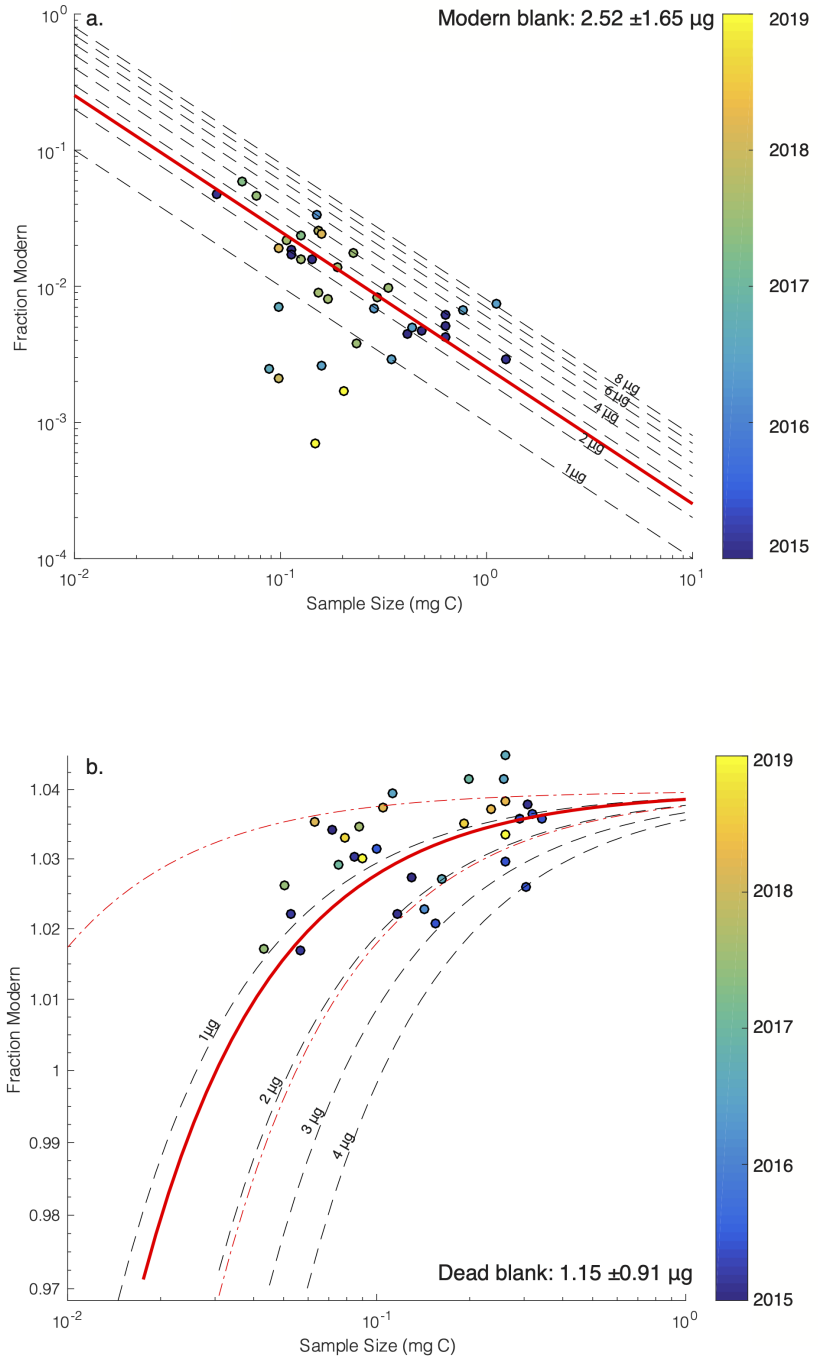

Figure 4.5: The blank determinations plotted here represent operations of the USF RPO system ranging from 2015 to 2019. Modern blank (a) is measured by a graphite standard, while dead blank (b) is measured by an oxalic acid standard. Sample sizes range from 4 to 102 μmol CO_2 (54-1224 μg C) for graphite (a) and 5 to 100 μmol CO_2 (57-1327 μg C) for oxalic acid.

4.9.3 Reservoir Correction

A reservoir age of 1144 ± 120 years is recommended for Holocene aged materials in the Southern Ocean (Hall et al., 2010), and extant amphipods collected from the marine cavity at our study site during borehole operations result in an average ^{14}C age of 1101 ± 38 years (Kingslake et al., 2018). In order to accurately account for local reservoir age in marine cavity beneath RIS, we apply the measured amphipod average as our reservoir correction (1101 years). However, the standard deviation of analytical errors from measured amphipods likely does not sufficiently account for variation in the local reservoir in a sub-ice shelf and grounding line proximal environment due to the input of relict carbon. We thus apply a standard deviation of ± 120 years as recommended by Hall et al. (2010). Our reservoir correction of 1101 ± 120 years to both accurately account for local reservoir age in marine cavity beneath RIS and confidently compare our ages with previous deglacial records in the Ross Sea Embayment.

4.9.4 Supplementary Data Tables

Table 4.3: Calibrated ages from low temperature RPO intervals (RPO-1) using a reservoir correction of 1101 ± 120 and the Marine 20 curve in Calib 8.2 (Heaton et al., 2020). Ages are reported with the median probability, as well as 1σ and 2σ confidence intervals.

Sediment core	**Sample depth (cm)**	**Calibrated age of RPO-1 (yrs B.P.)**	**1σ (yrs B.P)**	**2σ (yrs B.P)**
WGZ1-GC3	5	9856	9528-10164	9231-10542
WGZ1-GC3	13	7186	6990-7406	6747-7573
WGZ1-GC3	40	10046	9436-10641	8838-11267
WGZ1-GC3	62	9460	9139-9746	8898-10113

Table 4.2: Table containing total organic carbon (%TOC) for samples analyzed every 2 cm from WGZ1-GC3. %TOC was determined with a Carlo-Erba NAN2500 Series-II Elemental Analyzer using a small aliquot of decarbonated sediment at the University of South Florida College of Marine Science. Analytical uncertainty, expressed as ±1 standard deviation of replicate measurements of a working standard (low carbon, Antarctic sediments from the core catcher of JGC20C) was ±0.10% during measurement of these samples.

Sample Name	**Sample Depth (cm)**	**Total organic carbon (%)**	**±(1 σ)**
WGZ 3 cm	3	0.05	0.1
WGZ 7 cm	7	0.03	0.1
WGZ 9 cm	9	0.15	0.1
WGZ 11 cm	11	0.05	0.1
WGZ 15 cm	15	0.04	0.1
WGZ 17 cm	17	0.03	0.1
WGZ 21 cm	21	0.03	0.1
WGZ 28 cm	28	0.11	0.1
WGZ 30 cm	30	0.13	0.1
WGZ 32 cm	32	0.12	0.1
WGZ 34 cm	34	0.1	0.1
WGZ 36 cm	36	0.11	0.1
WGZ 38 cm	38	0.1	0.1
WGZ 42 cm	42	0.12	0.1
WGZ 44 cm	44	0.1	0.1
WGZ 46 cm	46	0.12	0.1
WGZ 48 cm	48	0.11	0.1
WGZ 50 cm	50	0.12	0.1
WGZ 52 cm	52	0.12	0.1
WGZ 54 cm	54	0.13	0.1
WGZ 56 cm	56	0.04	0.1
WGZ 60 cm	60	0.14	0.1
WGZ 64 cm	64	0.08	0.1
WGZ 68 cm	68	0.11	0.1

5 The origin, age, and cycling of carbon beneath the West Antarctic Ice Sheet

5.1 Introduction

Movement of water through the subglacial hydrologic system, including subglacial lakes, is important both for the dynamics of the overlying ice and the biogeochemistry of the substrates with which this water interacts (e.g., Stearns et al., 2008; Bell, 2008; Skidmore, 2011; Siegfried et al., 2016; Hawkings et al., 2020). Subglacial lakes are discrete bodies of water that exist between an ice sheet's base and the underlying substrate. Water that fills Antarctic subglacial lakes is sourced exclusively from melting at the base of the overlying ice sheet as a result of pressure and geothermal heating (Beem et al., 2010; Fisher et al., 2015). Since the first recognition of subglacial lakes in Antarctica ("Experiment in visual orientation during nights in the Antarctic", 1960; Robin et al., 1970), airborne radio-echo sounding, radar altimetry, and satellite laser altimetry have been used to identify over 400 subglacial lakes beneath the Antarctic Ice Sheet (Siegert et al., 2016). Many Antarctic subglacial lakes are thought to be isolated bodies of water (e.g., Subglacial Lake Vostok; Kapitsa et al., 1996), whereas others have been classified as "active" (n=139; Siegfried & Fricker, 2018). Active subglacial lakes form an interlinked path that transports water, nutrients, and sediments from Antarctica's interior to the coastal Southern Ocean (Fricker et al., 2007; Carter & Fricker, 2012).

Subglacial water, including gases (Scholander et al., 1956, 1962) and particulate material (Priscu & Christner, 2014) that liberated by ice melt, interacts with underlying sediments to provide nutrients and energy that make the subglacial environment favorable for microbial life (Skidmore, 2011). The potential for discovery of unique lifeforms hidden beneath

the Antarctic Ice Sheet prompted the development of clean-access technologies to directly investigate these features while preserving their pristine nature (Priscu et al., 2013; Michaud et al., 2020). Clean-access drilling enabled the first direct sampling and unequivocal observation of bacteria and archaea that form a functional microbial ecosystem beneath the West Antarctic Ice Sheet (WAIS) as part of the Whillans Ice Stream Subglacial Access Drilling (WISSARD) Project (Achberger et al., 2016; Christner et al., 2014; Michaud et al., 2017; Mikucki et al., 2016; Vick-Majors et al., 2016). In addition to microbial life, results from WISSARD indicate that interactions between subglacial water, microbes, and sediment enable the accumulation of dissolved organic carbon that exceeds biological demand within Whillans Subglacial Lake (SLW; Vick-Majors et al., 2020).

The sediments deposited underneath subglacial lakes have been of interest to the paleoclimate community since the discovery of the lakes themselves because of their potential to chronicle the long-term evolution of the overlying ice sheet (Siegert et al., 2005; Bentley et al., 2011). The first sediment cores collected from an Antarctic subglacial lake (Hodson et al., 2016) along with other sub-ice-stream sediment cores collected along the Siple Coast (Engelhardt et al., 1990; Kamb, 2001) contain evidence for marine influence on the subglacial environment over a variety of timescales (Michaud et al., 2016; Kingslake et al., 2018; Coenen et al., 2019; Venturelli et al., 2020). Understanding the timescales over which the subglacial environment received marine input in the geologic past is important both for gaining a long-term perspective of ice sheet dynamics and constraining how long subglacial lakes have been isolated.

Subglacial sedimentary archives underlying WAIS contain evidence for marine conditions over West Antarctica during the geologic past. Bedrock underlying WAIS exists primarily below sea-level, therefore during times when WAIS was smaller or non-existent, an interior seaway provided a viable habitat for seasonal phytoplankton productivity. Age-diagnostic marine microfossils accumulated in the deep, West Antarctic sedimentary basins during these periods of marine conditions and became encapsulated in the subglacial sedi-

mentary record when ice re-advanced (Paxman et al., 2019; Wilson et al., 2012). Diatoms from subglacial sediments along the Siple Coast have been used to infer open marine conditions over West Antarctica during the Oligocene, Miocene, Pliocene, and even Pleistocene (Harwood et al., 1989; Scherer, 1991; Scherer et al., 1998).

Juxtaposed with evidence for ice sheet absence in subglacial sedimentary archives is evidence of marine input to the subglacial environment under the cover of an ice shelf (Kingslake et al., 2018; Venturelli et al., 2020). Michaud et al. (2016) used chloride profiles in SLW sediment cores as evidence for marine influence on subglacial sediments within the recent geologic past, but could not constrain the precise timing of incursion. An ice sheet model (Kingslake et al., 2018) and radiocarbon measurements from these sediments (Venturelli et al., 2020) demonstrated that subglacial sedimentary deposits along the Siple Coast became bathed in marine waters when the grounding line retreated inland over West Antarctica from its present position during the Holocene. The process of grounding line retreat without ice shelf or WAIS collapse provides geochemical evidence for the presence of marine solutes, but does not result in microfossil deposition due to the persistence of the overlying ice shelf that would have rendered this environment uninhabitable for photosynthetic phytoplankton.

In this chapter, we demonstrate that sediments collected 150 km from the modern marine environment from Mercer Subglacial Lake (SLM) can be used to chronicle Holocene grounding line retreat far inland its modern position. To investigate how new, marine carbon is translocated to SLM sediments, we characterize acid insoluble organic material (AIOM) and inorganic carbon (detrital carbonate) from SLM sediment as well as dissolved organic carbon (DOC), dissolved inorganic carbon (DIC) and particulate organic carbon (POC) using $\delta^{13}C$ and $\Delta^{14}C$. With this work we aim to provide new constraints on ice sheet history and the subglacial carbon cycle, which are ultimately important for biological interpretations of microbial communities existing within subglacial lakes in this region.

5.2 Methods

5.2.1 Site Description

This work involves samples collected from Mercer Subglacial Lake (SLM) as part of the Subglacial Antarctic Lakes Scientific Access (SALSA) project. SLM is an active subglacial lake located at the confluence of Mercer Ice Stream (MIS) and Whillans Ice Stream (WIS) along the Siple Coast of West Antarctica (Figure 5.1). Ice that flows over SLM, as well as water that flows through SLM, are supplied in part from West Antarctica (WIS, MIS) and in part from East Antarctica (as Reedy Glacier flows into MIS). Therefore, water, solutes, and sediments transported from upstream may reflect both East and West Antarctic influences. Throughout the lifetimes of the Ice Cloud and land Elevation satellites (ICESat: 2003-2010 and ICESat-2: 2018-present), SLM has been observed through two complete fill-drain cycles and a third filling period (Siegfried & Fricker, 2018, in revision). When the SALSA science team accessed SLM during the 2018-2019 Antarctic field season, the lake had just entered a third draining phase (Figure 5.1)

5.2.2 Sample Collection

During the 2018-2019 Antarctic field season, the SALSA science team employed a clean access, hot-water drill (Priscu et al., 2013; Tulaczyk et al., 2014; Rack, 2016) to melt a 0.4 m diameter borehole through 1087 m of MIS to access SLM (84.64025°S, 149.50321°W; Figure 5.1). We determined that the SLM water column was 15 m deep during sampling, and over the 10 days of scientific operations we collected 60 L of lake water from the middle of the water column (7.5 m above sediment–water interface; Priscu et al., in revision). We employed a Uwitec multicoring device to retrieve ten multicores (0.32 to 0.49 m), and a newly developed borehole gravity coring device to retrieve two free fall (gravity) cores (1.0 and 1.76 m; Priscu et al., in revision). We followed a strict ^{14}C-clean protocol (Chapter 2) to separate discrete aliquots of lake water for isotopic analysis. SLM water collected for isotopic analysis of DOC

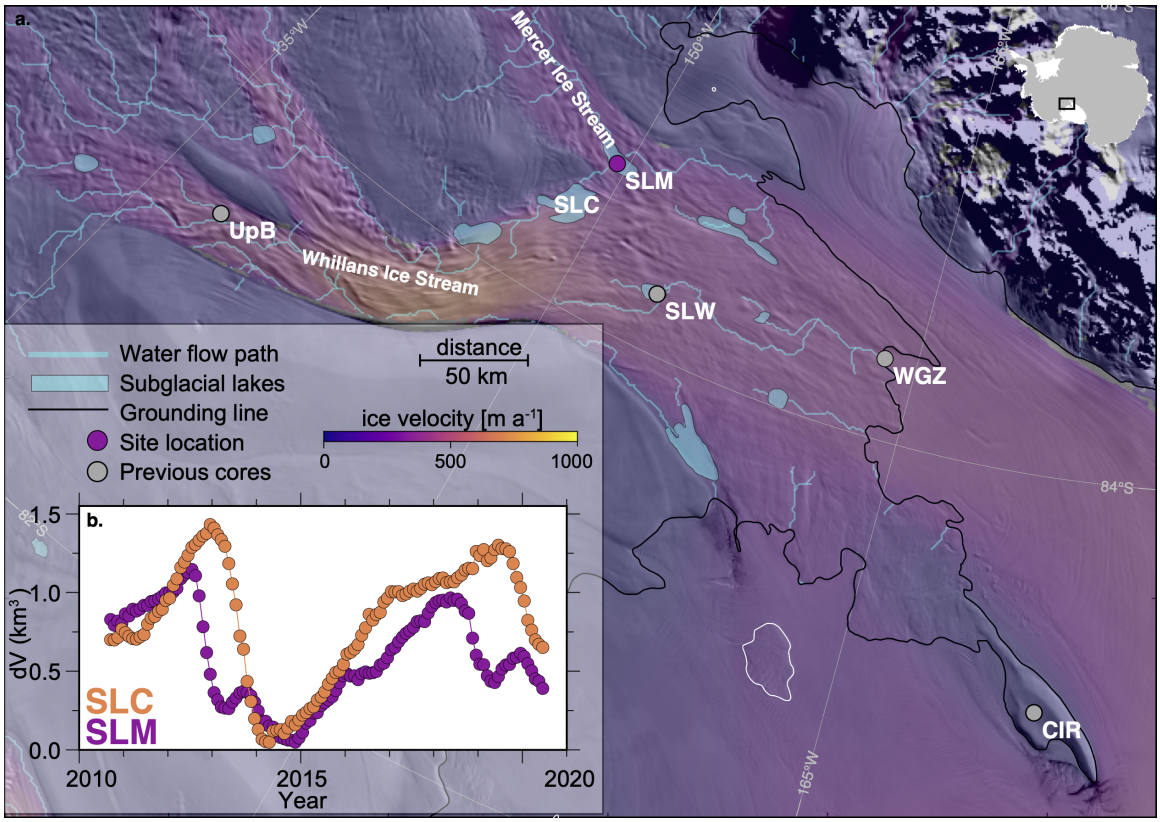

Figure 5.1: Map of study location. (a) Ross Sector ice streams with previous subglacial core site locations at Whillans Ice Stream (UpB), Whillans Subglacial Lake (SLW), Whillans Grounding Zone (WGZ) and Crary Ice Rise (CIR) marked with gray circles and the site from this study, Mercer Subglacial Lake (SLM), marked with a purple circle. Ice velocity (Mouginot et al., 2019) overlain on an imagery mosaic (Scambos et al., 2007)), with active subglacial lake areas (blue polygons; Siegfried & Fricker, 2018), hydropotential flow paths (blue lines; Siegfried & Fricker, 2018), and grounding line (black; Depoorter et al., 2013) indicated. (b) Volume changes in Conway Subglacial Lake (SLC) and SLM inferred from CryoSat-2 radar altimetry (Siegfried & Fricker, in revision).

was decanted from a clean Niskin bottle into a pre-combusted (525°C; 4 hrs) 1 L amber glass bottle and immediately frozen. SLM water collected for isotopic analysis of DIC was decanted into pre-combusted (525°C; 4 hrs) and poisoned (20 μL of a saturated $HgCl_2$ solution dried in each empty bottle prior to sample addition) 500 mL glass bottles. Water samples were shipped directly to the National Ocean Sciences Accelerator Mass Spectrometry (NOSAMS) facility. Sediment cores were capped immediately upon recovery from the borehole. We allowed cores to settle for 24 hours to allow for gas escape before securing caps with tape for shipment. All cores were stored upright during this time. Two multicores (01UW-A and 01UW-C) and two gravity cores (01FF and 02FF) intended for isotopic analyses were wrapped with multiple layers of plastic wrapping for shipment to the Oregon State University Marine and Geology Repository (OSU-MGR).

5.2.3 Isotopic Analyses of Water Samples

At NOSAMS, we filtered (Pall Life Sciences, 2.5cm diameter, PALL number 7200) 1 L of subglacial lake water prior to preparation for isotopic analyses ($\delta^{13}C$ and $\Delta^{14}C$) of DOC. we acidified (1N HCl), rinsed (Deionized water), and dried the filtered residue to isotopically characterize POC in the SLM water column. Once dry, we packed the entire filter into a pre-combusted (900°, 4 hrs) quartz ampoule with copper oxide and silver wire, combusted the closed ampoule (900°, 4 hrs), and cryogenically purified the CO_2 evolved from POC. To prepare the filtered 1 L water sample for isotopic analyses of DOC, we followed the methods of Beaupré et al. (2007) and Griffin et al. (2010). To remove DIC, we acidified the sample with 1 mL of 85% phosphoric acid. Following acidification, we purged the sample with ultrahigh purity helium gas, and oxidized the sample with ultraviolet light for four hours in a quartz reactor. CO_2 evolved from this process was stripped with ultrahigh purity helium, cryogenically purified, and flame sealed in a borosilicate ampoule.

To prepare samples for isotopic analyses of DIC, we followed the methods described in McNichol et al. (2010). Briefly, we transferred water samples from storage bottles to

preparatory bottles in an N_2-filled glove bag. we assembled each DIC stripping apparatus (probe and bottle) within the glove bag before transferring each sample to the vacuum line. we acidified (4 mL of 85% phosphoric acid) each sample to lower the pH enough to liberate DIC from water for 10 minutes. Following this process, we evacuated inert gases from the vacuum line and cryogenically dried and purified evolved CO_2 and placed each sample in a transfer flask.

All samples of CO_2 evolved from POC, DOC, and DIC sample preparations were converted to graphite by reduction on an iron catalyst using the closed-tube, zinc catalyst method (Walker & Xu, 2019; Xu et al., 2007) before determination of $^{14}C/^{12}C$ ratios and $\delta^{13}C$ at NOSAMS.

5.2.4 Non-destructive Sediment Core Analyses

Prior to sampling sediment cores at OSU-MGR, the SALSA science team obtained computed tomography (CT) scans to generate high-resolution images of SLM sediment cores. After CT scanning, we split each core to perform non-destructive analyses, core photography, and visual core description. We scanned each core using a Geotek standard multi-sensor core logger (MSCL) multi sensor track (MST) to characterize bulk density and magnetic susceptibility and an ITRAX x-ray fluorescence (XRF) scanner to characterize major bulk element composition. We used photographs, CT scans, and visual description to characterize lithologic units for all cores. Similarities in core lithology, magnetic susceptibility data, and major bulk element composition, along with the close proximity of coring locations enabled the construction of a composite section. To generate a composite section, we used the Corewall Corelyzer software (https://csdco.umn.edu/resources/software/correlator) developed and maintained by the Continental Scientific Drilling Coordination Office. With this program, we correlated magnetic susceptibility and major bulk element composition records of multicores 01UW-A and 01UW-C and free fall cores 01FF and 02FF.

5.2.5 Destructive Sediment Core Analyses

We removed 1-3 g (wet weight) samples for analysis with EA-IRMS, and 5-10 g (wet weight) samples for Ramped PyrOx ^{14}C (Table 5.1). We dried, homogenized, and acid rinsed each sample with 1N hydrochloric (HCl) acid to remove carbonate minerals. Following decarbonation, we removed remaining acid with a series of rinses with deionized water until the supernatant asymptotically approached a pH near neutrality (pH=6–7). Remaining acid insoluble organic material (AIOM) was dried and stored in pre-combusted (525°C; 4 hrs) glass scintillation vials until analysis. During the first round of decarbonation of these samples, we noticed an amount of effervescence conducive to isotope analysis and reserved a subset of samples (n=6) to remain untreated for analysis of the carbonate mineral component.

Table 5.1: Sample intervals for each SLM sediment core used for geochemical analysis.

Core name	**Core type**	**Core length**	**EA-IRMS sample interval**	**RPO ^{14}C sample interval**
01UW-A	Multicore	49 cm	Top and bottom of each lithologic unit	4-6 cm, 7.5-11 cm, 16-18 cm
01UW-C	Multicore	44 cm	Every 2 cm	None
01FF	Gravity core	100 cm	Every 4 cm	5-7 cm, 45-50 cm, 57-58 cm, 65-66 cm, 73-74 cm, 80-85 cm
02FF	Gravity core	176 cm	Top and bottom of each lithologic unit	148-150 cm, 168-170 cm

We determined total organic carbon (% TOC) and bulk stable isotope composition (δ^{13}C) for all AIOM samples with a Carlo-Erba NAN2500 Series-II Elemental Analyzer

coupled to a continuous-flow Thermo-Finnigan Delta + XL isotope ratio mass spectrometer (IRMS). We used NIST 8573 and NIST 8574 as calibration standards and a low carbon, bulk Antarctic sediment sample (JGC20C) as a working standard. Analytical uncertainty, expressed as ±1 standard deviation of replicate measurements of the working standard, was ± 0.02% for %TOC and 0.5‰ for δ^{13}C during the period over which we analyzed these samples. To analyze the carbonate mineral component, we hydrolyzed the subset (n=6) of sediment samples that had not been decarbonated with 85% phosphoric acid (H_3PO_4) under vacuum at NOSAMS. All CO_2 evolved from hydrolysis of carbonate minerals was cryogenically purified and flame sealed into a pre-combusted (525°C; 4 hrs) borosilicate ampoules.

Sediments retrieved from the subglacial environment include a mixture of material transported from upstream and deformed and deposited by the overlying ice sheet (Kamb, 2001). We applied RPO ^{14}C dating (Rosenheim et al., 2008) in attempt to separate the small amount of ^{14}C bearing organic carbon from the abundance of pre-aged organic carbon in AIOM samples from this subglacial mixture. Using RPO, we separated pyrolysates into three discrete CO_2 aliquots for each sediment depth. Even with a large sample size (400 mg dry sediment), individual aliquots across RPO spectra contained only 55-450 μg C, requiring treatment as "small samples" by NOSAMS. We based sampling on the shape of thermographs (CO_2 evolved with temperature in the RPO process; Figure 5.2), sampling the first aliquot of CO_2 at the top of the first peak on each thermograph (400°C), the second at the completion of the first peak (700°C), and the third at the completion of the pyrolysis reaction (1000°C) following the methods of Rosenheim et al. (2008).

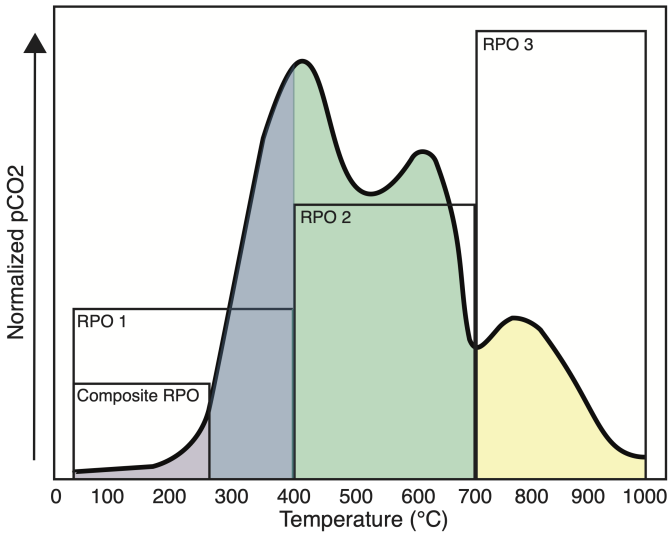

Figure 5.2: Averaged thermographs for SLM RPO analyses (n=12) demonstrating thermograph shape and temperatures at which evolved CO_2 aliquots were separated. "Composite RPO" is used to indicate the temperature at which ultra-small RPO aliquots were sampled.

Subt et al. (2017) demonstrated that minimizing the size of low temperature RPO aliquots can limit the bias of pre-aged allochthonous carbon in Antarctic margin sediments. To approach a minimum age of radiocarbon present in SLM sediments, we applied a modified RPO method, wherein we repeatedly combusted several (n=4) sediment aliquots (400 mg each) from a sampled interval to collect ultra-small, low-temperature aliquots (collected at 270°C; Figure 5.2). These low temperature CO_2 aliquots were combined for isotopic analysis as a single sample following the composite technique described in Subt et al. (2017). All aliquots of CO_2 produced with the preparatory techniques described above (RPO and carbonate hydrolysis) were sent to NOSAMS for determination of $^{14}C/^{12}C$ ratios and $\delta^{13}C$.

To account for blank contamination associated with the preparation of sediments for ^{14}C dating with RPO, we apply a correction of 1.15±0.91 μg to account for the mass of ^{14}C-free (dead blank) contamination and a correction of 2.52 ±1.65 μg to account for the mass of ^{14}C-bearing (modern) contamination following the methods of Fernandez, Santos, et al. (2014). Blank determinations applied here reflect an updated quantification of blank in the USF RPO system from 2015-2020, described in detail in Venturelli et al. (2020).

Hemingway, Galy, et al. (2017) demonstrated that a small amount of fractionation occurs due to incomplete oxidation of reduced gases to CO_2 during RPO preparation. Because δ^{13}C spectra from samples prepared with RPO can be a useful source tracer of end-member inputs to a system, it is necessary to remove the effect of preparation on δ^{13}C values to accurately interpret the data. As such, we follow the recommendations of Hemingway, Galy, et al. (2017) to correct for fractionation on RPO derived δ^{13}C:

$$\delta^{13}\mathrm{C}_{\mathrm{corrected}} = \delta^{13}\mathrm{C}_{\mathrm{RPO}}(\delta^{13}\mathrm{C}_{\mathrm{bulk}} - \overline{\delta^{13}C_s}) \tag{5.1}$$

Where $\delta^{13}C_{RPO}$ is the reported δ^{13}C for an RPO aliquot reported by NOSAMS, $\delta^{13}C_{bulk}$ is the reported δ^{13}C analyzed for a whole sample at USF-CMS, and $\delta^{13}C_s$ is the mass-weighted mean value calculated from the full spectra of RPO δ^{13}C results reported by NOSAMS.

5.2.6 ^{14}C Calculations

We present ^{14}C data using conventions defined by Stuiver and Polach (1977), however, the equations therein were originally defined for the measurement of ^{14}C activity with decay counting techniques which have since been replaced with accelerator mass spectrometry (AMS). Therefore, the equations used in this chapter are presented to reflect language more consistent with the methodological advancement to AMS and to align with recommendations of NOSAMS. ^{14}C data are reported by NOSAMS as fraction modern (f_M), which is the deviation a sample's $^{14}C/^{12}C$ ratio from the absolute international standard defined at 95% of the $^{14}C/^{12}C$ ratio of the original Oxalic Acid standard (Ox-1) in the year 1950. This is mathematically defined as:

$$f_M = \frac{\mathrm{R}^{\frac{14}{12}}{}_{\mathrm{SN}}}{\mathrm{R}^{\frac{14}{12}}{}_{\mathrm{ON}}} \tag{5.2}$$

The subscript SN represents the sample $R^{\frac{14}{12}}$ has been normalized to a common δ^{13}Cvalue of -25‰ to remove the influence of isotopic fractionation on reported $^{14}C/^{12}C$ ratios. Similarly,

the subscript ON represents that the Ox-1 standard $R^{\frac{14}{12}}$ has been normalized to a common δ^{13}C value of -19‰. We convert f_M to ^{14}C content and ^{14}C age following the convention outlined in Stuiver and Polach (1977).

5.2.7 ^{14}C Content

When discussing the presence of ^{14}C in various SLM carbon pools, we present results in Δ^{14}C notation. This value, originally described as δ^{14}C (Stuiver & Polach, 1977)

$$\delta^{14}\mathrm{C} = (f_M - 1) \times 1000 \tag{5.3}$$

is the relative difference between the absolute international standard (base year 1950) and the sample's ^{14}C/^{12}C ratio corrected for δ^{13}C . Δ^{14}C may be calculated as follows:

$$\Delta^{14}\mathrm{C} = (f_M \mathrm{e}^{-\lambda(\mathrm{y}-1950)} - 1) \times 1000 \tag{5.4}$$

where λ represents the ^{14}C decay constant ($\frac{1}{8267}$, equivalent to the true half-life of 5730 years) and y represents the year in which measurement of ^{14}C/^{12}C ratio was made. The exponential term, in the case of the analyses herein is then:

$$\mathrm{e}^{-\lambda(\mathrm{y}-1950)} = \mathrm{e}^{\frac{-1}{8267}(2019-1950)} = 0.9917 \tag{5.5}$$

To simplify my calculation of Δ^{14}C , we drop the exponential term as a value nearly equal to one (0.9917) yields results indistinguishable from the following equation within analytical uncertainty:

$$\Delta^{14}\mathrm{C} = (f_M - 1) \times 1000 \tag{5.6}$$

As a result, the final form of the calculation for Δ^{14}C matches the δ^{14}C equation (5.3) originally defined by Stuiver and Polach (1977).

5.2.8 Age

To assess the timing over which marine carbon is introduced to the subglacial system, conversion of ^{14}C data to "age" (year date) is necessary. A sample's $f_M$can be used to calculate its radiocarbon age as follows:

$$\text{Age}(^{14}\text{C yr}) = -8033 \ln(f_M) \tag{5.7}$$

Here, age is calculated conventionally with the Libby half-life of 5568 ($\lambda = \frac{1}{8033}$ yr^{-1}). Finally, we convert the radiocarbon age (^{14}C yr) to calendar age (yr B.P.) using the Marine20 curve in Calib 8.2 and a local reservoir correction of 1,101±120 years following Venturelli et al. (2020).

5.3 Results

5.3.1 Sediment Description

Multicores 01UW-A and 01UW-C consist of two lithologic units, with 12 to 15 cm of laminated mud (Unit I) underlain by a massive clast-rich muddy diamict unit (Unit II; Figure 5.3). Gravity cores 01FF and 02FF contain unit II underlain by 5 cm layer of clast-free mud with no visible structure (Unit III). Cores 01FF and 02FF contain a final clast-rich muddy diamict unit (Unit IV). Similarities in magnetic susceptibility and lithology (Figure 5.3) allowed for the construction of a continuous 2.06 m composite section representing the transition from sub-ice stream deposition to lake deposition within SLM. Bulk sedimentary AIOM was characterized by very low %TOC that decreased downcore from 0.36% in unit I to 0.15% throughout the remaining units (Figure 5.3).

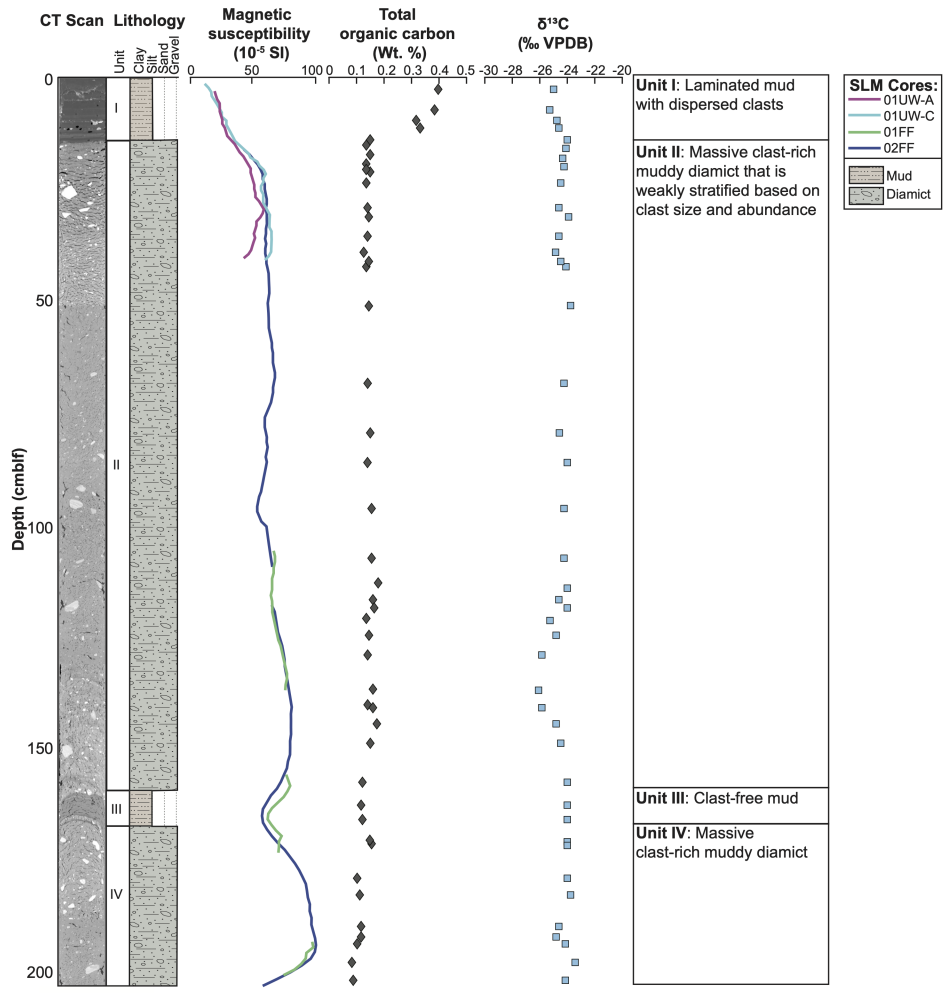

Figure 5.3: CT Scans, lithology, magnetic susceptibility %TOC, and δ^{13}C along with sedimentary unit descriptions for the composite section constructed from sediment cores 01UW-A, 01UW-C, 01FF, and 02FF collected from SLM. Here, it is apparent that Unit I contains a significantly higher %TOC than the rest of the sediments collected from SLM.

5.3.2 Carbon Reservoirs

To assess the subglacial carbon cycle through the lens of an active subglacial lake, we determined the size of carbon reservoirs (DIC and DOC; Table 5.2) within the water column during the fullest stage of SLM as well as carbon reservoirs in the underlying sediment (organic carbon and carbonate minerals; Table 5.2). When full, the area-averaged height anomaly observed with ICESat indicates that that average depth across SLM is 5 m (Siegfried & Fricker,

2018). The area of SLM, as defined by the original lake outline (Fricker & Scambos, 2009), corrected for projection on the WGS ellipsoid, is 143 km^2. Thus, when full, SLM contains 7.15×10^{11} L water. We determined the size of carbon reservoirs in sediments underlying SLM over a depth of 15 cm to assess carbon present in sediments deposited within SLM and over 206 cm to assess carbon present throughout the full sediment column collected in SALSA coring efforts.

Table 5.2: Calculated masses for SLM carbon reservoirs. We present quantification of both Unit I and the full recovered section for comparison between processes within SLM and more generally the subglacial environment.

Carbon reservoir	**Size (g C)**
Water column DOC	4.38×10^8
Water column DIC	7.69×10^9
Sediment OC in Unit I	1.40×10^{11}
Sediment OC in 2 m	8.44×10^{11}

5.3.3 Isotopic Results for Inorganic Carbon

Measurements of DIC from the SLM water column (n=5) resulted in an average concentration of 0.89 (± 0.06) mmol/kg, a $\Delta^{14}C$ of -979.2‰ (± 2.8‰), and a $\delta^{13}C$ of -8.86‰ (±0.13‰;Figure 5.4). We found a low abundance of carbonate minerals in SLM sediment samples (n=6) ranging from 0.75% to 1.25% (weight percent). Similar to water column DIC samples, the carbonate portion of SLM sediment resulted in low $\Delta^{14}C$ values ranging from -992.7‰ to -986.1‰ with $\delta^{13}C$ values that range from -3.73‰ to -2.81‰ (Figure 5.4). No downcore trends exist in either $\Delta^{14}C$ or $\delta^{13}C$ of the carbonates (Figure 5.4).

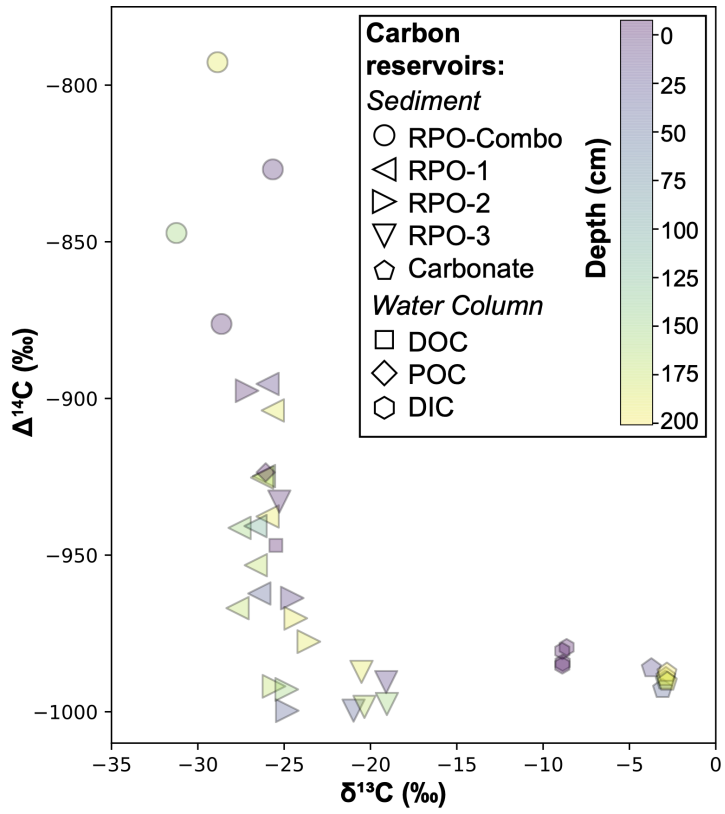

Figure 5.4: Distribution of isotopic data for all carbon reservoirs measured in SLM. Here we demonstrate the spectrum of isotopic data in sediment samples prepared with RPO and distinct differences in Δ^{14}C and δ^{13}C values between inorganic and organic carbon reservoirs. All points are colored based on the depth from which they were collected in SLM where 0 represents the sediment-lake water interface.

5.3.4 Isotopic Results for Organic Carbon

Organic carbon reservoirs are characterized by a higher ^{14}C content than inorganic carbon reservoirs, with Δ^{14}C values that increase from DOC in the water column to AIOM in the sediment. Our protocol for maintaining ^{14}C cleanliness limited sample collection to one liter of water for accurate characterization of DOC and filtration of POC (Venturelli et al., *submitted*; Chapter 3). In absence of replicates, uncertainty is presented as the 2σ analytical error for both of these samples. Measurements of DOC from the SLM water column resulted in a concentration of 51 μmol/kg, a Δ^{14}C of -946.9‰ (±2.6‰), and a δ^{13}C of -25.48‰ (±0.10‰ ;Figure 5.4).

Measurements of POC from the water column resulted in a $\Delta^{14}C$ of -923.6‰ (±1.7‰) and a $\delta^{13}C$ of -26.07‰ (±0.10‰ ; Figure 5.4). All AIOM samples prepared with RPO resulted in a spectrum of isotopic data, lacking a plateau (multiple aliquots from the same sample being characterized by the same $\delta^{13}C$ or $\Delta^{14}C$ value). Individual spectra were characterized by a more depleted $\delta^{13}C$ value in the lowest temperature aliquot increasing to a more enriched value in the highest temperature aliquot, ranging from -31.2‰ to -19.1‰ across all samples prepared with RPO. Concentrations of ^{14}C decreased across spectra, with a maximum $\Delta^{14}C$ value of -792.7‰ in a composite low-temperature aliquot and a minimum of -1000‰ in several high temperature RPO aliquots (Figure 5.4).

5.4 Discussion

5.4.1 The SLM System

Antarctic subglacial lakes are filled by basal melt from the overlying ice sheet. Contemporarily, basal melt supplying water to SLM comes in part from East Antarctica and in part from the drainage of Conway Subglacial Lake (SLC) underlying WAIS immediately upstream (Carter & Fricker, 2012; Carter et al., 2013). The best constraint on the age of this basal melt source comes from the nearby WAIS divide ice core, which contains ice formed 68 kyr B.P. at its base (Buizert et al., 2015). While this old, basally sourced water fills SLM (and other subglacial lakes in the area) during a fill cycle, it accumulates biologically relevant solutes (Vick-Majors et al., 2020). As SLM drains, both water and accumulated solutes flow through other lakes underlying MIS, and ultimately across the grounding line to the sub-Ross Ice Shelf marine environment (Carter & Fricker, 2012; Siegfried et al., 2016; Siegfried & Fricker, 2018).

5.4.2 Carbon in the SLM Water Column

Dissolved inorganic carbon: In most aquatic environments (subaerial lakes, rivers, oceans), exchange at the air-water interface can supply CO_2 to the system. In Antarctic subglacial

lakes, this process is replaced by exchange with ancient atmospheres when CO_2 trapped in old ice is liberated from the ice matrix by basal melting (Scholander et al., 1956, 1962) or interactions with underlying geology. Inorganic carbon in SLM may supplied by basal melt and dissolution of carbonate-bearing rocks in the Transantarctic Mountains. Additionally, remineralization of organic matter may provide an additional, albeit small, source of CO_2:

$$(CH_2O)_x(NH_3)_y(H_3PO_4)_z + (x + 2\,y)O_2 \longrightarrow xCO_2 + (x + y)H_2O + yHNO_3 + zH_3PO_4 \quad (5.8)$$

The DIC collected from SLM during the SALSA field season thus reflects input (by mass) both from the flow of water into the lake, and production within the lake during the fill period:

$$DIC_{measured} = DIC_{input} + DIC_{produced} \quad (5.9)$$

Where DIC_{input} reflects inorganic carbon dissolved in meltwater over or upstream SLM and inflow into SLM and $DIC_{produced}$ reflects the amount of organic carbon remineralized during the five-year period that SLM was accumulating water before the SALSA team obtained samples.

Dissolved organic carbon: Similar to DIC, sources of DOC to SLM come from both input (basal melt and inflow from upstream) and production within the lake. In Whillans Subglacial Lake (SLW), Michaud et al. (2016) demonstrate an upward diffusion of porewater through sediments underlying SLW that may provide a significant source of DOC to subglacial lake waters. Vick-Majors et al. (2020) demonstrated that the flux of DOC from porewater in SLW could account for a source of 107 g C/year of DOC to subglacial lake water (Vick-Majors et al., 2020). Additionally, Vick-Majors et al. (2020) demonstrate that a significant amount (106 g C/year) of DOC is produced within SLW by chemoautotrophy. If we assume that similar processes are at work in SLM, the DOC collected from SLM during

the SALSA field season thus reflects the following inputs by mass:

$$\mathrm{DOC_{measured}}=\mathrm{DOC_{input}}+\mathrm{DOC_{porewater}}+\mathrm{DOC_{produced}} \tag{5.10}$$

Particulate organic carbon: The operational definition of POC includes all carbon, excluding carbonate minerals, that can be collected on a filter, which includes suspended and sinking biomass and detritus (Kharbush et al., 2020). Whereas most aquatic environments (subaerial lakes, rivers, oceans) include phytoplankton biomass in this definition, the biomass in Antarctic subglacial lakes is made up of bacteria and archaea (Christner et al., 2014; Achberger et al., 2016). The POC sample collected from SLM during the SALSA field season reflects several inputs that can be broken into two categories by mass:

$$\mathrm{POC_{measured}}=\mathrm{POC_{detritus}}+\mathrm{POC_{biomass}} \tag{5.11}$$

where $\mathrm{POC_{detritus}}$ accounts for non-living suspended organic carbon transported by water flowing into SLM and liberated from debris-laden basal ice, while $\mathrm{POC_{biomass}}$ accounts for bacteria and archea living in SLM.

5.4.3 Carbon in SLM Sediments

Geophysical surveys over West Antarctica indicate ∼1 km thick sediment deposits fill subglacial basins underlying the Siple Coast ice streams (Rooney et al., 1987, 1991; Blankenship et al., 1986, 1987; Peters et al., 2006; Bindschadler et al., 1996). Previous investigation of ∼1 m long cores of till underlying these ice streams and RIS established the ages (Oligocene, Miocene, Pliocene, and potentially Pleistocene) of sediment inputs here using marine microfossils (Harwood et al., 1989; Scherer, 1991; Scherer et al., 1998; Coenen et al., 2019), biomarkers (Coenen et al., 2019), carbon isotope (δ^{13}C) analyses (Sackett, 1986), and terrestrial material (Tulaczyk et al., 1998; Kamb, 2001). Because SLM sediments contain a mixture of these same materials, as well as ^{14}C-bearing organic carbon, the AIOM measured

herein likely reflects several inputs that can be broken into two categories by mass:

$$\mathrm{AIOM_{measured}} = \mathrm{AIOM_{pre-aged}} + \mathrm{AIOM_{recent}} \tag{5.12}$$

where $\mathrm{AIOM_{pre-aged}}$ includes any input of organic carbon to subglacial sediment that is older 55,000 years old (devoid of ^{14}C), and $\mathrm{AIOM_{recent}}$ includes any input of organic carbon younger than 55,000 years old (containing ^{14}C).

$\mathrm{AIOM_{pre-aged}}$–the Supply of Pre-aged Carbon to SLM Sediments: The identification of siliceous microfossils in SLM sediments (marine diatoms, silicoflagellates, ebridians, sponge spicules, radiolarians, and chrysophycean cysts) that comprise a mixture of ages (early Oligocene, mid Miocene, late Miocene/Pliocene; Harwood and Leventer, *personal communication*) are consistent with previous findings of Oligocene, Miocene, Pliocene marine components of sediments in this region (Harwood et al., 1989; Scherer, 1991; Coenen et al., 2019). In addition to microfossil evidence for deciphering sources of $\mathrm{AIOM_{pre-aged}}$, we interpret the differences in δ^{13}C values to reflect the range in ^{14}C-free organic carbon in SLM sediments. High temperature RPO aliquots revealed that the ^{14}C-free endmember (Δ^{14}C=-1000‰) is characterized by a range of δ^{13}C values (expressed as a horizontal line; Figure 5.4). Whereas the most isotopically enriched cluster of data (δ^{13}C=-20‰) likely represents a petrogenic carbon reservoir (likely graphite or kerogen) previously described in sediments beneath RIS (Sackett, 1986), the isotopically depleted cluster of data (δ^{13}C=-25‰) likely reflects the same input of pre-aged marine carbon observed with micropaleontologic techniques. This interpretation is consistent with δ^{13}C values measured from phytoplankton bloom related POC in the contemporary Ross Sea (-28‰ to -25‰; Villinski et al., 2000).

$\mathrm{AIOM_{recent}}$–the Supply of ^{14}C to SLM Sediments: The lack of an upstream or basal source of ^{14}C to SLM leaves only a downstream (marine) source of ^{14}C to the system. In order

for marine waters to reach SLM, however, the grounding line, which serves as the boundary between subglacial and marine environments, had to retreat inland of our site sometime in the geologic past. Previous work has established that the introduction of ^{14}C to the subglacial environment along the Siple Coast occurred beneath RIS when the grounding line retreated far inland from its modern position during the Holocene (Kingslake et al., 2018; Venturelli et al., 2020). In absence of any recent (late Pleistocene to Holocene) marine microfossils in SLM sediments, it does not appear that ^{14}C would have come from a particulate source that may have been advected to a grounding-line proximal, sub-RIS environment from an open marine environment (Venturelli et al., 2020). However, chemolithoautotrophic bacteria have been demonstrated to assimilate marine DIC beneath the modern RIS to produce new particulate organic carbon that becomes a part of the sedimentary archive (Horrigan, 1981; Priscu et al., 1990).

The highest measured $\Delta^{14}C$ in SLM sediments (-791‰) is associated with the most depleted $\delta^{13}C$ values (-31.2‰ to -28.1‰). Assuming that the primary mechanism for bacterial DIC assimilation was Calvin-Benson cycling, a Ross Sea source of DIC (2‰; Villinski et al., 2000) would be fractionated by -12 to -26‰during assimilation (House, 1999; House et al., 2003). Further fractionation resulting from bacterial lipid production of -3 to -12‰ (Monson & Hayes, 1982; Jahnke et al., 1999; Teece et al., 1999; Zhang et al., 2003) would produce organic matter with a $\delta^{13}C$value of -13 to -36‰. This mechanism is supported by the discovery of bacterial communities in SLM sediment that primarily employ the Calvin-Benson cycle for carbon assimilation. Bacterially produced organic matter could have become part of the sedimentary archive that is preserved once the grounding line re-advanced a position 150 km downstream SLM observed today.

5.4.4 Using ^{14}C in $AIOM_{recent}$ to Understand Ice Sheet History

The spectra of isotope data from SLM illustrate that AIOM in the subglacial environment can be used to separate the small amount of autochthonous carbon ($AIOM_{recent}$) from pre-

aged carbon ($AIOM_{pre-aged}$) in the highly mixed subglacial sediment reservoir. A linear relationship between $\delta^{13}C$ and $\Delta^{14}C$ appears to exist for SLM organic carbon (Figure 5.4) that extends from previously bulk-analyzed subglacial sediments (Kingslake et al., 2018; Figure 5.5). Assuming that subglacial AIOM in this region is a mixture of two components (Equation 5.8), we interpret the ends of this line to represent $AIOM_{pre-aged}$ and $AIOM_{recent}$ endmembers. It is likely that the highest measured ^{14}C concentrations, even with adjustments for the sampling of low-temperature aliquots (Subt et al., 2017), still reflect some portion of $AIOM_{pre-aged}$ admixed into a sample that is primarily composed of $AIOM_{recent}$. However, because the linear relationship between $\delta^{13}C$ and $\Delta^{14}C$ for organic carbon in the sub-ice environment represents mixing between $AIOM_{pre-aged}$ and $AIOM_{recent}$ endmembers, it can be used to solve for the $\Delta^{14}C$ maximum, and thus the timing over which grounding line retreat occurred along the Siple Coast during the Holocene. To avoid biases introduced by a small sample size (n=32), we adopted a Monte Carlo approach to generate 10,000 reduced major axis regressions to quantify the linear relationship between SLM $\delta^{13}C$and $\Delta^{14}C$ data (Figure 5.5). We use the full output of the Monte Carlo simulation to generate maximum $\Delta^{14}C$ for $\delta^{13}C$ values that we would expect to measure in SLM if we were able to isolate only microbially produced organic carbon with RPO (-35 to -31‰; Figure 5.5). Model realizations over this conservative range of $\delta^{13}C$ values result in a range of mean $\Delta^{14}C$ values from -518.0‰($\pm$1.8‰) to -696.1‰ ($\pm$1.0‰). By combining equations 5.6 and 5.7 above to convert $\Delta^{14}C$ values to time, we find that across all three possible $\delta^{13}C$ endmembers, exposure of SLM sediments to the marine environment occurred between 5.4 kyr B.P. and 9.5 kyr B.P. (Table 5.3). This age range falls within the range of modeled (Kingslake et al., 2018) and measured (Venturelli et al., 2020) timing for grounding line retreat in this area, and provides insight to the inland extent of this process.

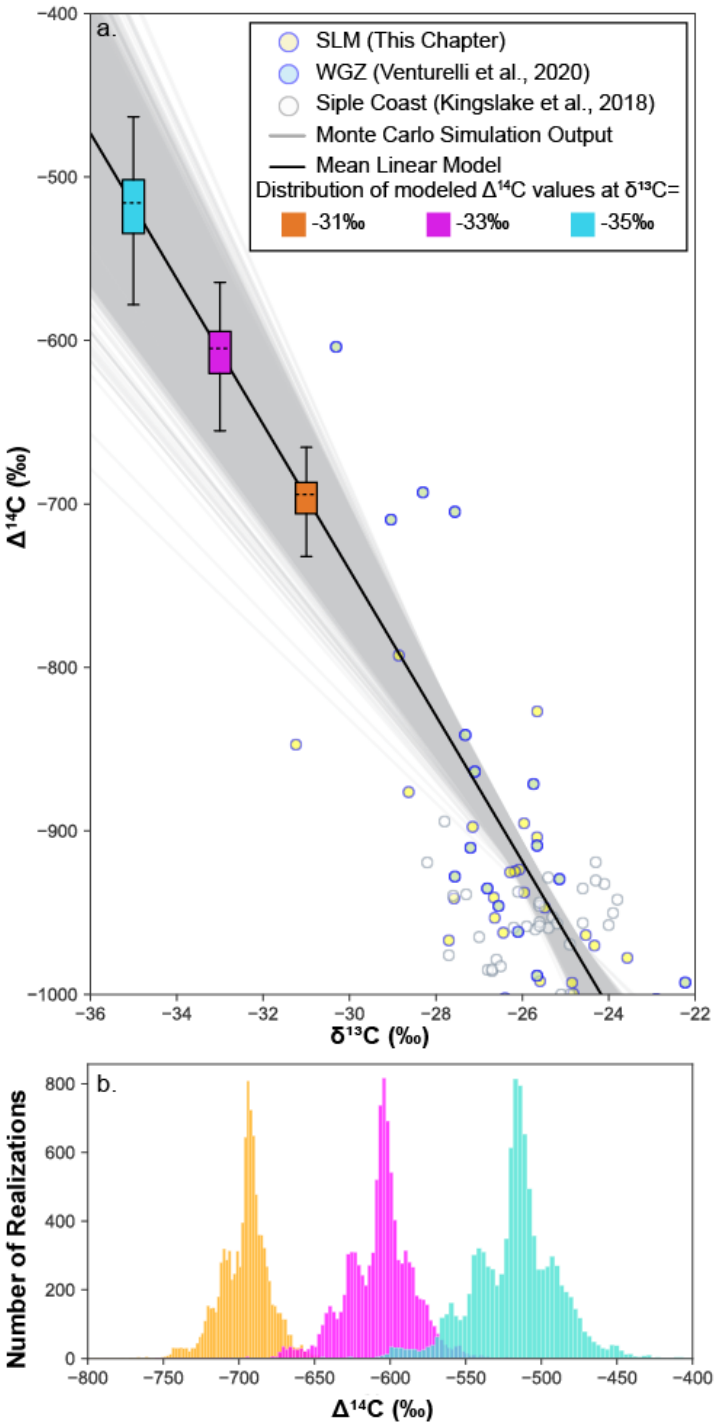

Figure 5.5: a. Linear model overlain by $\Delta^{14}C$ and $\delta^{13}C$ data for all existing sub-ice sediments collected from the Siple Coast subglacial environment. Here we display all lines calculated with the monte carlo simulation (n=10,000; gray lines), as well as the mean linear model (black line), and 95% confidence intervals for calculated $\Delta^{14}C$(‰) values at $\delta^{13}C$=-31‰(orange), -33‰(magenta), and -35‰(turquoise). (b.) includes all model realizations at the three $\delta^{13}C$ intervals for which the linear model was sampled.

Table 5.3: Linear model outputs (Δ^{14}C, f_M, and age) for three potential δ^{13}C minima.

δ^{13}C (‰)	Δ^{14}C (‰)	$\pm 2\sigma$	f_M	$\pm 2\sigma$	^{14}C yrs	$\pm 2\sigma$	Cal yrs BP (median probability)	$\pm 2\sigma$ range
-31	-696.1	0.3	0.304	0.001	9557	18	9508	9180-9888
-33	-607.0	0.4	0.393	0.001	7481	29	7241	6939-7506
-35	-518.0	0.6	0.482	0.001	5846	23	5466	5131-5774

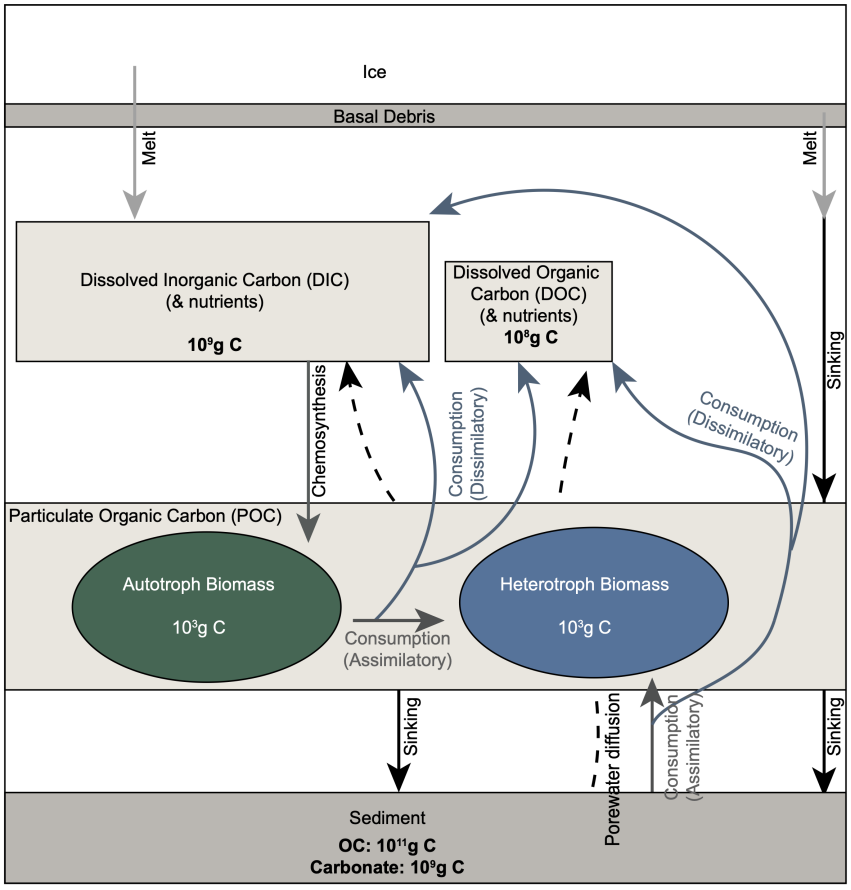

Figure 5.6: Conceptual model of the subglacial carbon cycle based on isotopic measurements from SLM.

5.4.5 Using ^{14}C as a Natural Tracer of the SLM Carbon Cycle

A single source of ^{14}C to the subglacial environment provides a natural tracer of carbon movement through the subglacial system. "New" carbon brought into the subglacial system by grounding line retreat may be subsequently transformed by biologic (assimilation and dissimilation) and geologic (porewater diffusion, basal freezing, and basal melting) processes, transferring carbon from the sedimentary reservoir to carbon reservoirs in the water column

(Figure 5.6). Using the median output from my linear model above (Δ^{14}C=-607.0‰) as a conservative estimate of the Δ^{14}C value for $AIOM_{recent}$, we calculate fluxes of ^{14}C from the sediment to other carbon reservoirs in SLM below.

^{14}C in dissolved inorganic carbon: SLM samples resulted in a DIC Δ^{14}C value of -979.2‰. Given that the source of CO_2 to the system is older than measurable with ^{14}C, we would expect SLM DIC to be devoid of ^{14}C, resulting in a Δ^{14}C value of -1000‰. However, it is likely that some CO_2 produced from remineralization of ^{14}C-bearing organic matter produced $^{14}CO_2$. Here we demonstrate this flux, updating equation 5.8 to reflect isotopic exchange:

$$(^{14}CH_2O)_x(NH_3)_y(H_3PO_4)_z + (x + 2\,y)O_2 \longrightarrow x\,^{14}CO_2 + (x + y)H_2O + yHNO_3 + zH_3PO_4 \tag{5.13}$$

If remineralization of organic carbon in SLM sediments is the only source of ^{14}C to the DIC reservoir, the flux of carbon from sediments to water column DIC can be determined with a mixing model where

$$\Delta_{\mathrm{DIC-measured}} = (p_1 \times \Delta_{input}) + (1 - p_1) \times \Delta_{\mathrm{sediment}} \tag{5.14}$$

$$(-979\,‰) = (0.946) \times (-1000\,‰) + (0.054) \times (-607.0\,‰) \tag{5.15}$$

Thus, in an SLM DIC reservoir that contains 7.69×10^9 g C, DIC_{input} accounts for 7.27×10^9 g C while the remaining 4.15×10^8 g C is produced by remineralization during the filling period of the lake. This is equivalent to a rate of 2.27×10^5 g C/day (or 1.89×10^4 mol C/day).

^{14}C in dissolved organic carbon: As indicated by equation 5.10, the SLM DOC reservoir reflects inputs from ice melt, porewater diffusion, and biologic productivity. Though basal

melt would supply ^{14}C-free DOC to SLM, heterotrophic carbon assimilation and porewater diffusion could move ^{14}C from sedimentary AIOM to the DOC reservoir. The flux of carbon from sediments to water column DOC can, again, be determined with a mixing model:

$$\Delta_{\mathrm{DOC-measured}} = (\mathrm{p}_1 \times \Delta_{input}) + (1 - \mathrm{p}_1) \times \Delta_{\mathrm{sediment}} \quad (5.16)$$

$$(-947\,‰) = (0.865) \times (-1000\,‰) + (0.135) \times (-607\,‰) \quad (5.17)$$

Thus, in an SLM DOC pool that contains 4.38×10^8 g C, a ^{14}C-free DOC$_{input}$ accounts for 3.79×10^8 g C whereas the remaining 5.91×10^7g C is transferred from the sediment by heterotrophic and porewater diffusion processes at a rate of 3.23×10^4 g C/day (2.69×10^3 mol C/day).

^{14}C in particulate organic carbon: The POC sample from SLM reflects the input of non-living POC transported by water into SLM and liberated by basal melt of the overlying ice sheet as well as the living, microbial component of the SLM water column. With the biomass previously measured in the subglacial environment (1.3×10^{-8} cells/L; Christner et al., 2014) and a cellular carbon content estimate of 1.1×10^{-14} g (Kepner et al., 1998), the intact microbial biomass within the total volume SLM would only account for 1.0×10^{-10} g C). Though the small amount of ^{14}C in SLM DIC and DOC indicates that microbial biomass would likely also contain ^{14}C, intact microbial biomass would account for a small enough portion of the POC reservoir to ignores its contribution. As such, we interpret the isotopic data from my POC sample to primarily reflect the non-living detritus in the SLM water column. Because the primary source of detritus to the subglacial hydrologic system comes from sediment entrained in basal ice that is liberated by basal melting, the POC sample collected from SLM provides an opportunity to characterize this basal debris in absence of a direct sample. Along the Siple Coast, it has been suggested that sediment entrained in basal ice [observed at Whillans and Kamb ice streams (Engelhardt & Kamb, 2013) and here (Priscu et al., in revision)] makes up 5-22% of the ice base by mass. Alley et al. (1998)

demonstrate that the origin of basal debris in this region comes from freeze-on processes at the base of these ice streams. The freeze-on and subsequent melt-out of this basal debris likely plays an important role in the distribution of sediment and associated carbon about the subglacial system. The similarity of isotopic data from the POC sample to the sediment AIOM data agree with previously proposed freeze-on processes (Alley et al., 1998). The presence of ^{14}C in our POC sample indicate that basal debris accretion likely occurred after the retreat of the grounding line along the Siple Coast supplied ^{14}C to the subglacial system.

5.4.6 Implications of This Work for Deglacial Models

Isotopic measurements from SLM sediments indicate that the grounding line retreated at least 150 km inland of the modern grounding line during the Holocene, before re-advancing to the modern position, agreeing with modeled (Kingslake et al., 2018) and measured (Venturelli et al., 2020) evidence for this process along the Siple Coast. This work highlights the importance of subglacial sediment archives for chronicling the full extent of deglacial ice dynamics, so long as we have the technical capability to separate the small amount of ^{14}C-bearing organic carbon from the large proportion of pre-aged AIOM. This work indicates that other deglacial models (Figure 5.7) in this region have been historically limited by utilizing only accessible ice-free terrestrial and marine archives for placing chronologic constraints on grounding line retreat following the Last Glacial Maximum. Whereas previous studies focused on exposed marine and terrestrial geologic archives (Conway et al., 1999; Ackert, 2008; Halberstadt et al., 2016) result in a unidirectional retreat pattern from the continental shelf edge to a modern grounding line position, studies that include subglacial geologic archives result in grounding line retreat inland of the modern position during the Holocene, followed by re-advance to a modern position (Kingslake et al., 2018; Venturelli et al., 2020, this study). To investigate the extent of grounding line retreat that may have occurred along the Siple Coast, measurements of ^{14}C in sediments and basal ice further inland than SLM could prove useful.

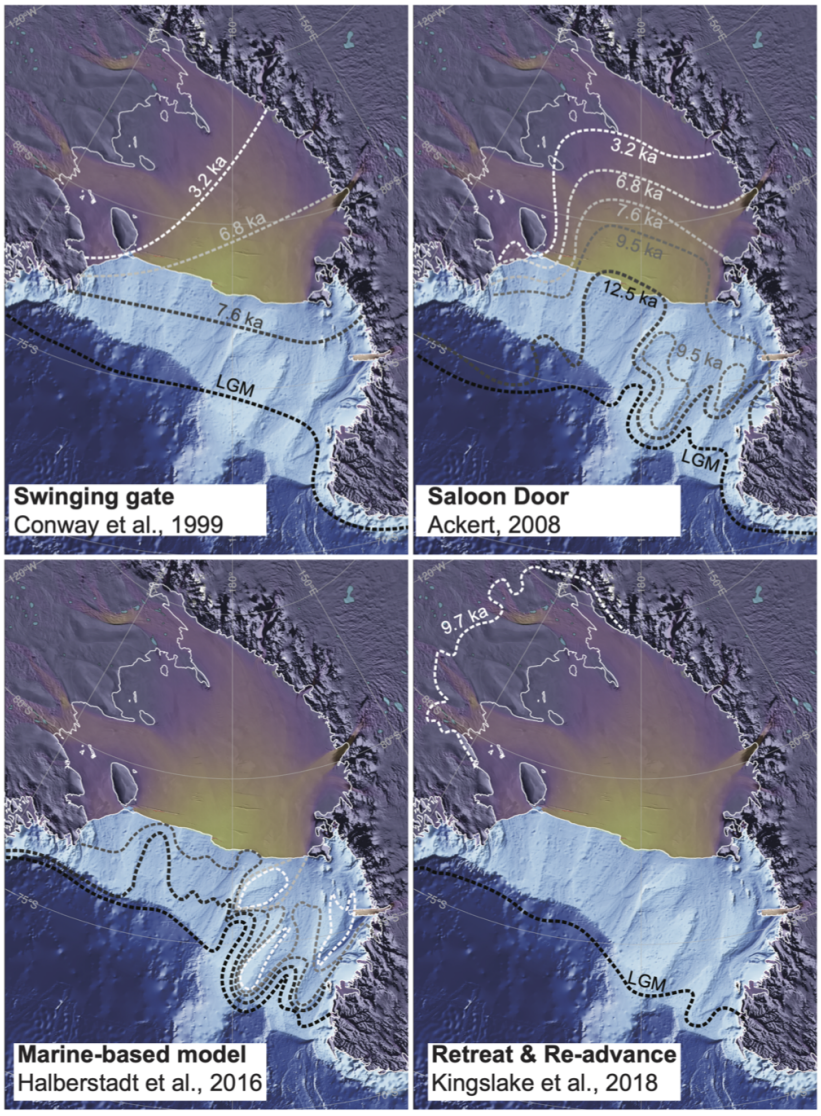

Figure 5.7: Previously published deglacial models for the Ross Sea Embayment demonstrating the timing and pattern of grounding line retreat following the Last Glacial Maximum.

5.5 Summary

To date, only two active subglacial lakes in Antarctica have been directly sampled (Christner et al., 2014; Priscu et al., in revision). Though access has been limited, the exploration of these lakes has supported early hypotheses of the persistence of unique life in the extreme subglacial environment (Christner et al., 2014; Achberger et al., 2016; Mikucki et al., 2016; Vick-Majors et al., 2016). My work demonstrates that along the Siple Coast, grounding line

retreat during the Holocene has supplied ^{14}C to the subglacial environment. The movement of ^{14}C from the sediment reservoir to dissolved carbon reservoirs in the water column highlights that marine input may be useful for the persistence of the subglacial microbial community in the extreme subglacial environment. To assess the persistence of life unaffected by the periodic marine input observed at SLM, future targets for subglacial drilling efforts should focus on lakes located further inland [e.g., South Pole Lake (Hills et al., 2020); Lake Vostok (Kapitsa et al., 1996)] that have been isolated from the atmosphere and marine environment on the order of millions, rather than thousands, of years.

5.6 Note about Ongoing SALSA Work

Ramped PyrOx ^{14}C and $\delta^{13}C$ data, coupled with linear modeling, can be used to indicate the timing over which marine carbon was recently supplied to the subglacial environment in this region. Ongoing microbial work by the SALSA Science Team will prove crucial and innovative in constraining the nature of marine input to the subglacial environment. Frequent incursions of marine water would not only supply ^{14}C to this subglacial environment, but also spike the hydrological system with marine microbial communities that show robust relationships to their origins in the sub-RIS environment. If microbial communities turn out to be divergent in SLM, environmental stability in excess of the timescale of marine incursion suggested by my work must be invoked. In such a case, marine incursions, although obviously reflective of geologic instability in terms of microbial environment (fresh to salt), would be of a nature to preserve a seed community without effecting its divergence. Such divergence generally occurs over longer time scales and in geologically stable environments. Thus, the stability of Siple Coast subglacial environments from wet till to subglacial lakes would have to achieve ecologic stability in the face of geologic instability.

5.7 Supplemental material

All SLM water (Table 5.4), sediment carbonate (Table 5.5), and sediment AIOM (Table 5.6) data are included in the tables within this section.

Table 5.4: All SLM water column isotope data.

Dissolved Inorganic Carbon									
Submitter Identification	NOSAMS Accession #	f_M	$\pm1\sigma$	Age (^{14}C yr)	$\pm1\sigma$	δ^{13}C	Δ^{14}C	$\pm1\sigma$	DIC Conc (mmol/kg)
SLM1801-01UW-C-coretop water	OS-147685	0.0206	0.0009	31,200	360	-8.64	-979.4	0.9	0.89
Lake DIC-29Dec2018-Niskin-003	OS-147646	0.0194	0.0009	31,700	360	-8.89	-980.6	0.9	0.8
Lake DIC-29Dec2018Niskin-004	OS-151584	0.0156	0.0011	33,400	550	-8.87	-984.4	1.1	0.89
Lake DIC-29Dec2018Niskin-005	OS-151585	0.0148	0.0010	33,800	560	-8.89	-985.2	1	0.94
Lake DIC-29Dec2018Niskin-006	OS-151586	0.0334	0.0010	27,300	250	-8.99	-966.6	1	0.96
Dissolved Organic Carbon									
Submitter Identification	NOSAMS Accession #	f_M	$\pm1\sigma$	Age (^{14}C yr)	$\pm1\sigma$	δ^{13}C	Δ^{14}C	$\pm1\sigma$	DOC Conc (μmol/kg)
DOC-29Dec2018Niskin	OS-151527	0.0531	0.0026	23,600	390	-25.48	-946.9	2.6	51
Particulate Organic Carbon									
Submitter Identification	NOSAMS Accession #	f_M	$\pm1\sigma$	Age (^{14}C yr)	$\pm1\sigma$	δ^{13}C	Δ^{14}C	$\pm1\sigma$	
POC-29Dec2018Niskin	OS-151530	0.0764	0.0017	20,700	180	-26.07	-923.6	1.7	

Table 5.5: All SLM sediment carbonate isotope data.

Submitter Identification	**Sample size (mg)**	**Accession #**	f_M	$\pm1\sigma$	**^{14}C yr**	$\pm1\sigma$	δ^{13}C	**Carbonate (wt.%)**	Δ^{14}C	$\pm1\sigma$
01UW-A 22-24 cm	508	OS-151627	0.0139	0.0012	34,400	700	-3.73	0.75	-986.1	1.2
01UW-A 44-46 cm	505	OS-151628	0.0125	0.0012	35,200	770	-2.83	0.88	-987.5	1.2
01FF-45-50	500	OS-151629	0.0111	0.0012	36,100	870	-2.89	1.08	-988.9	1.2
01FF-80-85	513	OS-151630	0.0096	0.0012	37,300	1,000	-2.81	1.2	-990.4	1.2
02FF 95-96	513	OS-151632	0.0100	0.0012	37,000	970	-2.92	1	-990	1.2
02FF 168-170	507	OS-151631	0.0073	0.0012	39,500	1,300	-3.08	1.25	-992.7	1.2

Table 5.6: All RPO ^{14}C and δ^{13}C data for SLM sediment as reported by NOSAMS and with corrections applied in this study. All ^{14}C data under the "USF Corrected data" header have been blank corrected following Fernandez et al. (2014). δ^{13}C data have been corrected following Hemingway et al. (2017).

		NOSAMS reported data						USF Corrected data						
Submitter Identification	Sample size (μmol	Accession #	f_M	$\pm1\sigma$	^{14}Cyr	$\pm1\sigma$	δ^{13}C	f_M	$\pm1\sigma$	^{14}C yr	$\pm1\sigma$	Δ^{14}C	$\pm1\sigma$	δ^{13}C
SLM 01UW-A 7.5-11.5 Combo (n=3)	10.3	OS-153530	0.1884	0.0014	13,400	60	-28.08	0.1731	0.009	14100	400	-826.9	8.6	-25.66
DB-1847-1, O1UW-A 16-18 cm	13.0	OS-149383	0.1180	0.0033	17,150	230	-26.16	0.1046	0.010	18150	760	-895.4	9.9	-25.96
DB-1847-2, O1UW-A 16-18 cm	11.2	OS-149384	0.0536	0.0036	23,500	540	-24.73	0.0363	0.012	26600	2700	-963.7	12.2	-24.53
DB-1847-3, O1UW-A 16-18 cm	4.6	OS-149375	0.0514	0.0030	23,800	470	-19.29	0.0095	0.028	37400	24000	-990.5	28.3	-19.09
DB-1852-1, O1UW-A 44-46 cm	9.6	OS-149377	0.0578	0.0035	22,900	490	-26.72	0.0377	0.014	26300	3000	-962.3	14.0	-26.44
DB-1852-2, O1UW-A 44-46 cm	18.4	OS-149378	0.0109	0.0036	36,300	2700	-25.1	0.0003	0.008		190600	-999.7	8.2	-24.82
DB-1852-3, O1UW-A 44-46 cm	8.7	OS-149371	0.0237	0.0020	30,100	690	-21.26	0.0004	0.016		344100	-999.6	15.6	-20.98
DB-1850-1, 02FF 148-150 cm	8.5	OS-149372	0.0558	0.0020	23,200	280	-27.35	0.0331	0.015	27400	3700	-966.9	15.4	-27.70
DB-1850-2, 02FF 148-150 cm	24.5	OS-149380	0.0165	0.0036	33,000	1800	-25.24	0.0081	0.007	38700	6500	-991.9	6.6	-25.59
DB-1850-3, 02FF 148-150 cm	7.6	OS-149373	0.0281	0.0021	28,700	610	-20	0.0016	0.018	51900	91000	-998.4	17.7	-20.35
DB-1849-1, 02FF 168-170 cm	11.1	OS-149381	0.0791	0.0035	20,400	350	-26.2	0.0623	0.012	22300	1500	-937.7	12.0	-25.96
DB-1849-2, 02FF 168-170 cm	11.6	OS-149382	0.0468	0.0035	24,600	610	-24.57	0.0298	0.012	28200	3200	-970.2	11.9	-24.33
DB-1849-3, 02FF 168-170 cm	5.4	OS-149374	0.0370	0.0026	26,500	560	-20.31	-0.0002	0.025	>AMS	>AMS	>AMS	24.9	-20.07
SLM 01FF 45-50 Combo (n=3)	8.0	OS-153539	0.1716	0.0019	14,150	90	-30.41	0.1528	0.014	15100	760	-847.2	14.4	-31.24
DB-1857-1, 01FF-2 45-50 cm	8.5	OS-149404	0.0806	0.0022	20,200	210	-26.75	0.0587	0.015	22800	2100	-941.3	15.1	-27.58
DB-1857-2, 01FF-2 45-50 cm	13.0	OS-149419	0.0228	0.0036	30,400	1300	-24.02	0.0071	0.011	39700	12400	-992.9	11.0	-24.85
DB-1857-3, 01FF-2 45-50 cm	7.0	OS-149405	0.0311	0.0024	27,900	630	-18.22	0.0025	0.019	48100	61500	-997.5	19.1	-19.05
01FF-80-85 cm Combo (n=4)	8.2	OS-151466	0.2246	0.0021	12,000	75	-29.96	0.2073	0.013	12650	520	-792.7	13.4	-28.86
DB-1856-1, 01FF-4 80-85 cm	8.1	OS-149402	0.1176	0.0020	17,200	140	-26.76	0.0962	0.015	18800	1300	-903.8	15.1	-25.66
DB-1856-2, 01FF-4 80-85 cm	13.4	OS-149418	0.0372	0.0036	26,400	770	-24.67	0.0224	0.011	30500	3800	-977.6	10.5	-23.57
DB-1856-3, 01FF-4 80-85 cm	7.1	OS-149403	0.0408	0.0029	25,700	580	-21.62	0.0127	0.019	35000	11900	-987.3	19.0	-20.52
DB-1858-1, 02FF 5-7cm	10.0	OS-149420	0.0780	0.0037	20,500	380	-26.63	0.0593	0.013	22700	1800	-940.7	13.3	-26.66
DB-1853-1, 01FF 57-58 cm	10.0	OS-149416	0.0934	0.0034	19,050	290	-26.14	0.0752	0.013	20800	1400	-924.8	13.0	-26.17
DB-1854-1, 01FF 65-66 cm	9.9	OS-149417	0.0659	0.0036	21,800	430	-26.61	0.0468	0.013	24600	2300	-953.2	13.5	-26.64
DB-1855-1, 01FF 73-74 cm	8.6	OS-149401	0.0959	0.0019	18,850	160	-26.25	0.0747	0.015	20800	1600	-925.3	14.7	-26.28

6 Concluding Remarks

The fundamental goal of paleoclimate research is to gain an understanding of variations in the geologic past so that we may better quantify and constrain how Earth's interlinked systems will adapt and respond to external perturbations in the future. In contrast to direct observations in the instrumental record, the geologic record provides indirect evidence for past changes in Earth's climate system via proxy. Any indirect observation (proxy record) comes with associated uncertainties. However, we can work to reduce these uncertainties with innovative methods that enable us to explore the geologic record in new and different ways.

6.1 Summary of Dissertation Objectives

Throughout this dissertation, I have detailed my exploration of the development, application, and optimization of newly developed isotopic techniques to address the following objectives:

1. Contribute to the advancement of the carbonate clumped isotope paleothermometer through mass spectrometric method development.

2. Develop pathways for collaboration between natural-level ^{14}C researchers and researchers applying ^{14}C-labeled tracers.

3. Apply Ramped PyrOx ^{14}C on sediments collected from ice-covered environments to explore Holocene Antarctic ice sheet history.

4. Optimize measurements of ^{14}C in a modern subglacial lake to explore the role of marine carbon in the subglacial carbon cycle.

6.1.1 Objective 1

A negative background effect called pressure baseline (PBL) can be observed in many mass spectrometers making carbonate clumped isotope (Δ_{47}) measurements. **Chapter 2** illustrates the ways in which miscorrection for PBL may result in interlaboratory differences in Δ_{47} derived paleotemperature measurements. I developed a new, empirical method to correct for PBL. The benefit to this method is that it is not instrument-specific, which makes a tool that anyone in the clumped isotope community may employ.

6.1.2 Objective 2

The risk of contamination has long forced researchers employing natural-level ^{14}C measurements to work completely separate from researchers employing ^{14}C-labelled tracers. However, such separation is not always possible (e.g., remote field camps, ocean going vessels), and the sacrifice of either may limit potential scientific outcomes of transdisciplinary research. In **Chapter 3**, I outlined a collaborative protocol for maintaining natural-level ^{14}C cleanliness in a remote field camp in Antarctica. This work provides a framework for future collaboration between researchers applying ^{14}C measurements over a high dynamic range.

6.1.3 Objective 3

The recent discovery of ^{14}C in subglacial sediments overturned paradigms surrounding the deglacial behavior of the West Antarctic Ice Sheet (Kingslake et al., 2018). However, the methods employed (bulk AIOM ^{14}C dating) in this discovery were insufficient for using ^{14}C to place chronological constraints on ice sheet change because carbon in the subglacial environment contains a high proportion of pre-aged material. In **chapters 4** and **5**, I employed Ramped PyrOx ^{14}C to separate the mixture of organic carbon present in subglacial sediments (Figure 6.1). I demonstrate that ^{14}C in sediments collected from beneath modern ice cover can be used to identify the timing (**Chapter 4**) and extent (**Chapter 5**) of Holocene grounding line retreat.

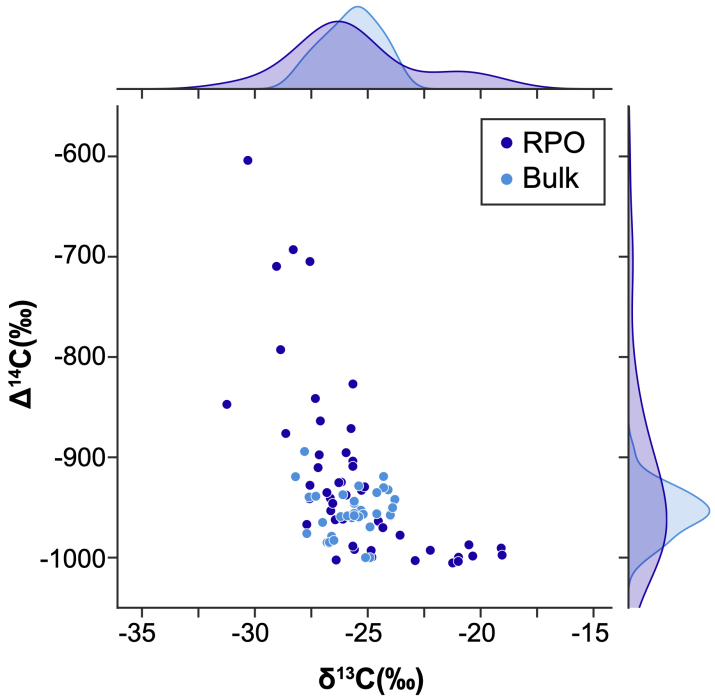

Figure 6.1: Comparison of $\Delta^{14}C$ and $\delta^{13}C$ data distributions for subglacial samples analyzed with bulk and RPO isotopic methods. All data labeled "bulk" come from Kingslake et al. (2018) and all RPO data come from chapters 4 and 5.

6.1.4 Objective 4

Finally, by ensuring a contamination-free environment (**Chapter 3**), and identifying a single source to the subglacial environment (**Chapter 4**), I demonstrated that ^{14}C provides a natural tracer of the subglacial carbon cycle. In **Chapter 5**, I calculated fluxes of ^{14}C out of subglacial sediments to demonstrate how the introduction of marine carbon may be useful to the subglacial microbial ecosystem.

6.2 Future Work

Advances in technology (mass spectrometry, sub-ice access) and isotopic techniques (Ramped PyrOx ^{14}C , clumped isotope paleothermometry) enabled me to pursue the work described in this dissertation. My work demonstrates that with methodological advances, we can optimize

even the most mixed geologic archives (sub-ice sediments) to assess changes in the recent geologic past. When paired with marine and terrestrial geologic archives, ^{14}C in subglacial sediments provides an opportunity to gain a holistic view of ice sheet history (Figure 6.2), and should be utilized in future paleoglaciological investigations of other marine-based sectors of the Antarctic Ice Sheet.

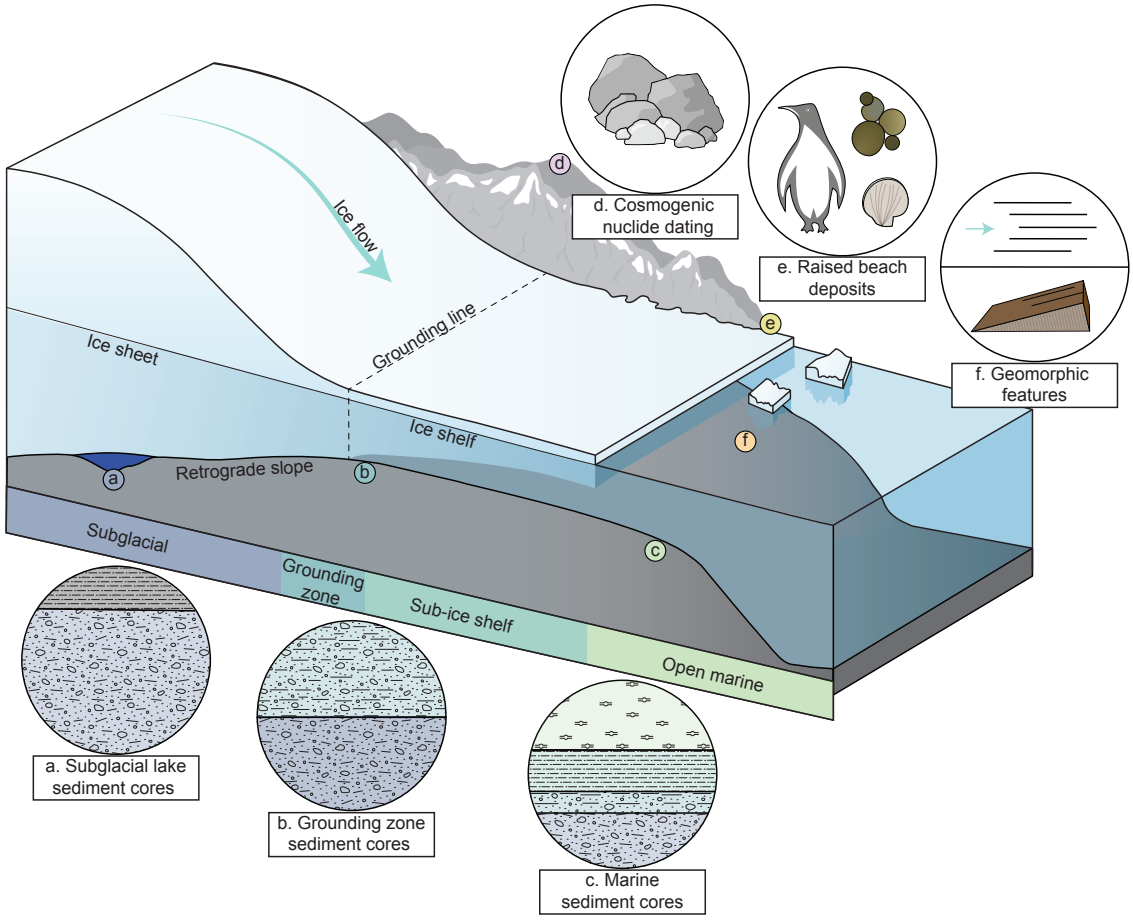

Figure 6.2: Block diagram of an idealized ice sheet illustrating potential geologic archives to be explored for paleoglaciological reconstructions

References

Achberger, A. M., Christner, B. C., Michaud, A. B., Priscu, J. C., Skidmore, M. L., & Vick-Majors, T. J. (2016). Microbial community structure of subglacial lake whillans, west antarctica. *Frontiers in Microbiology*, *7*. doi: 10.3389/fmicb.2016.01457

Ackert, R. (2008). Swinging gate or saloon doors: Do we need a new model of ross sea deglaciation. In *Fifteenth west antarctic ice sheet meeting, sterling, virginia* (Vol. 811).

Adkins, J. F. (2002). The salinity, temperature, and delta 18o of the glacial deep ocean. *Science*, *298*(5599), 1769–1773. doi: 10.1126/science.1076252

Alley, R. B. (1989). Water-Pressure Coupling of Sliding and Bed Deformation: I. Water System. *Journal of Glaciology*, *35*(119), 108–118. doi: 10.3189/002214389793701527

Alley, R. B., Anandakrishnan, S., Dupont, T. K., Parizek, B. R., & Pollard, D. (2007). Effect of Sedimentation on Ice-Sheet Grounding-Line Stability. *Science*, *315*(5820), 1838–1841. doi: 10.1126/science.1138396

Alley, R. B., Blankenship, D. D., Bentley, C. R., & Rooney, S. T. (1986). Deformation of till beneath ice stream B, West Antarctica. *Nature*, *322*(6074), 57–59. doi: 10.1038/322057a0

Alley, R. B., Lawson, D. E., Evenson, E. B., Strasser, J. C., & Larson, G. J. (1998). Glaciohydraulic supercooling: a freeze-on mechanism to create stratified, debris-rich basal ice: II. theory. *Journal of Glaciology*, *44*(148), 563–569. doi: 10.3189/s0022143000002070

Anand, P., Elderfield, H., & Conte, M. H. (2003). Calibration of Mg/Ca thermometry in planktonic foraminifera from a sediment trap time series. *Paleoceanography*, *18*(2), 1050. doi: 10.1029/2002pa000846

Anandakrishnan, S., Catania, G. A., Alley, R. B., & Horgan, H. J. (2007). Discovery of Till Deposition at the Grounding Line of Whillans Ice Stream. *Science*, *315*(5820), 1835–1838. doi: 10.1126/science.1138393

Anderson, J. B., Conway, H., Bart, P. J., Witus, A. E., Greenwood, S. L., McKay, R. M., ... Stone, J. O. (2014). Ross Sea paleo-ice sheet drainage and deglacial history during and since the LGM. *Quaternary Science Reviews*, *100*, 31–54. doi: 10.1016/j.quascirev.2013.08.020

Anderson, J. B., Shipp, S. S., Lowe, A. L., Wellner, J. S., & Mosola, A. B. (2002). The Antarctic Ice Sheet during the Last Glacial Maximum and its subsequent retreat history: a review. *Quaternary Science Reviews*, *21*(1-3), 49–70. doi: 10.1016/s0277-3791(01)00083-x

Arnold, J. R., & Libby, W. F. (1949). Age determinations by radiocarbon content: Checks with samples of known age. *Science*, *110*(2869), 678–680. doi: 10.1126/science.110.2869.678

Baltar, F., & Herndl, G. J. (2019). Is dark carbon fixation relevant for oceanic primary production estimates? *Biogeosciences*, *16*(19), 3793–3799. doi: 10.5194/bg-16-3793-2019

Bamber, J. L., Oppenheimer, M., Kopp, R. E., Aspinall, W. P., & Cooke, R. M. (2019). Ice sheet contributions to future sea-level rise from structured expert judgment. *Proceedings of the National Academy of Sciences*, *116*(23), 11195–11200. doi: 10.1073/pnas.1817205116

Bao, R., McNichol, A. P., Hemingway, J. D., Gaylord, M. C. L., & Eglinton, T. I. (2018). Influence of Different Acid Treatments on the Radiocarbon Content Spectrum of Sedimentary Organic Matter Determined by RPO/Accelerator Mass Spectrometry. *Radiocarbon*, *61*(2), 395–413. doi: 10.1017/rdc.2018.125

Bart, P. J., Anderson, J. B., & Nitsche, F. (2017). Post-LGM Grounding-Line Positions of the Bindschadler Paleo Ice Stream in the Ross Sea Embayment, Antarctica. *Journal of Geophysical Research: Earth Surface*, *122*(10), 1827–1844. doi: 10.1002/2017jf004259

Bart, P. J., Krogmeier, B. J., Bart, M. P., & Tulaczyk, S. (2017). The paradox of a long grounding during West Antarctic Ice Sheet retreat in Ross Sea. *Scientific Reports*, *7*(1). doi: 10.1038/s41598-017-01329-8

Beaupré, S. R., Druffel, E. R. M., & Griffin, S. (2007). A low-blank photochemical extraction system for concentration and isotopic analyses of marine dissolved organic carbon. *Limnology and Oceanography: Methods*, *5*(6), 174–184. doi: 10.4319/lom.2007.5.174

Beck, J. W., Edwards, R. L., Ito, E., Taylor, F. W., Recy, J., Rougerie, F., ... Henin, C. (1992). Sea-surface temperature from coral skeletal strontium/calcium ratios. *Science*, *257*(5070), 644–647. doi: 10.1126/science.257.5070.644

Beem, L. H., Jezek, K. C., & Veen, C. V. D. (2010). Basal melt rates beneath Whillans Ice Stream, West Antarctica. *Journal of Glaciology*, *56*(198), 647–654. doi: 10.3189/002214310793146241

Begeman, C. B., Tulaczyk, S., Padman, L., King, M., Siegfried, M. R., Hodson, T. O., & Fricker, H. A. (2020). Tidal Pressurization of the Ocean Cavity Near an Antarctic Ice Shelf Grounding Line. *Journal of Geophysical Research: Oceans*, *125*(4). doi: 10.1029/2019jc015562

Begeman, C. B., Tulaczyk, S. M., Marsh, O. J., Mikucki, J. A., Stanton, T. P., Hodson, T. O., ... King, M. A. (2018). Ocean Stratification and Low Melt Rates at the Ross Ice

Shelf Grounding Zone. *Journal of Geophysical Research: Oceans*, *123*(10), 7438–7452. doi: 10.1029/2018jc013987

Behrendt, J. (1999). Crustal and lithospheric structure of the west antarctic rift system from geophysical investigations a review. *Global and Planetary Change*, *23*(1-4), 25–44. doi: 10.1016/s0921-8181(99)00049-1

Behrendt, J. C., LeMasurier, W. E., Cooper, A. K., Tessensohn, F., Tréhu, A., & Damaske, D. (1991). Geophysical studies of the west antarctic rift system. *Tectonics*, *10*(6), 1257–1273. doi: 10.1029/91tc00868

Bell, R. E. (2008). The role of subglacial water in ice-sheet mass balance. *Nature Geoscience*, *1*(5), 297–304. doi: 10.1038/ngeo186

Bell, R. E., Studinger, M., Karner, G., Finn, C. A., & Blankenship, D. D. (n.d.). Identifying major sedimentary basins beneath the west antarctic ice sheet from aeromagnetic data analysis. In *Antarctica* (pp. 117–121). Springer-Verlag.

Bentley, M. J., Christoffersen, P., Hodgson, D. A., Smith, A. M., Tulaczyk, S., & Brocq, A. M. L. (2011). Subglacial lake sediments and sedimentary processes: Potential archives of ice sheet evolution, past environmental change, and the presence of life. In *Geophysical monograph series* (pp. 83–110). American Geophysical Union. doi: 10.1029/2010gm000940

Bentley, M. J., Ó Cofaigh, C., Anderson, J. B., Conway, H., Davies, B., Graham, A. G., ... Zwartz, D. (2014). A community-based geological reconstruction of Antarctic Ice Sheet deglaciation since the Last Glacial Maximum. *Quaternary Science Reviews*, *100*, 1–9. doi: 10.1016/j.quascirev.2014.06.025

Bernasconi, S. M., Hu, B., Wacker, U., Fiebig, J., Breitenbach, S. F. M., & Rutz, T. (2013). Background effects on Faraday collectors in gas-source mass spectrometry and implica-

tions for clumped isotope measurements. *Rapid Communications in Mass Spectrometry*, *27*(5), 603–612. doi: 10.1002/rcm.6490

Bernasconi, S. M., Müller, I. A., Bergmann, K. D., Breitenbach, S. F. M., Fernandez, A., Hodell, D. A., ... Ziegler, M. (2018). Reducing Uncertainties in Carbonate Clumped Isotope Analysis Through Consistent Carbonate-Based Standardization. *Geochemistry, Geophysics, Geosystems*, *19*(9), 2895–2914. doi: 10.1029/2017gc007385

Beukens, C. L. B. R. P., Clover, M. R., Gove, H. E., Liebert, R. B., Litherland, A. E., Purser, K. H., & Sondheim, W. E. (1977). Radiocarbon Dating Using Electrostatic Accelerators: Negative Ions Provide the Key. *Science*, *198*(4316), 508–510. doi: 10.1126/science.198.4316.508

Bindschadler, R., Vornberger, P., Blankenship, D., Scambos, T., & Jacobel, R. (1996). Surface velocity and mass balance of ice streams d and e, west antarctica. *Journal of Glaciology*, *42*(142), 461–475. doi: 10.3189/s0022143000003452

Blankenship, D. D., Bentley, C. R., Rooney, S. T., & Alley, R. B. (1986). Seismic measurements reveal a saturated porous layer beneath an active antarctic ice stream. *Nature*, *322*(6074), 54–57. doi: 10.1038/322054a0

Blankenship, D. D., Bentley, C. R., Rooney, S. T., & Alley, R. B. (1987). Till beneath ice stream b: 1. properties derived from seismic travel times. *Journal of Geophysical Research*, *92*(B9), 8903. doi: 10.1029/jb092ib09p08903

Brand, W. A., Assonov, S. S., & Coplen, T. B. (2010). Correction for the ^{17}O interference in $\delta(^{13}\mathrm{C})$ measurements when analyzing CO_2 with stable isotope mass spectrometry (IUPAC Technical Report). *Pure and Applied Chemistry*, *82*(8), 1719–1733. doi: 10.1351/pac-rep-09-01-05

Broecker, W. (1982). *Tracers in the sea* (Vol. 24) (No. 3). Cambridge University Press (CUP). doi: 10.1017/s0033822200005221

Brohan, P., Kennedy, J. J., Harris, I., Tett, S. F. B., & Jones, P. D. (2006). Uncertainty estimates in regional and global observed temperature changes: A new data set from 1850. *Journal of Geophysical Research*, *111*(D12). doi: 10.1029/2005jd006548

Buchholz, B. A., Freeman, S. P., Haack, K. W., & Vogel, J. S. (2000). Tips and traps in the ^{14}c bio-AMS preparation laboratory. *Nuclear Instruments and Methods in Physics Research Section B: Beam Interactions with Materials and Atoms*, *172*(1-4), 404–408. doi: 10.1016/s0168-583x(00)00142-7

Buizert, C., Cuffey, K. M., Severinghaus, J. P., Baggenstos, D., Fudge, T. J., Steig, E. J., ... Taylor, K. C. (2015). The WAIS divide deep ice core WD2014 chronology – part 1: Methane synchronization (68–31 ka BP) and the gas age–ice age difference. *Climate of the Past*, *11*(2), 153–173. doi: 10.5194/cp-11-153-2015

Carter, S., & Fricker, H. (2012). The supply of subglacial meltwater to the grounding line of the Siple Coast, West Antarctica. *Annals of Glaciology*, *53*(60), 267–280. doi: 10.3189/2012aog60a119

Carter, S., Fricker, H., & Siegfried, M. (2013). Evidence of rapid subglacial water piracy under whillans ice stream, west antarctica. *Journal of Glaciology*, *59*(218), 1147–1162. doi: 10.3189/2013jog13j085

Chanton, J., Zhao, T., Rosenheim, B. E., Joye, S., Bosman, S., Brunner, C., ... Hollander, D. (2014). Using natural abundance radiocarbon to trace the flux of petrocarbon to the seafloor following the deepwater horizon oil spill. *Environmental Science & Technology*, *49*(2), 847–854. doi: 10.1021/es5046524

Chanton, J. P., Burnett, W. C., Dulaiova, H., Corbett, D. R., & Taniguchi, M. (2003). Seepage rate variability in florida bay driven by atlantic tidal height. *Biogeochemistry*, *66*(1/2), 187–202. doi: 10.1023/b:biog.0000006168.17717.91

Christianson, K., Jacobel, R. W., Horgan, H. J., Alley, R. B., Anandakrishnan, S., Holland, D. M., & DallaSanta, K. J. (2016). Basal conditions at the grounding zone of Whillans Ice Stream, West Antarctica, from ice-penetrating radar. *Journal of Geophysical Research: Earth Surface*, *121*(11), 1954–1983. doi: 10.1002/2015jf003806

Christianson, K., Parizek, B. R., Alley, R. B., Horgan, H. J., Jacobel, R. W., Anandakrishnan, S., ... Muto, A. (2013). Ice sheet grounding zone stabilization due to till compaction. *Geophysical Research Letters*, *40*(20), 5406–5411. doi: 10.1002/2013gl057447

Christner, B. C., Priscu, J. C., Achberger, A. M., Barbante, C., Carter, S. P., Christianson, K., ... the WISSARD Science Team (2014). A microbial ecosystem beneath the west antarctic ice sheet. *Nature*, *512*(7514), 310–313. doi: 10.1038/nature13667

Christoffersen, P., Tulaczyk, S., & Behar, A. (2010). Basal ice sequences in Antarctic ice stream: Exposure of past hydrologic conditions and a principal mode of sediment transfer. *Journal of Geophysical Research*, *115*(F3). doi: 10.1029/2009jf001430

Church, J. A., Clark, P. U., Cazenave, A., Gregory, J. M., Jevrejeva, S., Levermann, A., ... others (2013). *Sea level change.*

Clark, P. U., Dyke, A. S., Shakun, J. D., Carlson, A. E., Clark, J., Wohlfarth, B., ... McCabe, A. M. (2009). The last glacial maximum. *Science*, *325*(5941), 710–714. doi: 10.1126/science.1172873

Clough, J. W., & Hansen, B. L. (1979). The Ross Ice Shelf Project. *Science*, *203*(4379), 433–434. doi: 10.1126/science.203.4379.433

Coenen, J. J., Scherer, R. P., Baudoin, P., Warny, S., neda, I. S. C., & Askin, R. (2019). Paleogene Marine and Terrestrial Development of the West Antarctic Rift System. *Geophysical Research Letters*, *47*(3). doi: 10.1029/2019gl085281

Cole, J. E., Fairbanks, R. G., & Shen, G. T. (1993). Recent Variability in the Southern Oscillation: Isotopic Results from a Tarawa Atoll Coral. *Science*, *260*(5115), 1790–1793. doi: 10.1126/science.260.5115.1790

Conway, H., Hall, B. L., Denton, G. H., Gades, A. M., & Waddington, E. D. (1999). Past and Future Grounding-Line Retreat of the West Antarctic Ice Sheet. *Science*, *286*(5438), 280–283. doi: 10.1126/science.286.5438.280

Cooper, A. K., Barrett, P. J., Hinz, K., Traube, V., Letichenkov, G., & Stagg, H. M. (1991). Cenozoic prograding sequences of the antarctic continental margin: a record of glacio-eustatic and tectonic events. *Marine Geology*, *102*(1-4), 175–213. doi: 10.1016/0025-3227(91)90008-r

Daëron, M., Blamart, D., Peral, M., & Affek, H. (2016). Absolute isotopic abundance ratios and the accuracy of $\Delta_4 7$ measurements. *Chemical Geology*, *442*, 83–96. doi: 10.1016/j.chemgeo.2016.08.014

DeConto, R. M., & Pollard, D. (2016). Contribution of Antarctica to past and future sea-level rise. *Nature*, *531*(7596), 591–597. doi: 10.1038/nature17145

Defliese, W. F., Hren, M. T., & Lohmann, K. C. (2015). Compositional and temperature effects of phosphoric acid fractionation on δ_{47} analysis and implications for discrepant calibrations. *Chemical Geology*, *396*, 51–60. doi: 10.1016/j.chemgeo.2014.12.018

Delaney, M. L., W.H.Bé, A., & Boyle, E. A. (1985). Li, Sr, Mg, and Na in foraminiferal calcite shells from laboratory culture, sediment traps, and sediment cores. *Geochimica et Cosmochimica Acta*, *49*(6), 1327–1341. doi: 10.1016/0016-7037(85)90284-4

Dennis, K. J., Affek, H. P., Passey, B. H., Schrag, D. P., & Eiler, J. M. (2011). Defining an absolute reference frame for 'clumped' isotope studies of CO_2. *Geochimica et Cosmochimica Acta*, *75*(22), 7117–7131. doi: 10.1016/j.gca.2011.09.025

Depoorter, M. A., Bamber, J. L., Griggs, J. A., Lenaerts, J. T. M., Ligtenberg, S. R. M., van den Broeke, M. R., & Moholdt, G. (2013). Calving fluxes and basal melt rates of Antarctic ice shelves. *Nature*, *502*(7469), 89–92. doi: 10.1038/nature12567

Dutton, A., Carlson, A. E., Long, A. J., Milne, G. A., Clark, P. U., DeConto, R., ... Raymo, M. E. (2015). Sea-level rise due to polar ice-sheet mass loss during past warm periods. *Science*, *349*(6244), aaa4019–aaa4019. doi: 10.1126/science.aaa4019

Eglinton, T. I., Benitez-Nelson, B. C., Pearson, A., McNichol, A. P., Bauer, J. E., & Druffel, E. R. (1997). Variability in radiocarbon ages of individual organic compounds from marine sediments. *Science*, *277*(5327), 796–799. doi: 10.1126/science.277.5327.796

Eiler, J. M. (2007). "Clumped-isotope" geochemistry—The study of naturally-occurring, multiply-substituted isotopologues. *Earth and Planetary Science Letters*, *262*(3–4), 309–327. doi: 10.1016/j.epsl.2007.08.020

Eiler, J. M. (2011). Paleoclimate reconstruction using carbonate clumped isotope thermometry. *Quaternary Science Reviews*, *30*(25-26), 3575–3588. doi: 10.1016/j.quascirev.2011.09.001

Eiler, J. M., & Schauble, E. (2004). $^{18}O^{13}C^{16}O$ in Earth's atmosphere. *Geochimica et Cosmochimica Acta*, *68*(23), 4767–4777. doi: 10.1016/j.gca.2004.05.035

Elderfield, H., Yu, J., Anand, P., Kiefer, T., & Nyland, B. (2006). Calibrations for benthic foraminiferal Mg/Ca paleothermometry and the carbonate ion hypothesis. *Earth and Planetary Science Letters*, *250*(3–4), 633–649. doi: 10.1016/j.epsl.2006.07.041

Emiliani, C. (1955). Pleistocene Temperatures. *The Journal of Geology*, *63*(6), 538–578. doi: 10.1086/626295

Engelhardt, H., Humphrey, N., Kamb, B., & Fahnestock, M. (1990). Physical Conditions at the Base of a Fast Moving Antarctic Ice Stream. *Science*, *248*(4951), 57–59. doi: 10.1126/science.248.4951.57

Engelhardt, H., & Kamb, B. (2013). Kamb ice stream flow history and surge potential. *Annals of Glaciology*, *54*(63), 287–298. doi: 10.3189/2013aog63a535

Evans, D., Sagoo, N., Renema, W., Cotton, L. J., Müller, W., Todd, J. A., ... Affek, H. P. (2018). Eocene greenhouse climate revealed by coupled clumped isotope-mg/ca thermometry. *Proceedings of the National Academy of Sciences*, *115*(6), 1174–1179. doi: 10.1073/pnas.1714744115

Experiment in visual orientation during nights in the Antarctic. (1960). *Soviet Antarctic Expedition Information Bulletin*, *2*, 233–234.

Felis, T., Pätzold, J., Loya, Y., Fine, M., Nawar, A. H., & Wefer, G. (2000). A coral oxygen isotope record from the northern Red Sea documenting NAO, ENSO, and north pacific teleconnections on middle east climate variability since the year 1750. *Paleoceanography*, *15*(6), 679–694. doi: 10.1029/1999pa000477

Fernandez, A., Santos, G. M., Williams, E. K., Pendergraft, M. A., Vetter, L., & Rosenheim, B. E. (2014). Blank Corrections for Ramped Pyrolysis Radiocarbon Dating of Sedimentary and Soil Organic Carbon. *Analytical Chemistry*, *86*(24), 12085–12092. doi: 10.1021/ac502874j

Fernandez, A., Tang, J., & Rosenheim, B. E. (2014). Siderite 'clumped' isotope thermometry: A new paleoclimate proxy for humid continental environments. *Geochimica et Cosmochimica Acta*, *126*, 411–421. doi: 10.1016/j.gca.2013.11.006

Fisher, A. T., Mankoff, K. D., Tulaczyk, S. M., Tyler, S. W., & and, N. F. (2015). High geothermal heat flux measured below the west antarctic ice sheet. *Science Advances*, *1*(6), e1500093. doi: 10.1126/sciadv.1500093

Fricker, H. A., & Scambos, T. (2009). Connected subglacial lake activity on lower mercer and whillans ice streams, west antarctica, 2003–2008. *Journal of Glaciology*, *55*(190), 303–315. doi: 10.3189/002214309788608813

Fricker, H. A., Scambos, T., Bindschadler, R., & Padman, L. (2007). An active subglacial water system in west antarctica mapped from space. *Science*, *315*(5818), 1544–1548. doi: 10.1126/science.1136897

Gagan, M. K., Ayliffe, L. K., Hopley, D., Cali, J. A., Mortimer, G. E., Chappell, J., ... Head, M. J. (1998). Temperature and Surface-Ocean Water Balance of the Mid-Holocene Tropical Western Pacific. *Science*, *279*(5353), 1014–1018. doi: 10.1126/science.279.5353.1014

Ghosh, P., Adkins, J., Affek, H., Balta, B., Guo, W., Schauble, E. A., ... Eiler, J. M. (2006). ^{13}C–^{18}O bonds in carbonate minerals: A new kind of paleothermometer. *Geochimica et Cosmochimica Acta*, *70*(6), 1439–1456. doi: 10.1016/j.gca.2005.11.014

Godwin, H. (1962). Half-life of radiocarbon. *Nature*, *195*(4845), 984–984. doi: 10.1038/195984a0

Goehring, B. M., Schaefer, J. M., Schluechter, C., Lifton, N. A., Finkel, R. C., Jull, A. J. T., ... Alley, R. B. (2011). The Rhone Glacier was smaller than today for most of the Holocene. *Geology*, *39*(7), 679–682. doi: 10.1130/g32145.1

Golledge, N. R., Kowalewski, D. E., Naish, T. R., Levy, R. H., Fogwill, C. J., & Gasson, E. G. W. (2015). The multi-millennial Antarctic commitment to future sea-level rise. *Nature*, *526*(7573), 421–425. doi: 10.1038/nature15706

Gomez, N., Mitrovica, J. X., Tamisiea, M. E., & Clark, P. U. (2010). A new projection of sea level change in response to collapse of marine sectors of the Antarctic Ice Sheet. *Geophysical Journal International*, *180*(2), 623–634. doi: 10.1111/j.1365-246x.2009.04419.x

Gonfiantini, R., Stichler, W., & Rozanski, K. (1995). *Standards and intercomparison materials distributed by the International Energy Agency for stable isotope measurements (IAEA-TECDOC-825)*. International Atomic Energy Agency.

Goodge, J. W. (2020). Geological and tectonic evolution of the transantarctic mountains, from ancient craton to recent enigma. *Gondwana Research*, *80*, 50–122. doi: 10.1016/j.gr.2019.11.001

Greenwood, S. L., Simkins, L. M., Halberstadt, A. R. W., Prothro, L. O., & Anderson, J. B. (2018). Holocene reconfiguration and readvance of the East Antarctic Ice Sheet. *Nature Communications*, *9*(1). doi: 10.1038/s41467-018-05625-3

Griffin, S., Beaupré, S. R., & Druffel, E. R. M. (2010). An alternate method of diluting dissolved organic carbon seawater samples for 14c analysis. *Radiocarbon*, *52*(3), 1224–1229. doi: 10.1017/s0033822200046300

Halberstadt, A. R. W., Simkins, L. M., Greenwood, S. L., & Anderson, J. B. (2016). Past ice-sheet behaviour: retreat scenarios and changing controls in the Ross Sea, Antarctica. *The Cryosphere*, *10*(3), 1003–1020. doi: 10.5194/tc-10-1003-2016

Hall, B. L., & Denton, G. H. (2000). Radiocarbon Chronology of Ross Sea Drift, Eastern Taylor Valley, Antarctica: Evidence for a Grounded Ice Sheet in the Ross Sea at the Last Glacial Maximum. *Geografiska Annaler, Series A: Physical Geography*, *82A*(2&3), 305–336. doi: 10.1111/1468-0459.00127

Hall, B. L., Denton, G. H., Stone, J. O., & Conway, H. (2013). History of the grounded ice sheet in the Ross Sea sector of Antarctica during the Last Glacial Maximum and the last termination. *Geological Society, London, Special Publications*, *381*(1), 167–181. doi: 10.1144/sp381.5

Hall, B. L., Henderson, G. M., Baroni, C., & Kellogg, T. B. (2010). Constant Holocene Southern-Ocean ^{14}C reservoir ages and ice-shelf flow rates. *Earth and Planetary Science Letters*, *296*(1–2), 115–123. doi: 10.1016/j.epsl.2010.04.054

Hall, M. M., & Bryden, H. L. (1982). Direct estimates and mechanisms of ocean heat transport. *Deep Sea Research Part A. Oceanographic Research Papers*, *29*(3), 339–359. doi: 10.1016/0198-0149(82)90099-1

Harwood, D. M., Scherer, R. P., & Webb, P.-N. (1989). Multiple Miocene marine productivity events in West Antarctica as recorded in upper Miocene sediments beneath the Ross Ice Shelf (Site J-9). *Marine Micropaleontology*, *15*(1-2), 91–115. doi: 10.1016/0377-8398(89)90006-6

Hauer, M. E., Evans, J. M., & Mishra, D. R. (2016). Millions projected to be at risk from sea-level rise in the continental united states. *Nature Climate Change*, *6*(7), 691–695. doi: 10.1038/nclimate2961

Hawkings, J. R., Skidmore, M. L., Wadham, J. L., Priscu, J. C., Morton, P. L., Hatton, J. E., ... and, R. G. M. S. (2020). Enhanced trace element mobilization by Earth's ice sheets. *Proceedings of the National Academy of Sciences*, *117*(50), 31648–31659. doi: 10.1073/pnas.2014378117

He, B., Olack, G. A., & Colman, A. S. (2012). Pressure baseline correction and high-precision CO_2 clumped-isotope (Δ_{47}) measurements in bellows and micro-volume modes. *Rapid Communications in Mass Spectrometry*, *26*(24), 2837–2853. doi: 10.1002/rcm.6436

Heaton, T. J., Köhler, P., Butzin, M., Bard, E., Reimer, R. W., Austin, W. E. N., ... Skinner, L. C. (2020). Marine20—The Marine Radiocarbon Age Calibration Curve (0–55,000 cal BP). *Radiocarbon*, *62*(4), 779–820. doi: 10.1017/rdc.2020.68

Hemingway, J. D. (2017). *Fluvialseds/Rampedpyrox: Biogeosciences Companion Code.* Zenodo. doi: 10.5281/ZENODO.839815

Hemingway, J. D., Galy, V. V., Gagnon, A. R., Grant, K. E., Rosengard, S. Z., Soulet, G., ... McNichol, A. P. (2017). Assessing the blank carbon contribution, isotope mass balance, and kinetic isotope fractionation of the ramped pyrolysis/oxidation instrument at NOSAMS. *Radiocarbon*, *59*(1), 179–193. doi: 10.1017/rdc.2017.3

Hemingway, J. D., Rothman, D. H., Rosengard, S. Z., & Galy, V. V. (2017). Technical note: An inverse method to relate organic carbon reactivity to isotope composition from serial oxidation. *Biogeosciences*, *14*(22), 5099–5114. doi: 10.5194/bg-14-5099-2017

Hill, P. G., Warwick, P. E., & Zubkov, M. V. (2013). Low microbial respiration of leucine at ambient oceanic concentration in the mixed layer of the central Atlantic Ocean. *Limnology and Oceanography*, *58*(5), 1597–1604. doi: 10.4319/lo.2013.58.5.1597

Hills, B. H., Christianson, K., & Holschuh, N. (2020). A framework for attenuation method selection evaluated with ice-penetrating radar data at south pole lake. *Annals of Glaciology*, *61*(81), 176–187. doi: 10.1017/aog.2020.32

Hodson, T., Powell, R., Brachfeld, S., Tulaczyk, S., & Scherer, R. (2016). Physical processes in Subglacial Lake Whillans, West Antarctica: Inferences from sediment cores. *Earth and Planetary Science Letters*, *444*, 56–63. doi: 10.1016/j.epsl.2016.03.036

Horgan, H. J., Alley, R. B., Christianson, K., Jacobel, R. W., Anandakrishnan, S., Muto, A., ... Siegfried, M. R. (2013). Estuaries beneath ice sheets. *Geology*, *41*(11), 1159–1162. doi: 10.1130/g34654.1

Horgan, H. J., Christianson, K., Jacobel, R. W., Anandakrishnan, S., & Alley, R. B. (2013). Sediment deposition at the modern grounding zone of Whillans Ice Stream, West Antarctica. *Geophysical Research Letters*, *40*(15), 3934–3939. doi: 10.1002/grl.50712

Horrigan, S. G. (1981). Primary production under the Ross Ice Shelf, Antarctica1. *Limnology and Oceanography*, *26*(2), 378–382. doi: 10.4319/lo.1981.26.2.0378

House, C. H. (1999). *Carbon isotopic fractionation by diverse extant and fossil prokaryotes and microbial phylogenetic diversity revealed through genomics* (Unpublished doctoral dissertation). University of California, Los Angeles.

House, C. H., Schopf, J., & Stetter, K. O. (2003). Carbon isotopic fractionation by archaeans and other thermophilic prokaryotes. *Organic Geochemistry*, *34*(3), 345–356. doi: 10.1016/s0146-6380(02)00237-1

Hu, B., Radke, J., Schl uter, H.-J., Heine, F. T., Zhou, L., & Bernasconi, S. M. (2014). A modified procedure for gas-source isotope ratio mass spectrometry: the long-integration dual-inlet (LIDI) methodology and implications for clumped isotope measurements. *Rapid Communications in Mass Spectrometry*, *28*(13), 1413–1425. doi: 10.1002/rcm.6909

Hughes, T. (1973). Is the west Antarctic Ice Sheet disintegrating? *Journal of Geophysical Research*, *78*(33), 7884–7910. doi: 10.1029/jc078i033p07884

Huntington, K. W., Eiler, J. M., Affek, H. P., Guo, W., Bonifacie, M., Yeung, L. Y., ... Came, R. (2009). Methods and limitations of 'clumped' CO_2 isotope (Δ_{47}) analysis by gas-source isotope ratio mass spectrometry. *Journal of Mass Spectrometry*, *44*(9), 1318–1329. doi: 10.1002/jms.1614

Jacobel, R. W., Christianson, K., Wood, A. C., Dallasanta, K. J., & Gobel, R. M. (2014). Morphology of basal crevasses at the grounding zone of Whillans Ice Stream, West Antarctica. *Annals of Glaciology*, *55*(67), 57–63. doi: 10.3189/2014aog67a004

Jahnke, L. L., Summons, R. E., Hope, J. M., & Marais, D. J. D. (1999). Carbon isotopic fractionation in lipids from methanotrophic bacteria II: the effects of physiology and

environmental parameters on the biosynthesis and isotopic signatures of biomarkers. *Geochimica et Cosmochimica Acta*, *63*(1), 79–93. doi: 10.1016/s0016-7037(98)00270-1

Jankowski, E. J., & Drewry, D. J. (1981). The structure of west antarctica from geophysical studies. *Nature*, *291*(5810), 17–21. doi: 10.1038/291017a0

Joughin, I., Shean, D. E., Smith, B. E., & Dutrieux, P. (2016). Grounding line variability and subglacial lake drainage on Pine Island Glacier, Antarctica. *Geophysical Research Letters*, *43*(17), 9093–9102. doi: 10.1002/2016gl070259

Joughin, I., Smith, B. E., & Medley, B. (2014). Marine ice sheet collapse potentially under way for the thwaites glacier basin, west antarctica. *Science*, *344*(6185), 735–738. doi: 10.1126/science.1249055

Kamb, B. (2001). Basal zone of the west antarctic ice streams and its role in lubrication of their rapid motion. In R. B. Alley & R. A. Bindschadler (Eds.), *The west antarctic ice sheet: Behavior and environment* (Vol. 77, pp. 157–199). Washington, D.C.: American Geophysical Union. doi: 10.1029/ar077p0157

Kapitsa, A. P., Ridley, J. K., de Q. Robin, G., Siegert, M. J., & Zotikov, I. A. (1996). A large deep freshwater lake beneath the ice of central east antarctica. *Nature*, *381*(6584), 684–686. doi: 10.1038/381684a0

Kennett, J. P. (1968). *The fauna of the ross sea: part 6: ecology and distribution of foraminifera*. Department of Scientific and Industrial Research.

Kepner, R. L., Wharton, R. A., & Suttle, C. A. (1998). Viruses in antarctic lakes. *Limnology and Oceanography*, *43*(7), 1754–1761. doi: 10.4319/lo.1998.43.7.1754

Kharbush, J. J., Close, H. G., Mooy, B. A. S. V., Arnosti, C., Smittenberg, R. H., Moigne, F. A. C. L., ... Mohr, W. (2020). Particulate organic carbon deconstructed: Molecular

and chemical composition of particulate organic carbon in the ocean. *Frontiers in Marine Science*, *7*. doi: 10.3389/fmars.2020.00518

Kim, J.-H., van der Meer, J., Schouten, S., Helmke, P., Willmott, V., Sangiorgi, F., ... Damsté, J. S. S. (2010). New indices and calibrations derived from the distribution of crenarchaeal isoprenoid tetraether lipids: Implications for past sea surface temperature reconstructions. *Geochimica et Cosmochimica Acta*, *74*(16), 4639–4654. doi: 10.1016/j.gca.2010.05.027

King, T. M., Rosenheim, B. E., Post, A. L., Gabris, T., Burt, T., & Domack, E. W. (2018). Large-Scale Intrusion of Circumpolar Deep Water on Antarctic Margin Recorded by Stylasterid Corals. *Paleoceanography and Paleoclimatology*, *33*(11), 1306–1321. doi: 10.1029/2018pa003439

Kingslake, J., Scherer, R. P., Albrecht, T., Coenen, J., Powell, R. D., Reese, R., ... Whitehouse, P. L. (2018). Extensive retreat and re-advance of the West Antarctic Ice Sheet during the Holocene. *Nature*, *558*(7710), 430–434. doi: 10.1038/s41586-018-0208-x

Kirchman, D., K'nees, E., & Hodson, R. (1985). Leucine incorporation and its potential as a measure of protein synthesis by bacteria in natural aquatic systems. *Applied and Environmental Microbiology*, *49*(3), 599–607.

Klein III, C., & Orlando Jr, S. (1994). A spatial framework for water-quality management in the florida keys national marine sanctuary. *Bulletin of Marine Science*, *54*(3), 1036–1044.

Lea, D. W. (2003). Elemental and isotopic proxies of past ocean temperatures. In H. D. Holland & K. K. Turekian (Eds.), *Treatise on geochemistry* (Vol. 6, pp. 365–390). Elsevier Science. doi: 10.1016/b0-08-043751-6/06114-4

Lee, T. N., Leaman, K., Williams, E., Berger, T., & Atkinson, L. (1995). Florida current meanders and gyre formation in the southern straits of florida. *Journal of Geophysical Research*, *100*(C5), 8607. doi: 10.1029/94jc02795

Leichter, J. J., & Miller, S. L. (1999). Predicting high-frequency upwelling: Spatial and temporal patterns of temperature anomalies on a florida coral reef. *Continental Shelf Research*, *19*(7), 911–928. doi: 10.1016/s0278-4343(99)00004-7

Leutert, T. J., Auderset, A., Martínez-García, A., Modestou, S., & Meckler, A. N. (2020). Coupled southern ocean cooling and antarctic ice sheet expansion during the middle miocene. *Nature Geoscience*, *13*(9), 634–639. doi: 10.1038/s41561-020-0623-0

Libby, W. F. (1946). Atmospheric helium three and radiocarbon from cosmic radiation. *Physical Review*, *69*(11-12), 671–672. doi: 10.1103/physrev.69.671.2

Libby, W. F. (1955). Radiocarbon dating. *Chemistry in Britain*, *5*(12), 548–552.

Libby, W. F., Anderson, E. C., & Arnold, J. R. (1949). Age determination by radiocarbon content: World-wide assay of natural radiocarbon. *Science*, *109*(2827), 227–228. doi: 10.1126/science.109.2827.227

Licht, K. J. (2004). The Ross Sea's contribution to eustatic sea level during meltwater pulse 1A. *Sedimentary Geology*, *165*(3-4), 343–353. doi: 10.1016/j.sedgeo.2003.11.020

Linsley, B. K., Dunbar, R. B., Wellington, G. M., & Mucciarone, D. A. (1994). A coral-based reconstruction of Intertropical Convergence Zone variability over Central America since 1707. *Journal of Geophysical Research*, *99*(C5), 9977. doi: 10.1029/94jc00360

Lowry, D. P., Golledge, N. R., Bertler, N. A. N., Jones, R. S., & McKay, R. (2019). Deglacial grounding-line retreat in the Ross Embayment, Antarctica, controlled by ocean and atmosphere forcing. *Science Advances*, *5*(8), eaav8754. doi: 10.1126/sciadv.aav8754

Lund, D. C., & Curry, W. B. (2004). Late holocene variability in florida current surface density: Patterns and possible causes. *Paleoceanography*, *19*(4). doi: 10.1029/2004pa001008

Lynch-Stieglitz, J., Curry, W. B., & Lund, D. C. (2009). Florida straits density structure and transport over the last 8000 years. *Paleoceanography*, *24*(3). doi: 10.1029/2008pa001717

MacGregor, J. A., Anandakrishnan, S., Catania, G. A., & Winebrenner, D. P. (2011). The grounding zone of the Ross Ice Shelf, West Antarctica, from ice-penetrating radar. *Journal of Glaciology*, *57*(205), 917–928. doi: 10.3189/002214311798043780

Matsuoka, K., Hindmarsh, R. C., Moholdt, G., Bentley, M. J., Pritchard, H. D., Brown, J., ... Whitehouse, P. L. (2015). Antarctic ice rises and rumples: Their properties and significance for ice-sheet dynamics and evolution. *Earth-Science Reviews*, *150*, 724–745. doi: 10.1016/j.earscirev.2015.09.004

McCrea, J. M. (1950). On the Isotopic Chemistry of Carbonates and a Paleotemperature Scale. *The Journal of Chemical Physics*, *18*(6), 849–857. doi: 10.1063/1.1747785

McNichol, A., Quay, P., Gagnon, A., & Burton, J. (2010). Collection and measurement of carbon isotopes in seawater dic. *ICPO Publication Series*, *134*.

Meckler, A. N., Ziegler, M., Millán, M. I., Breitenbach, S. F. M., & Bernasconi, S. M. (2014). Long-term performance of the Kiel carbonate device with a new correction scheme for clumped isotope measurements. *Rapid Communications in Mass Spectrometry*, *28*(15), 1705–1715. doi: 10.1002/rcm.6949

Mercer, J. H. (1968). Glacial geology of the reedy glacier area, antarctica. *Geological Society of America Bulletin*, *79*(4), 471. doi: 10.1130/0016-7606(1968)79[471:ggotrg]2.0.co;2

Mercer, J. H. (1978). West Antarctic ice sheet and CO_2 greenhouse effect: a threat of disaster. *Nature*, *271*(5643), 321–325. doi: 10.1038/271321a0

Michaud, A. B., Dore, J. E., Achberger, A. M., Christner, B. C., Mitchell, A. C., Skidmore, M. L., ... Priscu, J. C. (2017). Microbial oxidation as a methane sink beneath the west antarctic ice sheet. *Nature Geoscience*, *10*(8), 582–586. doi: 10.1038/ngeo2992

Michaud, A. B., Skidmore, M. L., Mitchell, A. C., Vick-Majors, T. J., Barbante, C., Turetta, C., ... Priscu, J. C. (2016). Solute sources and geochemical processes in Subglacial Lake Whillans, West Antarctica. *Geology*, *44*(5), 347–350. doi: 10.1130/g37639.1

Michaud, A. B., Vick-Majors, T. J., Achberger, A. M., Skidmore, M. L., Christner, B. C., Tranter, M., & Priscu, J. C. (2020). Environmentally clean access to antarctic subglacial aquatic environments. *Antarctic Science*, *32*(5), 329–340. doi: 10.1017/s0954102020000231

Mikucki, J. A., Lee, P. A., Ghosh, D., Purcell, A. M., Mitchell, A. C., Mankoff, K. D., ... and, M. T. (2016). Subglacial lake whillans microbial biogeochemistry: a synthesis of current knowledge. *Philosophical Transactions of the Royal Society A: Mathematical, Physical and Engineering Sciences*, *374*(2059), 20140290. doi: 10.1098/rsta.2014.0290

Monson, K., & Hayes, J. (1982). Carbon isotopic fractionation in the biosynthesis of bacterial fatty acids. ozonolysis of unsaturated fatty acids as a means of determining the intramolecular distribution of carbon isotopes. *Geochimica et Cosmochimica Acta*, *46*(2), 139–149. doi: 10.1016/0016-7037(82)90241-1

Morlighem, M. (2019). *MEaSUREs BedMachine Antarctica, Version 1.* NASA National Snow and Ice Data Center DAAC. doi: 10.5067/C2GFER6PTOS4

Morlighem, M., Rignot, E., Binder, T., Blankenship, D., Drews, R., Eagles, G., ... Young, D. A. (2020). Deep glacial troughs and stabilizing ridges unveiled beneath the margins

of the Antarctic ice sheet. *Nature Geoscience*, *13*(2), 132–137. doi: 10.1038/s41561-019-0510-8

Mosola, A. B., & Anderson, J. B. (2006). Expansion and rapid retreat of the West Antarctic Ice Sheet in eastern Ross Sea: possible consequence of over-extended ice streams? *Quaternary Science Reviews*, *25*(17–18), 2177–2196. doi: 10.1016/j.quascirev.2005.12.013

Mouginot, J., Rignot, E., & Scheuchl, B. (2019). Continent-Wide, Interferometric SAR Phase, Mapping of Antarctic Ice Velocity. *Geophysical Research Letters*, *46*(16), 9710–9718. doi: 10.1029/2019gl083826

Müller, Kirst, G., Ruhland, G., von Storch, I., & Rosell-Melé, A. (1998). Calibration of the alkenone paleotemperature index $U_{37}^{K'}$ based on core-tops from the eastern South Atlantic and the global ocean (60°N–60°S). *Geochimica et Cosmochimica Acta*, *62*(10), 1757–1772. doi: 10.1016/s0016-7037(98)00097-0

Müller, I. A., Fernandez, A., Radke, J., van Dijk, J., Bowen, D., Schwieters, J., & Bernasconi, S. M. (2017). Carbonate clumped isotope analyses with the long-integration dual-inlet (LIDI) workflow: scratching at the lower sample weight boundaries. *Rapid Communications in Mass Spectrometry*, *31*(12), 1057–1066. doi: 10.1002/rcm.7878

Müller, I. A., Violay, M. E., Storck, J.-C., Fernandez, A., van Dijk, J., Madonna, C., & Bernasconi, S. M. (2017). Clumped isotope fractionation during phosphoric acid digestion of carbonates at 70 °C. *Chemical Geology*, *449*, 1–14. doi: 10.1016/j.chemgeo.2016.11.030

Muller, R. A., Alvarez, L. W., Holley, W. R., & Stephenson, E. J. (1977). Quarks with Unit Charge: A Search for Anomalous Hydrogen. *Science*, *196*(4289), 521–523. doi: 10.1126/science.196.4289.521

Muller, R. A., Stephenson, E. J., & Mast, T. S. (1978). Radioisotope Dating with an Accelerator: A Blind Measurement. *Science*, *201*(4353), 347–348. doi: 10.1126/science.201.4353.347

Murray, S. T., Arienzo, M. M., & Swart, P. K. (2016). Determining the δ_{47} acid fractionation in dolomites. *Geochimica et Cosmochimica Acta*, *174*, 42–53. doi: 10.1016/j.gca.2015.10.029

Nelson, D. E., Korteling, R. G., & Stott, W. R. (1977). Carbon-14: Direct detection at natural concentrations. *Science*, *198*(4316), 507–508. doi: 10.1126/science.198.4316.507

Nier, A. O. (1950). A Redetermination of the Relative Abundances of the Isotopes of Carbon, Nitrogen, Oxygen, Argon, and Potassium. *Physical Review*, *77*(6), 789–793. doi: 10.1103/physrev.77.789

Ohkouchi, N., Eglinton, T. I., & Hayes, J. M. (2003). Radiocarbon dating of individual fatty acids as a tool for refining antarctic margin sediment chronologies. *Radiocarbon*, *45*(1), 17–24. doi: 10.1017/s0033822200032355

Pandow, M., Mackay, C., & Wolfgang, R. (1960). The reaction of atomic carbon with oxygen: significance for the natural radio-carbon cycle. *Journal of Inorganic and Nuclear Chemistry*, *14*(3-4), 153–158. doi: 10.1016/0022-1902(60)80251-5

Passey, B. H., Levin, N. E., Cerling, T. E., Brown, F. H., & Eiler, J. M. (2010). High-temperature environments of human evolution in East Africa based on bond ordering in paleosol carbonates. *Proceedings of the National Academy of Sciences*, *107*(25), 11245–11249. doi: 10.1073/pnas.1001824107

Paxman, G. J., Jamieson, S. S., Hochmuth, K., Gohl, K., Bentley, M. J., Leitchenkov, G., & Ferraccioli, F. (2019). Reconstructions of antarctic topography since the eocene–oligocene boundary. *Palaeogeography, Palaeoclimatology, Palaeoecology*, *535*, 109346. doi: 10.1016/j.palaeo.2019.109346

Pearson, A., Eglinton, T. I., & McNichol, A. P. (2000). An organic tracer for surface ocean radiocarbon. *Paleoceanography*, *15*(5), 541–550. doi: 10.1029/1999pa000476

Pearson, A., Mcnichol, A. P., Schneider, R. J., Reden, K. F. V., & Zheng, Y. (1997). Microscale AMS 14c measurement at NOSAMS. *Radiocarbon*, *40*(1), 61–75. doi: 10.1017/s0033822200017902

Pearson, F., & Hanshaw, B. (1970). Sources of dissolved carbonate species in groundwater and their effects on carbon-14 dating. *Isotope hydrology*, *1970*, 271–285.

Pendergraft, M. A., & Rosenheim, B. E. (2014). Varying Relative Degradation Rates of Oil in Different Forms and Environments Revealed by Ramped Pyrolysis. *Environmental Science & Technology*, *48*(18), 10966–10974. doi: 10.1021/es501354c

Peters, L. E., Anandakrishnan, S., Alley, R. B., Winberry, J. P., Voigt, D. E., Smith, A. M., & Morse, D. L. (2006). Subglacial sediments as a control on the onset and location of two siple coast ice streams, west antarctica. *Journal of Geophysical Research*, *111*(B1). doi: 10.1029/2005jb003766

Petersen, S. V., Defliese, W. F., Saenger, C., Daëron, M., Huntington, K. W., John, C. M., ... Winkelstern, I. Z. (2019). Effects of improved ^{17}o correction on interlaboratory agreement in clumped isotope calibrations, estimates of mineral-specific offsets, and temperature dependence of acid digestion fractionation. *Geochemistry, Geophysics, Geosystems*, *20*(7), 3495–3519. doi: 10.1029/2018gc008127

Petersen, S. V., & Schrag, D. P. (2015). Antarctic ice growth before and after the eocene-oligocene transition: New estimates from clumped isotope paleothermometry. *Paleoceanography*, *30*(10), 1305–1317. doi: 10.1002/2014pa002769

Petersen, S. V., Tabor, C. R., Lohmann, K. C., Poulsen, C. J., Meyer, K. W., Carpenter, S. J., ... Sheldon, N. D. (2016). Temperature and salinity of the late cretaceous western interior seaway. *Geology*, *44*(11), 903–906. doi: 10.1130/g38311.1

Priscu, J., Kalin, J., Winans, J., Campbell, T., Siegfried, M., Skidmore, M., ... Vick-Majors, T. (in revision). Scientic access into mercer subglacial lake. *Annals of Glaciology*.

Priscu, J. C., Achberger, A. M., Cahoon, J. E., Christner, B. C., Edwards, R. L., Jones, W. L., ... Vick-Majors, T. J. (2013). A microbiologically clean strategy for access to the whillans ice stream subglacial environment. *Antarctic Science*, *25*(5), 637–647. doi: 10.1017/s0954102013000035

Priscu, J. C., & Christner, B. C. (2014). Earth's icy biosphere. In *Microbial diversity and bioprospecting* (pp. 130–145). ASM Press. doi: 10.1128/9781555817770.ch13

Priscu, J. C., Downes, M. T., Priscu, L. R., Palmisano, A. C., & Sullivan, C. W. (1990). Dynamics of ammonium oxidizer activity and nitrous oxide (N_2O) within and beneath Antarctic sea ice. *Marine Ecology Progress Series*, *62*, 37–46. doi: 10.3354/meps062037

Prothro, L. O., Majewski, W., Yokoyama, Y., Simkins, L. M., Anderson, J. B., Yamane, M., ... Ohkouchi, N. (2020). Timing and pathways of East Antarctic Ice Sheet retreat. *Quaternary Science Reviews*, *230*, 106166. doi: 10.1016/j.quascirev.2020.106166

Quinn, T. M., Crowley, T. J., Taylor, F. W., Henin, C., Joannot, P., & Join, Y. (1998). A multicentury stable isotope record from a New Caledonia coral: Interannual and decadal sea surface temperature variability in the southwest Pacific since 1657 A.D. *Paleoceanography*, *13*(4), 412–426. doi: 10.1029/98pa00401

Rack, F. R. (2016). Enabling clean access into Subglacial Lake Whillans: development and use of the WISSARD hot water drill system. *Philosophical Transactions of the Royal Society A: Mathematical, Physical and Engineering Sciences*, *374*(2059), 20140305. doi: 10.1098/rsta.2014.0305

Reimer, P. J., Austin, W. E. N., Bard, E., Bayliss, A., Blackwell, P. G., Ramsey, C. B., ... Talamo, S. (2020). The IntCal20 northern hemisphere radiocarbon age calibration curve (0–55 cal kBP). *Radiocarbon*, *62*(4), 725–757. doi: 10.1017/rdc.2020.41

Rignot, E., & Jacobs, S. S. (2002). Rapid Bottom Melting Widespread near Antarctic Ice Sheet Grounding Lines. *Science*, *296*(5575), 2020–2023. doi: 10.1126/science.1070942

Rignot, E., Mouginot, J., Morlighem, M., Seroussi, H., & Scheuchl, B. (2014). Widespread, rapid grounding line retreat of Pine Island, Thwaites, Smith, and Kohler glaciers, West Antarctica, from 1992 to 2011. *Geophysical Research Letters*, *41*(10), 3502–3509. doi: 10.1002/2014gl060140

Rignot, E., Mouginot, J., Scheuchl, B., van den Broeke, M., van Wessem, M. J., & Morlighem, M. (2019). Four decades of antarctic ice sheet mass balance from 1979–2017. *Proceedings of the National Academy of Sciences*, *116*(4), 1095–1103. doi: 10.1073/pnas.1812883116

Robin, G. d. Q., Swithinbank, C. W. M., & Smith, B. M. E. (1970). Radio echo exploration of the Antarctic ice sheet. *International Association of Scientific Hydrology Publication*, *86*, 97–115.

Rodríguez-Sanz, L., Bernasconi, S. M., Marino, G., Heslop, D., Müller, I. A., Fernandez, A., ... Rohling, E. J. (2017). Penultimate deglacial warming across the mediterranean sea revealed by clumped isotopes in foraminifera. *Scientific Reports*, *7*(1). doi: 10.1038/s41598-017-16528-6

Rooney, S., Blankenship, D., Alley, R., & Bentley, C. (1991). Seismic reflection profiling of a sediment-filled graben beneath ice stream b, west antarctica. In *International symposium on antarctic earth sciences. 5* (pp. 261–265).

Rooney, S. T., Blankenship, D. D., Alley, R. B., & Bentley, C. R. (1987). Till beneath ice stream b: 2. structure and continuity. *Journal of Geophysical Research*, *92*(B9), 8913. doi: 10.1029/jb092ib09p08913

Rosenheim, B. E., Day, M. B., Domack, E., Schrum, H., Benthien, A., & Hayes, J. M. (2008). Antarctic sediment chronology by programmed-temperature pyrolysis: Methodology and data treatment. *Geochemistry, Geophysics, Geosystems*, *9*(4), Q04005. doi: 10.1029/2007gc001816

Rosenheim, B. E., & Galy, V. (2012). Direct measurement of riverine particulate organic carbon age structure. *Geophysical Research Letters*, *39*(19), L19703. doi: 10.1029/2012gl052883

Rosenheim, B. E., Roe, K. M., Roberts, B. J., Kolker, A. S., Allison, M. A., & Johannesson, K. H. (2013). River discharge influences on particulate organic carbon age structure in the Mississippi/Atchafalaya River System. *Global Biogeochemical Cycles*, *27*(1), 154–166. doi: 10.1002/gbc.20018

Rosenheim, B. E., Santoro, J. A., Gunter, M., & Domack, E. W. (2013). Improving Antarctic Sediment ^{14}C Dating Using Ramped Pyrolysis: An Example from the Hugo Island Trough. *Radiocarbon*, *55*(01), 115–126. doi: 10.1017/s0033822200047846

Rosenheim, B. E., Tang, J., & Fernandez, A. (2013). Measurement of multiply substituted isotopologues ('clumped isotopes') of CO_2 using a 5 kV compact isotope ratio mass spectrometer: Performance, reference frame, and carbonate paleothermometry. *Rapid Communications in Mass Spectrometry*, *27*(16), 1847–1857. doi: 10.1002/rcm.6634

Sachs, J. P., Schneider, R. R., Eglinton, T. I., Freeman, K. H., Ganssen, G., McManus, J. F., & Oppo, D. W. (2000). Alkenones as paleoceanographic proxies. *Geochemistry, Geophysics, Geosystems*, *1*(11), 2000GC000059. doi: 10.1029/2000gc000059

Sackett, W. M. (1986). Organic carbon in sediments underlying the ross ice shelf. *Organic Geochemistry*, *9*(3), 135–137. doi: 10.1016/0146-6380(86)90103-8

Santrock, J., Studley, S. A., & Hayes, J. M. (1985). Isotopic analyses based on the mass spectra of carbon dioxide. *Analytical Chemistry*, *57*(7), 1444–1448. doi: 10.1021/ac00284a060

Scambos, T. A., Haran, T. M., Fahnestock, M. A., Painter, T. H., & Bohlander, J. (2007). MODIS-based Mosaic of Antarctica (MOA) data sets: Continent-wide surface morphology and snow grain size. *Remote Sensing of Environment*, *111*(2–3), 242–257. doi: 10.1016/j.rse.2006.12.020

Schauble, E. A., Ghosh, P., & Eiler, J. M. (2006). Preferential formation of ^{13}C–^{18}O bonds in carbonate minerals, estimated using first-principles lattice dynamics. *Geochimica et Cosmochimica Acta*, *70*(10), 2510–2529. doi: 10.1016/j.gca.2006.02.011

Schauer, A. J., Kelson, J., Saenger, C., & Huntington, K. W. (2016). Choice of ^{17}O correction affects clumped isotope (Δ_{47}) values of CO_2 measured with mass spectrometry. *Rapid Communications in Mass Spectrometry*, *30*(24), 2607–2616. doi: 10.1002/rcm.7743

Scherer, R. P. (1991). Quaternary and Tertiary microfossils from beneath Ice Stream B: Evidence for a dynamic West Antarctic Ice Sheet history. *Global and Planetary Change*, *4*(4), 395–412. doi: 10.1016/0921-8181(91)90005-h

Scherer, R. P. (1994). A new method for the determination of absolute abundance of diatoms and other silt-sized sedimentary particles. *Journal of Paleolimnology*, *12*(2), 171–179. doi: 10.1007/bf00678093

Scherer, R. P., Aldahan, A., Tulaczyk, S., Possnert, G., Engelhardt, H., & Kamb, B. (1998). Pleistocene Collapse of the West Antarctic Ice Sheet. *Science*, *281*(5373), 82–85. doi: 10.1126/science.281.5373.82

Schmid, T. W., & Bernasconi, S. M. (2010). An automated method for 'clumped-isotope' measurements on small carbonate samples. *Rapid Communications in Mass Spectrometry*, *24*(14), 1955–1963. doi: 10.1002/rcm.4598

Schmidt, M. W., Weinlein, W. A., Marcantonio, F., & Lynch-Stieglitz, J. (2012). Solar forcing of florida straits surface salinity during the early holocene. *Paleoceanography*, *27*(3). doi: 10.1029/2012pa002284

Schmitz, W. J., & McCartney, M. S. (1993). On the north atlantic circulation. *Reviews of Geophysics*, *31*(1), 29–49. doi: 10.1029/92rg02583

Schmitz, W. J., & Richardson, P. L. (1991). On the sources of the florida current. *Deep Sea Research Part A. Oceanographic Research Papers*, *38*, S379–S409. doi: 10.1016/s0198-0149(12)80018-5

Scholander, P., Dansgaard, W., Nutt, D., de Vries, H., Coachman, L., & Hemmingsen, E. (1962). *Radio-carbon age and oxygen-18 content of Greenland icebergs*. Reitzel.

Scholander, P. F., Kanwisher, J. W., & Nutt, D. C. (1956). Gases in icebergs. *Science*, *123*(3186), 104–105. doi: 10.1126/science.123.3186.104

Schoof, C. (2007). Ice sheet grounding line dynamics: Steady states, stability, and hysteresis. *Journal of Geophysical Research*, *112*(F3), F03S28. doi: 10.1029/2006jf000664

Schouten, S., Hopmans, E. C., Schefuß, E., & Damsté, J. S. S. (2002). Distributional variations in marine crenarchaeotal membrane lipids: a new tool for reconstructing ancient sea water temperatures? *Earth and Planetary Science Letters*, *204*(1-2), 265–274. doi: 10.1016/s0012-821x(02)00979-2

Schrag, D. P. (1999). Rapid analysis of high-precision sr/ca ratios in corals and other marine carbonates. *Paleoceanography*, *14*(2), 97–102. doi: 10.1029/1998pa900025

Schrag, D. P., Hampt, G., & Murray, D. W. (1996). Pore fluid constraints on the temperature and oxygen isotopic composition of the glacial ocean. *Science*, *272*(5270), 1930–1932. doi: 10.1126/science.272.5270.1930

Schreiner, K. M., Bianchi, T. S., & Rosenheim, B. E. (2014). Evidence for permafrost thaw and transport from an Alaskan North Slope watershed. *Geophysical Research Letters*, *41*(9), 3117–3126. doi: 10.1002/2014gl059514

Siegert, M. J., Carter, S., Tabacco, I., Popov, S., & Blankenship, D. D. (2005). A revised inventory of antarctic subglacial lakes. *Antarctic Science*, *17*(3), 453–460. doi: 10.1017/s0954102005002889

Siegert, M. J., Ross, N., & Brocq, A. M. L. (2016). Recent advances in understanding antarctic subglacial lakes and hydrology. *Philosophical Transactions of the Royal Society A: Mathematical, Physical and Engineering Sciences*, *374*(2059), 20140306. doi: 10.1098/rsta.2014.0306

Siegfried, M. R., & Fricker, H. A. (2018). Thirteen years of subglacial lake activity in Antarctica from multi-mission satellite altimetry. *Annals of Glaciology*, *59*(76pt1), 42–55. doi: 10.1017/aog.2017.36

Siegfried, M. R., & Fricker, H. A. (in revision). Illumination active subglacial lake processes with ICESat-2 laser altimetry. *Geophysical Research Letters*.

Siegfried, M. R., Fricker, H. A., Carter, S. P., & Tulaczyk, S. (2016). Episodic ice velocity fluctuations triggered by a subglacial flood in west antarctica. *Geophysical Research Letters*, *43*(6), 2640–2648. doi: 10.1002/2016gl067758

Simkins, L. M., Greenwood, S. L., & Anderson, J. B. (2018). Diagnosing ice sheet grounding line stability from landform morphology. *The Cryosphere*, *12*(8), 2707–2726. doi: 10.5194/tc-12-2707-2018

Skidmore, M. (2011). Microbial communities in antarctic subglacial aquatic environments. *GMS*, *192*, 61–81.

Smith, B., Fricker, H. A., Gardner, A. S., Medley, B., Nilsson, J., Paolo, F. S., ... Zwally, H. J. (2020). Pervasive ice sheet mass loss reflects competing ocean and atmosphere processes. *Science*, *368*(6496), 1239–1242. doi: 10.1126/science.aaz5845

Spector, P., Stone, J., Cowdery, S. G., Hall, B., Conway, H., & Bromley, G. (2017). Rapid early-Holocene deglaciation in the Ross Sea, Antarctica. *Geophysical Research Letters*, *44*(15), 7817–7825. doi: 10.1002/2017gl074216

Stearns, L. A., Smith, B. E., & Hamilton, G. S. (2008). Increased flow speed on a large east antarctic outlet glacier caused by subglacial floods. *Nature Geoscience*, *1*(12), 827–831. doi: 10.1038/ngeo356

Steier, P., Dellinger, F., Kutschera, W., Priller, A., Rom, W., & Wild, E. M. (2004). Pushing the Precision Limit of ^{14}C AMS. *Radiocarbon*, *46*(1), 5–16. doi: 10.1017/s0033822200039291

Steig, E. J., & Neff, P. D. (2018). The prescience of paleoclimatology and the future of the antarctic ice sheet. *Nature Communications*, *9*(1). doi: 10.1038/s41467-018-05001-1

Strickland, J. D. H., & Parsons, T. R. (1972). *A practical handbook of seawater analysis*. Fisheries Research Board of Canada.

Stuiver, M., Denton, G. H., Hughes, T. J., & Fastook, J. L. (1981). History of the marine ice sheets in West Antarctica during the last glaciation: A working hypothesis. In G. H. Denton & T. J. Hughes (Eds.), *The last great ice sheets* (pp. 319–439). New York: Wiley-Interscience.

Stuiver, M., & Polach, H. A. (1977). Discussion Reporting of ^{14}C Data. *Radiocarbon*, *19*(3), 355–363. doi: 10.1017/s0033822200003672

Subt, C., Fangman, K. A., Wellner, J. S., & Rosenheim, B. E. (2016). Sediment chronology in Antarctic deglacial sediments: Reconciling organic carbon ^{14}C ages to carbonate ^{14}C ages using Ramped PyrOx. *The Holocene*, *26*(2), 265–273. doi: 10.1177/0959683615608688

Subt, C., Yoon, H. I., Yoo, K. C., Lee, J. I., Leventer, A., Domack, E. W., & Rosenheim, B. E. (2017). Sub-ice shelf sediment geochronology utilizing novel radiocarbon methodology for highly detrital sediments. *Geochemistry, Geophysics, Geosystems*, *18*(4), 1404–1418. doi: 10.1002/2016gc006578

Synal, H.-A., Stocker, M., & Suter, M. (2007). MICADAS: A new compact radiocarbon AMS system. *Nuclear Instruments and Methods in Physics Research Section B: Beam Interactions with Materials and Atoms*, *259*(1), 7–13. doi: 10.1016/j.nimb.2007.01.138

Tang, J., Dietzel, M., Fernandez, A., Tripati, A. K., & Rosenheim, B. E. (2014). Evaluation of kinetic effects on clumped isotope fractionation (Δ_{47}) during inorganic calcite precipitation. *Geochimica et Cosmochimica Acta*, *134*, 120–136. doi: 10.1016/j.gca.2014.03.005

Teece, M. A., Fogel, M. L., Dollhopf, M. E., & Nealson, K. H. (1999). Isotopic fractionation associated with biosynthesis of fatty acids by a marine bacterium under oxic and anoxic conditions. *Organic Geochemistry*, *30*(12), 1571–1579. doi: 10.1016/s0146-6380(99)00108-4

Tierney, J. E., Poulsen, C. J., Montañez, I. P., Bhattacharya, T., Feng, R., Ford, H. L., ... Zhang, Y. G. (2020). Past climates inform our future. *Science*, *370*(6517), eaay3701. doi: 10.1126/science.aay3701

Tinto, K. J., Padman, L., Siddoway, C. S., Springer, S. R., Fricker, H. A., Das, I., ... Bell, R. E. (2019). Ross Ice Shelf response to climate driven by the tectonic imprint on

seafloor bathymetry. *Nature Geoscience*, *12*(6), 441–449. doi: 10.1038/s41561-019-0370-2

Toth, L. T., Cheng, H., Edwards, R. L., Ashe, E., & Richey, J. N. (2017). Millennial-scale variability in the local radiocarbon reservoir age of south florida during the holocene. *Quaternary Geochronology*, *42*, 130–143. doi: 10.1016/j.quageo.2017.07.005

Toth, L. T., Kuffner, I. B., Stathakopoulos, A., & Shinn, E. A. (2018). A 3,000-year lag between the geological and ecological shutdown of florida's coral reefs. *Global Change Biology*, *24*(11), 5471–5483. doi: 10.1111/gcb.14389

Tulaczyk, S., Kamb, B., Scherer, R. P., & Engelhardt, H. F. (1998). Sedimentary processes at the base of a west antarctic ice stream: constraints from textural and compositional properties of subglacial debris. *Journal of Sedimentary Research*, *68*(3), 487–496. doi: 10.2110/jsr.68.487

Tulaczyk, S., Mikucki, J. A., Siegfried, M. R., Priscu, J. C., Barcheck, C. G., Beem, L. H., ... the WISSARD Science Team (2014). WISSARD at Subglacial Lake Whillans, West Antarctica: scientific operations and initial observations. *Annals of Glaciology*, *55*(65), 51–58. doi: 10.3189/2014aog65a009

Urey, H. C. (1947). The thermodynamic properties of isotopic substances. *Journal of the Chemical Society*, 562–581. doi: 10.1039/jr9470000562

Urey, H. C., Lowenstam, H. A., Epstein, S., & McKinney, C. R. (1951). Measurement of Paleotemperatures and Temperatures of the Upper Cretaceous of England, Denmark, and the Southeastern United States. *Geological Society of America Bulletin*, *62*(4), 399. doi: 10.1130/0016-7606(1951)62[399:mopato]2.0.co;2

Venturelli, R. A., & Rosenheim, B. E. (2018). Compositional and beam-size-dependent effects on pressure baseline in clumped isotope mass spectrometry. *Rapid Communications in Mass Spectrometry*, *33*(1), 140–148. doi: 10.1002/rcm.8303

Venturelli, R. A., Siegfried, M. R., Roush, K. A., Li, W., Burnett, J., Zook, R., ... Rosenheim, B. E. (2020). Mid-Holocene Grounding Line Retreat and Readvance at Whillans Ice Stream, West Antarctica. *Geophysical Research Letters*, *47*(15). doi: 10.1029/2020gl088476

Vick-Majors, T. J., Michaud, A. B., Skidmore, M. L., Turetta, C., Barbante, C., Christner, B. C., ... Priscu, J. C. (2020). Biogeochemical Connectivity Between Freshwater Ecosystems beneath the West Antarctic Ice Sheet and the Sub-Ice Marine Environment. *Global Biogeochemical Cycles*, *34*(3). doi: 10.1029/2019gb006446

Vick-Majors, T. J., Mitchell, A. C., Achberger, A. M., Christner, B. C., Dore, J. E., Michaud, A. B., ... and, J. C. P. (2016). Physiological Ecology of Microorganisms in Subglacial Lake Whillans. *Frontiers in Microbiology*, *7*. doi: 10.3389/fmicb.2016.01705

Villinski, J. C., Dunbar, R. B., & Mucciarone, D. A. (2000). Carbon 13/Carbon 12 ratios of sedimentary organic matter from the Ross Sea, Antarctica: A record of phytoplankton bloom dynamics. *Journal of Geophysical Research: Oceans*, *105*(C6), 14163–14172. doi: 10.1029/1999jc000309

Volkman, J. K. (2000). Ecological and environmental factors affecting alkenone distributions in seawater and sediments. *Geochemistry, Geophysics, Geosystems*, *1*(9), 2000GC000061. doi: 10.1029/2000gc000061

Walker, B. D., & Xu, X. (2019). An improved method for the sealed-tube zinc graphitization of microgram carbon samples and ^{14}c AMS measurement. *Nuclear Instruments and Methods in Physics Research Section B: Beam Interactions with Materials and Atoms*, *438*, 58–65. doi: 10.1016/j.nimb.2018.08.004

Wang, K. J., Huang, Y., Majaneva, M., Belt, S. T., Liao, S., Novak, J., ... Cabedo-Sanz, P. (2021). Group 2i isochrysidales produce characteristic alkenones reflecting sea ice distribution. *Nature Communications*, *12*(1). doi: 10.1038/s41467-020-20187-z

Wang, Z., Schauble, E. A., & Eiler, J. M. (2004). Equilibrium thermodynamics of multiply substituted isotopologues of molecular gases. *Geochimica et Cosmochimica Acta*, *68*(23), 4779–4797. doi: 10.1016/j.gca.2004.05.039

Warnock, J. P., & Scherer, R. P. (2014). A revised method for determining the absolute abundance of diatoms. *Journal of Paleolimnology*, *53*(1), 157–163. doi: 10.1007/s10933-014-9808-0

Weertman, J. (1974). Stability of the Junction of an Ice Sheet and an Ice Shelf. *Journal of Glaciology*, *13*(67), 3–11. doi: 10.3189/s0022143000023327

Westerhold, T., Marwan, N., Drury, A. J., Liebrand, D., Agnini, C., Anagnostou, E., ... Zachos, J. C. (2020). An astronomically dated record of earth's climate and its predictability over the last 66 million years. *Science*, *369*(6509), 1383–1387. doi: 10.1126/science.aba6853

Whitehouse, P. L., Gomez, N., King, M. A., & Wiens, D. A. (2019). Solid Earth change and the evolution of the Antarctic Ice Sheet. *Nature Communications*, *10*, 503. doi: 10.1038/s41467-018-08068-y

Williams, E. K., Rosenheim, B. E., Allison, M., McNichol, A. P., & Xu, L. (2015). Quantification of refractory organic material in Amazon mudbanks of the French Guiana Coast. *Marine Geology*, *363*, 93–101. doi: 10.1016/j.margeo.2015.02.009

Wilson, D. S., Jamieson, S. S., Barrett, P. J., Leitchenkov, G., Gohl, K., & Larter, R. D. (2012). Antarctic topography at the Eocene–Oligocene boundary. *Palaeogeography, Palaeoclimatology, Palaeoecology*, *335-336*, 24–34. doi: 10.1016/j.palaeo.2011.05.028

Winkelstern, I. Z., Rowe, M. P., Lohmann, K. C., Defliese, W. F., Petersen, S. V., & Brewer, A. W. (2017). Meltwater pulse recorded in last interglacial mollusk shells from bermuda. *Paleoceanography*, *32*(2), 132–145. doi: 10.1002/2016pa003014

Xu, X., Trumbore, S. E., Zheng, S., Southon, J. R., McDuffee, K. E., Luttgen, M., & Liu, J. C. (2007). Modifying a sealed tube zinc reduction method for preparation of AMS graphite targets: Reducing background and attaining high precision. *Nuclear Instruments and Methods in Physics Research Section B: Beam Interactions with Materials and Atoms*, *259*(1), 320–329. doi: 10.1016/j.nimb.2007.01.175

Yoshida, N., Vasilev, M., Ghosh, P., Abe, O., Yamada, K., & Morimoto, M. (2012). Precision and long-term stability of clumped-isotope analysis of CO_2 using a small-sector isotope ratio mass spectrometer. *Rapid Communications in Mass Spectrometry*, *27*(1), 207–215. doi: 10.1002/rcm.6431

Zaarur, S., Affek, H. P., & Brandon, M. T. (2013). A revised calibration of the clumped isotope thermometer. *Earth and Planetary Science Letters*, *382*, 47–57. doi: 10.1016/j.epsl.2013.07.026

Zermeño, P., Kurdyla, D. K., Buchholz, B. A., Heller, S. J., Kashgarian, M., & Frantz, B. R. (2004). Prevention and removal of elevated radiocarbon contamination in the LLNL/CAMS natural radiocarbon sample preparation laboratory. *Nuclear Instruments and Methods in Physics Research Section B: Beam Interactions with Materials and Atoms*, *223-224*, 293–297. doi: 10.1016/j.nimb.2004.04.058

Zhang, C. L., Li, Y., Ye, Q., Fong, J., Peacock, A. D., Blunt, E., ... White, D. C. (2003). Carbon isotope signatures of fatty acids in geobacter metallireducens and shewanella algae. *Chemical Geology*, *195*(1-4), 17–28. doi: 10.1016/s0009-2541(02)00386-8

Zhang, X., Bianchi, T. S., Cui, X., Rosenheim, B. E., Ping, C.-L., Hanna, A. J. M., ... Allison, M. A. (2017). Permafrost Organic Carbon Mobilization From the Watershed to

the Colville River Delta: Evidence From ^{14}C Ramped Pyrolysis and Lignin Biomarkers. *Geophysical Research Letters*, *44*(22), 11,491–11,500. doi: 10.1002/2017gl075543

Zhao, X.-L., Crann, C. A., Murseli, S., St-Jean, G., Kieser, W. E., Wilk, M., ... Clark, I. D. (2019). A preliminary ion source background study at lalonde AMS. *Radiocarbon*, *61*(4), 1091–1106. doi: 10.1017/rdc.2019.58

Zhou, W., Wu, S., Lange, T. E., Lu, X., Cheng, P., Xiong, X., ... Zhao, W. (2012). High-Level ^{14}C Contamination and Recovery at Xi'an AMS Center. *Radiocarbon*, *54*(2), 187–193. doi: 10.2458/azu_js_rc.v54i2.16045

Appendix A: Proof of Copyright Permissions

Chapter 2

The following is taken directly from the Wiley Publishing webpage (https://www.wiley.com/en-us/permissions/Author-of-Work) detailing permissions for:

Venturelli, R. A., & Rosenheim, B. E. (2019). Compositional and beam-size-dependent effects on pressure baseline in clumped isotope mass spectrometry. *Rapid Communications in Mass Spectrometry*, 33(1), 140-148. (DOI: 10.1002/rcm.8303)

"If you are the author of a published Wiley article, you have the right to reuse the full text of your published article as part of your thesis or dissertation. In this situation, you do not need to request permission from Wiley for this use."

Chapter 4

The following is taken directly from the AGU, Geophysical Research Letters webpage (https://agupubs.onlinelibrary.wiley.com/hub/journal/19448007/about/permissions) detailing permissions for:

Venturelli, R. A., Siegfried, Roush, K.A., Li, W., Burnett, J., Zook, R., Fricker, H.A., Priscu, J.C., Leventer, A. and Rosenheim, B.E. (2020). Mid-Holocene grounding line retreat and readvance at Whillans Ice Stream, West Antarctica. *Geophysical Research Letters*, 47(15), e2020GL088476. (DOI: 10.1029/2020GL088476)

"If you wish to reuse your own article (or an amended version of it) in a new publication of which you are the author, editor or co-editor, prior permission is not required (with the usual acknowledgements)."

Appendix B: Florida Keys Reef Tract Coral Clumped Isotopes

Overview

The Florida Keys Reef Tract (FKRT) is the third largest coral reef system in the world, forming the northern structural boundary of the Straits of Florida, through which the Florida Current flows parallel to the FKRT linking salinity-driven circulation of the Caribbean Sea to the origin of the western boundary Gulf Stream, facilitating a link between the tropical and high-latitude Atlantic Ocean (Hall & Bryden, 1982; Schmitz & Richardson, 1991; Schmitz & McCartney, 1993; Lee et al., 1995; Lund & Curry, 2004; Lynch-Stieglitz et al., 2009; Schmidt et al., 2012; Toth et al., 2017). In contrast to western Atlantic reefs, which demonstrate continuous accretion throughout the Holocene until recent interruption due to anthropogenic disturbance, FKRT accretion began to significantly decline 6 ky B.P. until reaching geological senescence 3 ky B.P. (Toth et al., 2018). Regional paleoceanographic records from combined ^{14}C and U-series measurements of Holocene-aged corals from the FKRT indicate that significant nearshore hydrographic variability occurred in this region throughout the Holocene (Toth et al., 2017). The cause for this variability is largely unknown. Thorough reconstruction of hydrographic variability in this region is integral to determining the extent to which Atlantic Ocean surface circulation responds to atmospheric and oceanic forcing on timescales beyond the instrumental record.

Decoupling local- versus regional- scale controls on south Florida oceanographic and hydrographic variability is imperative for our understanding of long-term controls on the past variability of the Florida Current and its impact on larger scale climatic oscillations. Local

scale variability has been attributed to the influence of upwelling (Klein III & Orlando Jr, 1994; Lee et al., 1995; Leichter & Miller, 1999) or terrestrial input from the Florida platform (Pearson & Hanshaw, 1970; Chanton et al., 2003). Terrestrial inputs include meteoric water runoff, both from the surface and subsurface (groundwater), which would have influence on the apparent age of nearshore water masses. Florida's subterranean aquifers and Pleistocene carbonate platform are significantly older than meteoric water flowing through them. Dissolution of ^{14}C-depleted carbonate results in groundwater with a falsely old age, which may be imparted onto hermatypic corals growing in this region.

In order to isolate the mechanisms and magnitude of hydrographic variability in the Straits of Florida throughout the Holocene, we must develop proxies capable of deconvolving local- from regional-scale change utilizing available paleoclimate archives for targeted intervals. Shallow water corals growing along the FKRT provide an ideal archive of hydrographic variability influencing the Atlantic Ocean throughout the Holocene, as they record both terrestrial input from the Florida Platform and oceanographic change within the Straits of Florida. However, insufficient development of paleoclimate proxies for the genera of coral growing along the FKRT hinder our ability deconvolve local upwelling and terrestrial influence from regional-scale circulation in this location. Therefore, there is a need for both the refinement of geochemical proxies utilizing modern materials from this study area, as well as the application of these proxies throughout the Holocene.

Carbonate clumped isotope thermometry, a novel tool for reconstructing temperatures independent of calcifying fluid composition, has recently gained traction for the potential of deconvolving paleotemperature and past seawater isotopic composition ($\delta^{18}O_w$) within a single measurement (Eiler, 2011). Clumped isotope measurements (Δ_{47}) in bulk corals (Ghosh et al., 2006) demonstrate agreement with inorganic Δ_{47} calibrations, and *Porites* corals demonstrate Δ_{47} values that fall within 1.5°C of their growth temperature. It has been suggested that some shallow water corals (*Porites Siderastrea, Astrangia* and *Caryophyllia*) demonstrate enriched Δ_{47} signatures due to vital effects correlated with growth rate, how-

ever Δ_{47} signatures show a clear temperature dependence, lending support to the further development of this proxy for other species of shallow water corals.

Here I present preliminary stable isotope work(Δ_{47}, δ^{13}C, δ^{18}O) utilizing bulk samples (averaging 5 growth seasons) of Holocene-aged shallow water corals (*Acropora, Orbicella, Diploria*) chosen based on age (^{14}C) and location spanning the spatial range (upper, middle, lower Keys, and open ocean) and temporal range (7.5 ky B.P. to 4.5 ky B.P.) in excess of those affected by anomalous radiocarbon reservoir ages (Toth et al., 2017).

Methods

All stable isotope work (Δ_{47}, δ^{13}C, δ^{18}O) was conducted in the Stable Isotope Laboratory at the University of Michigan, wherein each sample was replicated three times. Samples (4 mg) were reacted individually with 105 wt% H_3PO_4 for 15 minutes to extract CO_2 on the offline sample preparation line using methods outlined in (Defliese et al., 2015), in which residual water as well as hydro/halo-carbons were removed using cryogenic separation and chilled Porapak, respectively. The purified samples were transferred to a Thermo Scientific MAT 253 isotope ratio mass spectrometer (IRMS) where abundances of mass 44-49 isotopologues were measured. Analyses of unknowns were bolstered with analyses of heated and equilibrated gases to construct a reference frame as described in Dennis et al. (2011), internal carbonate standards to verify reference frame stability, and external carbonate standards as recommended by Bernasconi et al. (2018). For Sr/Ca analyses, 200 μg of the homogenized coral powders were acidified with 2% nitric acid to achieve target concentrations of 20 ppm Ca. Acidified samples were analyzed on the PerkinElmer 7300 DV inductively couple optical emission spectrometer (ICP-OES) at the U.S. Geological Survey St. Petersburg Coastal and Marine Science Center. The internal gravimetric standard methods described in Schrag (1999) were used to correct Sr/Ca data for instrumental drift.

Preliminary Results

Clumped isotope derived temperatures fall within realistic growth temperatures for shallow water corals growing along the FKRT and exhibit temporal variability in $\delta^{18}O_w$ that can be correlated with variations in local radiocarbon reservoir age (Toth et al., 2017). Data from *Orbicella* samples, in particular, demonstrate agreement between Δ_{47} and Sr/Ca derived paleotemperatures and $\delta^{18}O_w$ values (Figure B.1).

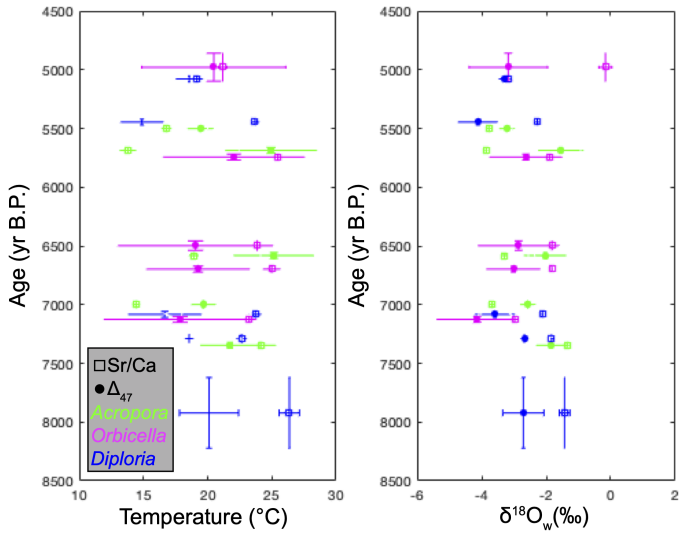

Figure B.1: Preliminary clumped isotope and Sr/Ca derived paleotemperatures and $\delta^{18}O_w$ values from FKRT corals. Each point represents an average of three replicates for Δ_{47} measurements and five replicates for Sr/Ca measurements. All error bars represent 2σ uncertainty.

Data

Table B.1: Sample information for all FKRT corals analyzed. Listed ages were previously published by Toth et al. (2017)

Sample ID	Lat.	Long.	Subregion	Age (yrs B.P.)	2σ	genus
LK-LK-5-0	25.0	-80.4	Lower Keys	7080	25	Diploria
MK-SR-1-15	24.6	-81.1	Middle Keys	7290	35	Diploria
DT-LB-1-16.5	24.6	-82.9	Dry Tortugas	5080	25	Diploria
UK-GR-3-20	25.1	-80.3	Upper Keys	7920	300	Diploria
LK-5K-N5-0	24.5	-81.9	Lower Keys	5450	25	Diploria
UK-GR-4-10	25.1	-80.3	Upper Keys	4980	120	Orbicella
DT-GB-6-27	24.6	-82.9	Dry Tortugas	6500	40	Orbicella
UK-CF-7-25	25.2	-80.2	Upper Keys	5740	25	Orbicella
LK-WS-3-21	25.1	-80.3	Upper Keys	7130	25	Orbicella
LK-LK-18-2	24.5	-81.4	Lower Keys	6700	25	Orbicella
MK-SR-3-3	24.6	-81.1	Middle Keys	5690	25	Acropora
UK-CF-4-5	25.2	-80.2	Upper Keys	6580	25	Acropora
MK-TN-1-6	24.7	-80.8	Middle Keys	7000	30	Acropora
MK-TN-2-1	24.7	-80.8	Middle Keys	7350	25	Acropora
LK-WS-3-5	24.5	-81.7	Lower Keys	5500	25	Acropora

Table B.2: Raw stable isotope data for FKRT corals.

Sample Name	Date Analyzed	δ^{13}C(‰)	2σ	δ^{18}O(‰)	2σ	δ^{45}(‰)	δ^{46}(‰)	δ^{47}(‰)	δ^{48}(‰)	δ^{49}(‰)	Δ_{47}(‰)
UK-GR-4-11	7/25/18	0.23	0.70	35.15	2.50	3.68	0.18	3.62	-2.29	23.58	-0.35
UK-GR-4-11	7/29/18	0.36	0.60	35.83	2.00	3.83	0.83	4.41	-0.39	20.47	-0.36
UK-GR-4-11	8/2/18	0.29	0.60	35.69	2.80	3.76	0.70	4.25	0.09	-1.57	-0.32
LK-LK-5-0	7/25/18	1.23	0.80	35.88	1.40	4.64	0.88	5.34	-0.54	23.04	-0.32
LK-LK-5-0	7/30/18	1.35	0.60	35.99	2.10	4.76	0.98	5.58	4.95	18.91	-0.31
LK-LK-5-0	8/2/18	1.31	0.60	35.91	2.00	4.73	0.91	5.48	1.70	16.05	-0.29
MK-SR-1-15	7/26/18	0.78	0.60	36.33	1.40	4.24	1.31	5.36	0.53	20.89	-0.31
MK-SR-1-15	7/29/18	0.99	0.70	36.47	1.70	4.44	1.44	5.70	1.50	20.21	-0.30
MK-SR-1-15	8/3/18	0.82	0.60	36.54	2.60	4.28	1.51	5.60	3.11	18.60	-0.31
DT-LB-1-16.5	7/26/18	2.39	0.60	35.64	1.60	5.73	0.65	6.26	-1.14	22.00	-0.30
DT-LB-1-16.5	7/30/18	2.59	0.60	35.79	1.70	5.92	0.79	6.60	-0.30	24.70	-0.29
DT-LB-1-16.5	8/3/18	2.58	0.70	35.94	2.40	5.92	0.94	6.75	2.18	13.17	-0.28
MK-SR-3-3	7/30/18	0.97	0.60	36.33	2.00	4.42	1.32	5.55	-0.01	26.21	-0.31
MK-SR-3-3	8/5/18	0.83	0.70	36.24	2.90	4.28	1.22	5.30	1.07	16.14	-0.32
MK-SR-3-3	8/6/18	0.85	0.70	36.26	1.40	4.30	1.24	5.36	2.52	20.22	-0.30
DT-GB-6-27	7/27/18	-0.09	0.70	36.11	1.70	3.42	1.10	4.27	-0.11	22.96	-0.34
DT-GB-6-27	7/30/18	0.00	0.60	36.27	1.70	3.51	1.25	4.55	3.59	20.49	-0.30
DT-GB-6-27	8/4/18	-0.05	0.60	36.24	2.90	3.45	1.22	4.44	2.30	17.37	-0.33
UK-CF-4-5	7/28/18	-0.68	0.70	35.77	2.60	2.85	0.77	3.34	-0.52	19.59	-0.36
UK-CF-4-5	7/31/18	-0.64	0.60	35.61	2.00	2.89	0.62	3.21	-1.00	21.32	-0.37
UK-CF-4-5	8/5/18	-0.49	0.70	35.80	2.90	3.03	0.79	3.55	0.84	18.04	-0.36
UK-CF-7-25	7/27/18	-0.08	0.70	35.80	2.00	3.42	0.80	3.98	-0.84	23.30	-0.33
UK-CF-7-25	7/31/18	-0.22	0.60	35.74	1.90	3.28	0.74	3.77	-0.74	20.41	-0.35
UK-CF-7-25	8/4/18	-0.17	0.60	35.81	3.00	3.34	0.81	3.89	0.85	15.11	-0.35
MK-TN-1-6	7/27/18	0.16	0.70	36.41	1.90	3.66	1.39	4.82	0.46	23.01	-0.33
MK-TN-1-6	7/31/18	0.11	0.70	36.20	2.50	3.61	1.18	4.55	0.52	19.46	-0.33
MK-TN-1-6	8/4/18	0.15	0.60	36.34	2.90	3.65	1.32	4.77	1.56	16.79	-0.30
UK-GR-3-20	7/27/18	0.04	0.50	36.14	1.90	3.54	1.13	4.42	-0.28	23.41	-0.34
UK-GR-3-20	7/31/18	0.06	0.60	35.77	1.80	3.55	0.77	4.08	-0.28	18.41	-0.33
UK-GR-3-20	8/4/18	0.39	0.70	36.35	2.80	3.88	1.33	5.01	1.23	17.36	-0.30
LK-WS-3-21	7/28/18	-0.42	0.70	35.18	1.60	3.08	0.20	3.02	-1.88	21.32	-0.35
LK-WS-3-21	7/31/18	-0.49	0.70	35.06	1.80	3.01	0.08	2.84	-1.62	18.27	-0.34
LK-WS-3-21	8/5/18	-0.44	0.60	35.16	2.70	3.06	0.19	2.97	-1.52	14.55	-0.36
MK-TN-2-1	7/28/18	0.86	0.70	36.77	1.90	4.33	1.74	5.87	1.70	20.50	-0.31
MK-TN-2-1	8/1/18	0.82	0.60	36.60	2.60	4.29	1.57	5.67	2.54	20.05	-0.30
MK-TN-2-1	8/5/18	0.80	0.70	36.52	3.70	4.27	1.49	5.57	2.05	16.31	-0.30
LK-WS-3-5	7/28/18	-1.04	0.60	35.73	1.70	2.52	0.73	2.95	-0.60	19.65	-0.36
LK-WS-3-5	8/1/18	-0.84	0.70	35.78	2.80	2.70	0.78	3.18	-0.15	19.93	-0.37
LK-WS-3-5	8/5/18	-1.04	0.70	35.58	3.20	2.51	0.59	2.82	-0.76	16.29	-0.34
LK-5K-N5-0	7/29/18	1.53	0.70	35.80	1.60	4.93	0.80	5.58	1.80	15.71	-0.29
LK-5K-N5-0	8/1/18	1.42	0.60	35.63	3.20	4.82	0.63	5.30	11.37	14.27	-0.30
LK-5K-N5-0	8/6/18	1.54	0.60	35.84	2.60	4.94	0.84	5.66	26.66	9.95	-0.27
LK-LK-18-2	7/29/18	-0.01	0.70	35.99	1.40	3.49	0.98	4.25	1.75	17.19	-0.32
LK-LK-18-2	8/2/18	-0.06	0.50	35.96	1.90	3.44	0.96	4.14	1.86	15.85	-0.35
LK-LK-18-2	8/6/18	0.04	0.60	35.94	2.30	3.53	0.93	4.24	5.35	15.08	-0.32

Table B.3: Clumped isotope data for FKRT corals. Clumped isotope measurements were calibrated to temperature using the calibration presented in Dennis et al. (2011). $\delta^{18}O_w$were calculated using clumped isotope derived temperatures and the δ^{18}O–temperature equilibrium relationship of Kim et al. (2007).

Sample ID	Δ_{47-ARF} (‰)	2σ	T (°C)	2σ	$\delta^{18}O_{gas}$(‰)	$\delta^{18}O_{carbonate}$(‰)	$\delta^{18}O_w$(‰)	2σ
LK-LK-5-0	0.723	0.009	16.7	2.83	35.93	27.34	-3.59	0.60
MK-SR-1-15	0.717	0.001	18.6	0.30	36.44	27.85	-2.68	0.10
DT-LB-1-16.5	0.717	0.003	18.6	1.04	35.79	27.20	-3.31	0.14
UK-GR-3-20	0.713	0.017	20.1	2.29	36.09	27.50	-2.71	0.64
LK-5K-N5-0	0.728	0.005	14.9	1.64	35.77	27.18	-4.12	0.60
UK-GR-4-10	0.713	0.016	20.5	5.61	35.56	26.97	-3.17	1.22
DT-GB-6-27	0.717	0.017	19.0	6.01	36.21	27.62	-2.86	1.25
UK-CF-7-25	0.708	0.015	22.0	5.49	35.79	27.20	-2.63	1.12
LK-WS-3-21	0.721	0.017	17.9	5.92	35.13	26.55	-4.14	1.25
LK-LK-18-2	0.716	0.012	19.2	3.99	35.96	27.37	-3.02	0.83
MK-SR-3-3	0.700	0.010	24.9	3.53	36.28	27.65	-1.55	0.68
UK-CF-4-5	0.699	0.015	25.2	3.10	35.73	27.14	-2.03	0.64
MK-TN-1-6	0.708	0.003	19.7	0.92	36.32	28.27	-2.57	0.22
MK-TN-2-1	0.708	0.007	21.7	2.31	36.63	28.03	-1.85	0.45
LK-WS-3-5	0.715	0.137	19.4	0.97	35.70	27.11	-3.22	0.22